INTERACTIONS BETWEEN TROPICAL CYCLONES AND THE MIDLATITUDE WAVEGUIDE: DOWNSTREAM IMPACTS AND THE ROLE OF CONVECTIVE PROCESSES

by

Kevin C. Prince

A Dissertation Submitted in

Partial Fulfillment of the

Requirements for the Degree of

Doctor of Philosophy

in Atmospheric Sciences

at

The University of Wisconsin-Milwaukee

August 2022

ABSTRACT

INTERACTIONS BETWEEN TROPICAL CYCLONES AND THE MIDLATITUDE WAVEGUIDE: DOWNSTREAM IMPACTS AND THE ROLE OF CONVECTIVE PROCESSES

by

Kevin C. Prince

The University of Wisconsin-Milwaukee, 2022
Under the Supervision of Professor Clark Evans

Significant amplification to the waveguide can occur when a recurving tropical cyclone (TC) interacts with the midlatitude flow, leading to significant downstream impacts. To this point in time, TC-midlatitude waveguide interactions have been conceptualized as primarily being driven by large-scale processes, with convective-scale contributions having been parameterized or neglected. This three-part study diagnoses the impact TC-midlatitude waveguide interactions have on the intensity evolution of downstream TCs and the role convective-scale processes play in TC-midlatitude waveguide interactions.

Recurving TCs in both the North Atlantic and western North Pacific basins frequently interact favorably with upstream troughs, where a favorable interaction entails the tightening of a pre-existing potential vorticity (PV) gradient on the eastern flank of the trough, leading to subsequent downstream flow amplification in the vicinity of a downstream TC. In the Atlantic, weakening downstream TCs are closer to the midlatitude waveguide on the southeastern edge of the amplified midlatitude ridge, whereas strengthening downstream TCs are further from the waveguide and equatorward of the amplified midlatitude ridge. Conversely, western North Pacific strengthening and weakening secondary TCs are primarily stratified by latitude, with weakening secondary TCs located poleward of their strengthening secondary TC counterparts.

Convective-scale processes are shown to potentially play a role in determining the strength and downstream evolution of TC-midlatitude waveguide interactions. This importance of convective-scale processes on the large-scales is accomplished by way of an inverse energy cascade supported by the filamentation of intensely negative PV generated by deep, moist convection. These negative PV anomalies are generated by intense horizonal gradients of diabatic warming and exist primarily in the middle- to upper-troposphere. While preliminary sensitivity simulations suggest that convective-scale processes in particular regions of a TC-midlatitude waveguide interaction may not play a key role in determining the strength, and subsequent evolution of the interaction, that is not to say that convective-scale processes do not play a role at all. Additionally, the relative importance of convective-scale processes may depend on the particular TC-midlatitude waveguide interaction being studied.

For Anna and my family.

TABLE OF CONTENTS

LIST OF FIGURES

LIST OF TABLES

ACKNOWLEDGEMENTS

I would first like to acknowledge my parents for being extremely supportive of my passions from a young age all the way through my schooling. Without the support of them, I would not be where I am today. I would also like to thank Anna for the years of support while completing my PhD, I am a better person for having met you. Next, I would like to thank my sisters, Heather and Kristin, their husbands, Shane, and Travis, respectively, my three nieces, Kaiya, Vivian, and Charlotte, and finally my four grandparents, for being an extremely supporting family. I would also like to thank the friends I have had since grade school and the friends I made during my time at CMU and UWM.

Finally, I would like to thank my adviser Professor Clark Evans for providing a tremendous amount of support, advice, and opportunities, over the six years we have worked together. I will look back on my time at UWM very fondly, and this is in large part due to the advising Clark provided.

Chapter 1

A CLIMATOLOGY OF INDIRECT TROPICAL CYCLONE INTERACTIONS IN THE NORTH ATLANTIC AND WESTERN NORTH PACIFIC BASINS

The close proximity of TCs Irma and Jose in September of 2017 inspired the first part of this study which builds a larger dataset of cases in which TCs are not only in close proximity to one another, but where one of the TCs is concurrently interacting favorably with the midaltitude waveguide. The material in part 1 is drawn from Prince and Evans (2020, *Mon. Wea. Rev.*) for which the American Meteorological Society currently holds the copyright.

1.1 Introduction

A significant fraction of tropical cyclones (TCs) recurve into the midlatitude flow in many tropical basins around the world, with approximately 37% of all western North Pacific TCs from 1979-2009 recurving (Archambault et al. 2013) and approximately 68% of North Atlantic TCs from 1950-2010 recurving (Colbert and Soden 2012). As these TCs recurve, their interaction with the midlatitude flow may cause increases in flow "waviness" (Archambault et al. 2013, 2015) and increased forecast errors downstream (Agustí-Panareda et al. 2004, 2005; McTaggart-Cowan et al. 2007; Harr and Dea 2009; Anwender et al. 2010; Grams et al. 2011, 2015; Pantillon et al. 2013; Riemer and Jones 2014; Keller et al. 2011, 2019). Extensive research has been published on the recurvature and extratropical transition (ET) of TCs (Jones et al. 2003; Evans et al. 2017; Keller et al. 2019) and the impact these recurving TCs have on the

midlatitude waveguide (Anwender et al. 2008; Hodges et al. 2008; Aiyyer 2015; Grams and Archambault 2016; Keller et al. 2019; Pohorsky et al. 2019).

As a TC enters the midlatitudes, it may perturb the waveguide many thousands of kilometers downstream (Riemer and Jones 2010, 2014; Grams et al. 2013b; Keller 2017; Keller et al. 2019). This is accomplished primarily through the diabatically driven vertical redistribution of isentropic PV aloft, wherein PV is reduced (in the Northern Hemisphere) above the level of maximum diabatic warming near the TCs center (Hoskins et al. 1985; Grams et al. 2011). This very-low PV air aloft is then advected radially outward, away from the TCs center, by the TCs divergent secondary circulation, tightening the local PV gradient and facilitating the creation of a jet or amplification of a pre-existing jet (Riemer and Jones 2010; Grams et al. 2011, 2013a; Archambault et al. 2013, 2015; Grams and Archambault 2016). This jet strengthening, along with the poleward transport of warm, moist air, facilitates rapid ridge-building immediately downstream of the TC (Cunningham and Keyser 2000; Bosart 2003; Riemer and Jones 2010). The pattern reconfiguration associated with the interaction between the midlatitude waveguide and primary TC may in some cases result in downstream anticyclonic wave breaking (Thorncroft et al. 1993; Zhang et al. 2017; Zhang and Wang 2018). Other factors that govern the extent to which a TC perturbs the midlatitude waveguide include characteristics of the midlatitude pattern itself, including but not limited to its antecedent wavelength and amplitude (Torn and Hakim 2015; Quinting and Jones 2016; Wirth et al. 2017; Finocchio and Doyle 2019), and the phasing of the TC with the upstream trough (e.g., Ritchie and Elsberry 2003, 2007; Scheck et al. 2011; Grams et al. 2013a; Archambault et al. 2013, 2015; Riemer and Jones 2014; Wirth et al. 2018; Komaromi and Doyle 2018; Keller et al. 2019; Riboldi et al. 2019).

A substantial portion of TCs form when one or more existing TCs are already present, with approximately one-third in the North Atlantic and nearly one-half in the western North Pacific forming with another TC already existing in its respective basin (Schenkel 2016, 2017). Furthermore, when two or more TCs are present within a given basin, the average distance between the TCs is approximately 1500 km in the North Atlantic and approximately 2000 km (approximately one synoptic-scale Rossby wavelength in each respective basin) in the western North Pacific (Schenkel 2017). While many studies have shown how midlatitude features can influence TC activity across a wide range of spatial and temporal scales (McTaggart-Cowan et al. 2007; Galarneau et al. 2015; Fowler and Galarneau 2017; Zhang et al. 2016; 2017), there has yet to be a *comprehensive* evaluation of TCs which perturb the midlatitude waveguide in the presence of a secondary TC and the impact this interaction can have on the secondary TCs track and intensity. Consequently, this study focuses on what is termed an *indirect* interaction (in contrast with the *direct* interaction first conceptualized by Fujiwhara 1921). Herein, an indirect interaction is conceptualized as the process of a primary TC influencing a secondary TC by influencing the synoptic-scale pattern in which the secondary TC is embedded.

A recent example of an indirect interaction is given by North Atlantic TCs Irma and Jose in 2017 (Fig. 1.1). As Irma recurves northward across the Florida peninsula, the TC interacts with an upstream shortwave trough over the southeastern United States. Negative PV advection by the primary TCs upper-tropospheric divergent outflow (as conceptualized by Archambault et al. 2013) tightens the local PV gradient between the TC and upstream trough, leading to local jet-streak enhancement and subsequent downstream ridge amplification (Fig. 1.1). Intensified upper-tropospheric northerly flow on the eastern periphery of the Irma-amplified downstream ridge blocks Jose from propagating poleward and increases the vertical wind shear incident upon the

TC. The increased vertical wind shear causes a rapid decrease in Jose's intensity from 115 kt/948 hPa at 1200 UTC on 10 September 2017 to 70 kt/979 hPa at 1200 UTC on 12 September 2017 (Berg 2018).

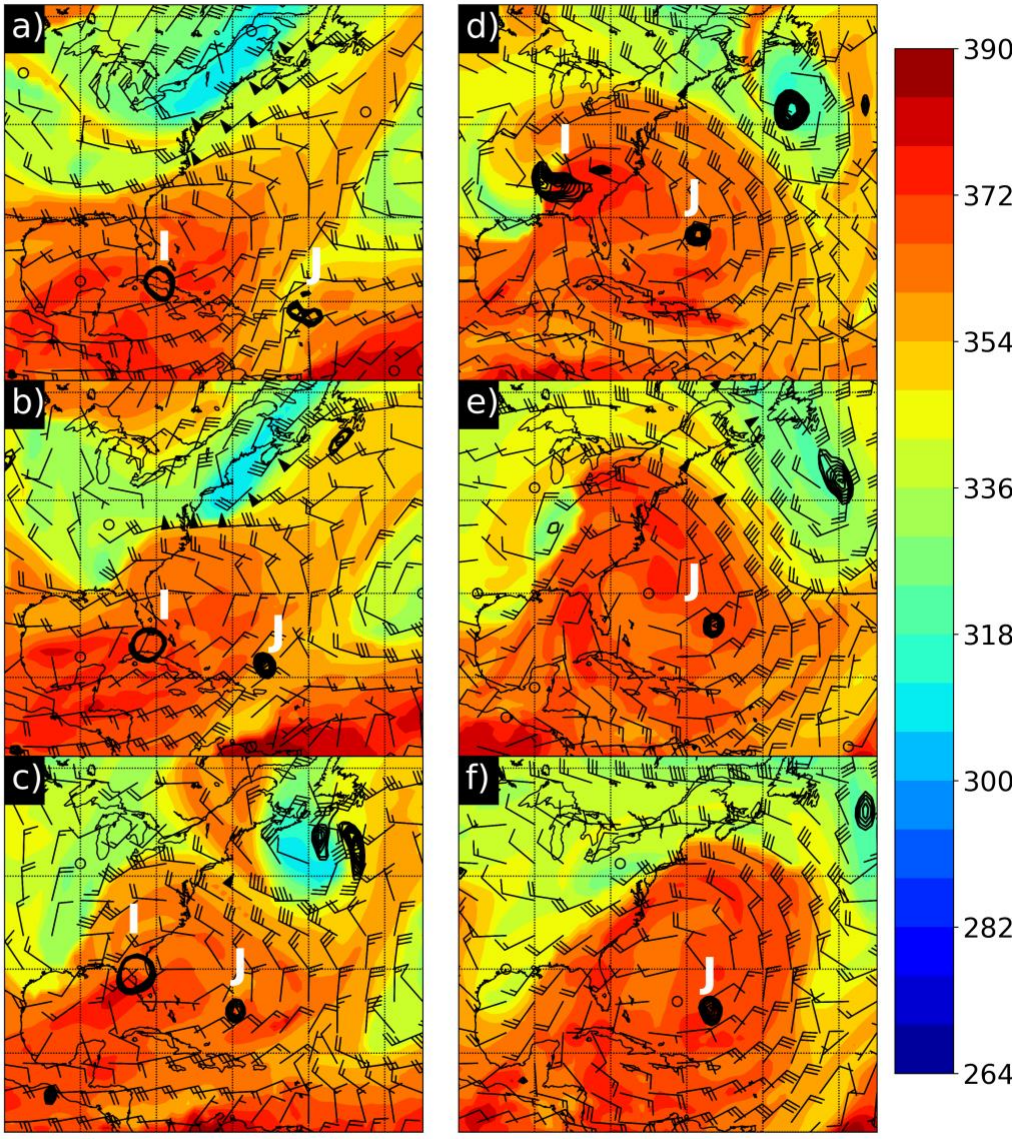

Figure 1.1. Potential temperature (shaded in K per the color bar at right) on the 2 PVU (Potential Vorticity Unit; 10^{-6} m^2 s^{-1} K kg^{-1}) surface, horizontal wind on the 2 PVU surface (barbs; half-flag: 5 kt, flag: 10 kt, pennant: 50 kt), and 850 hPa relative vorticity (black contours; from 10 to 20*10^{-5} s^{-1} every 2 s^{-1}) at 1200 UTC (a) 9, (b) 10, (c) 11, (d) 12, (e) 13, and (f) 14 September 2017 for North Atlantic TCs Irma (primary; I) and Jose (downstream; J). Latitude and longitude lines are drawn every 10˚.

An example of multiple indirect interaction events in close temporal proximity occurred in 2010 between North Atlantic TCs Danielle, Earl, Fiona, and Gaston in 2010 (Fowler and Galarneau 2017). The recurvature of TC Danielle into a preexisting Rossby-wave train over North America results in ridge amplification immediately downstream, which increases the meridional flow on its eastern and western flanks and, in turn, increases the vertical wind shear in proximity to three secondary TCs (Earl, Fiona, and Gaston). Forecast uncertainties associated with the initial interaction of TC Danielle with the midlatitude waveguide amplify downstream at medium-range lead times, reducing the midlatitude predictability across the North Atlantic and increasing forecast track errors for TCs Fiona and Gaston (Fowler and Galarneau 2017).

The purpose of this study is to produce a climatology of indirect TC interactions in the North Atlantic and western North Pacific basins from 1989-2018. This climatology provides a robust dataset for future studies to quantify the extent to which a primary TC can influence a secondary TCs track and intensity and more generally to document the influences of recurving TCs on the downstream tropical-to-subtropical environment across multiple basins. The improved understanding of these interactions is hoped to improve the understanding and predictability of the potential interaction outcomes, which may in turn lead to improved TC track and intensity forecasts.

1.2 Methods

1.2.1 Data

Six-hourly data from the European Center for Medium-Range Weather Forecasts interim reanalysis dataset (ERA-Interim; Dee et al. 2011) are used to identify all indirect interactions. The dataset has roughly 80-km resolution on a reduced Gaussian grid with 60 isobaric levels up to 0.1 hPa. Best-track and forecast track and intensity data for all TCs in the North Atlantic are

collected from the NHC best-track database (Landsea and Franklin 2013) and public archive (ftp://ftp.nhc.noaa.gov/atcf/archive/), respectively, while best-track and forecast track and intensity data for the western North Pacific are collected from the Joint Typhoon Warning Center's collaboration site (JTWC 2019). Due to data availability limitations, note that the forecast tracks in the western North Pacific are based only on TCs between 2002-2018.

1.2.2 Case Selection

All classified tropical and subtropical cyclones, no matter their intensity, occurring in the North Atlantic and western North Pacific basins from 1989-2018 are considered as potential cases. While classification practices for the North Atlantic do change somewhat during this time frame, these have been shown to have a minimal impact on total TC counts per year, resulting in minimal impacts to the number of indirect interactions (Landsea 2007). The same period was selected for the western North Pacific for consistency.

Two screening steps are followed to identify indirect-interaction events. The first filtering step requires that two or more TCs concurrently exist for all candidate events. As a TC interacts with an upstream trough, the resulting perturbation is most pronounced within one wavelength downstream (Riemer and Jones 2010, 2014; Grams et al. 2013b; Keller 2017; Keller et al. 2019; Pohorsky et al. 2019). Therefore, the second screening step requires that the two TCs be within this distance, as determined by the geometry of the midlatitude flow at the time of interaction. Note that a TC may both be influenced by and subsequently influence an additional secondary TC, which is counted as two interaction events. However, a TC that influences more than one secondary TC (although there are no such cases within the dataset considered due to the one-wavelength restriction) is a single interaction event.

The Archambault et al. (2013) interaction metric is used to ensure that the midlatitude-flow reconfiguration downstream of a candidate primary TC is at least partially the result of the primary TCs diabatically driven upper-tropospheric divergent outflow impinging upon the midlatitude waveguide. The interaction metric is defined as the negative PV advection by the divergent (or irrotational) component of the wind, i.e.,

$$-\overrightarrow{V_\chi} * \nabla_p PV < 0 \tag{1.1}$$

where $\overrightarrow{V_\chi}$ is the 250-150 hPa–averaged irrotational component of the horizontal wind and $\nabla_p PV$ is the 250-150 hPa–averaged PV gradient. Candidate events must be associated with an instantaneous metric value of -1 PVU day^{-1} or lower at one or more locations within 500 km of the primary TCs center, consistent with Archambault et al. (2013, 2015; albeit with a coarser dataset in their study), to be included. Compositing (section 1.2.3) is temporally centered on the *time of maximum interaction*, defined as the time at which the interaction metric achieves its maximum magnitude.

In contrast to the indirect interaction between TCs Irma and Jose depicted in Fig. 1, not all TC pairs for which a primary TC recurves into the midlatitudes and undergoes ET qualify as indirect-interaction events. A representative example is given by North Atlantic TC Ophelia in 2011, which recurved into the midlatitude flow while TC Philippe began to develop to its southeast (Fig. 1.2). As Ophelia recurves into the midlatitude flow, an area of negative PV advection more negative than the -1 PVU day^{-1} threshold is present but is located 1500-2000 km west of TC Ophelia (Fig. 1.2f). A closer inspection reveals that a majority of Ophelia's upper-tropospheric outflow is directed eastward into the midlatitude ridge rather than westward against the trough (Fig. 1.2f,g), such that the negative PV advection to Ophelia's west results from other forcings (e.g., deep, moist convection along the United States east coast) rather than from

Ophelia. Further, the direction of TC Ophelia's outflow primarily into the midlatitude ridge to its east cannot result in significant midlatitude amplification, and thus no indirect interaction with TC Philippe, as the Petterssen development parameters (upper-tropospheric divergence, lower-tropospheric warm-air advection, and mid-tropospheric cyclonic vorticity advection) indicate that only immediately ahead of a trough is significant amplification to the midlatitude waveguide by a TC possible (Petterssen and Smeybe 1971; Keller et al. 2019).

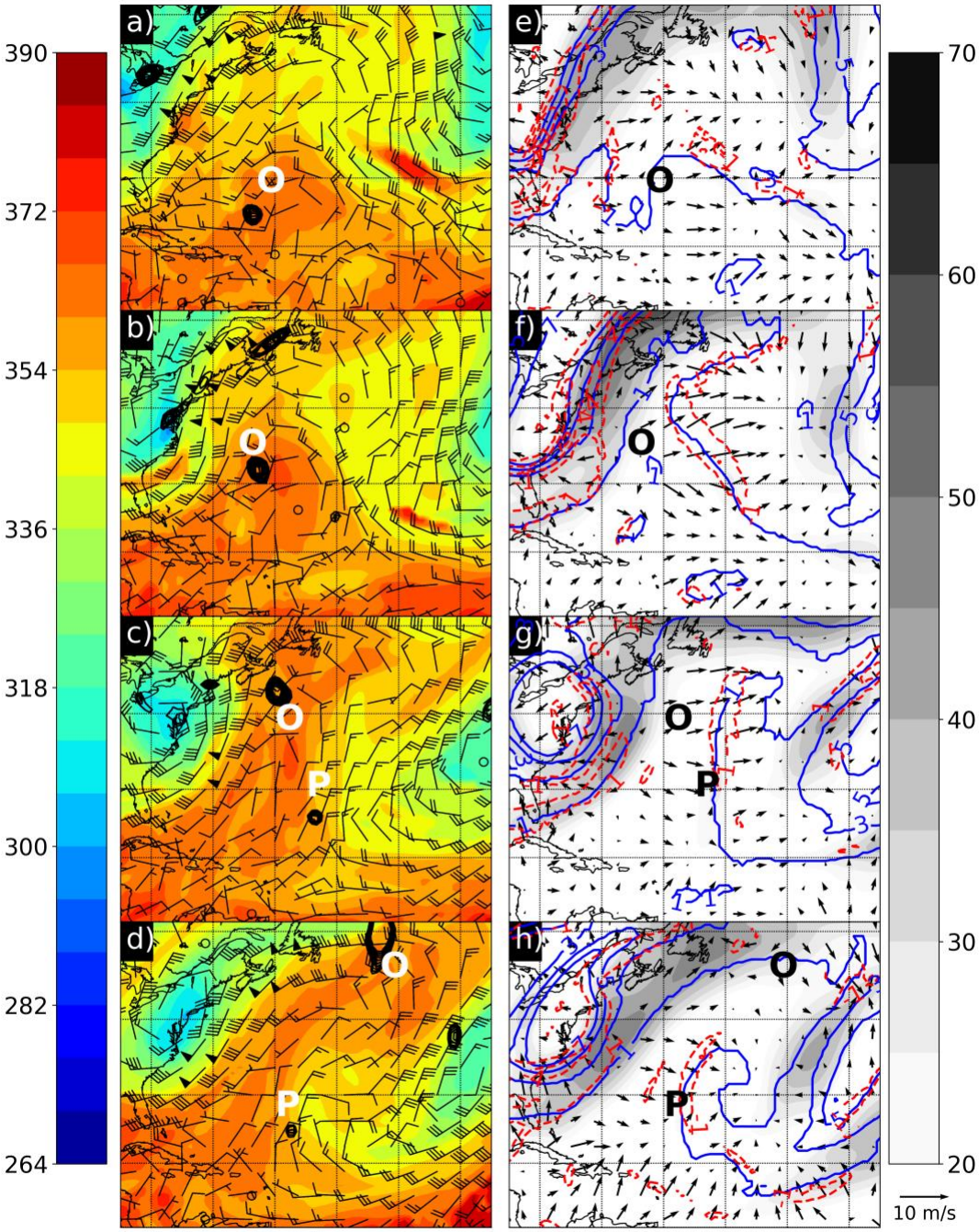
a)
b)
c)
d)
e)
f)
g)
h)
390
372
354
336
318
300
282
264
70
60
50
40
30
20
10 m/s

Figure 1.2. In panels (a-d), potential temperature (shaded in K per the color bar at left) on the 2 PVU (Potential Vorticity Unit; 10^{-6} m^2 s^{-1} K kg^{-1}) surface, horizontal wind on the 2 PVU surface (barbs; half-flag: 5 kt, flag: 10 kt, pennant: 50 kt), and 850 hPa relative vorticity (black contours; from 10 to 20*10^{-5} s^{-1} every 2 s^{-1}) at 0000 UTC (a) 1, (b) 2, (c) 3, and (d) 4 October 2011 for North Atlantic TCs Ophelia (primary; O) and Philippe (downstream; P). In panels (e-h), 250-150 hPa layer-mean PV (blue contours every 2 PVU starting at 1 PVU), 250-150 hPa layer-mean horizontal wind speed (shaded in m s^{-1} per the color bar at right), 250-150 hPa layer-mean irrotational wind (vectors; m s^{-1}; reference vector at lower right), 250-150 hPa advection of the layer-mean potential vorticity by the layer-mean irrotational wind (red-dashed contours every -3 PVU day^{-1} starting at -1 PVU day^{-1}) at the same times as in panels (a-d). Latitude and longitude grid lines are drawn every 10˚.

1.2.3 Compositing

Two compositing approaches are used in this study, one to document the impact the primary TCs have on the midlatitude waveguide downstream of their maximum interaction location and one to document differences in the large-scale environments between secondary TCs that weaken or intensify in the 48-h following the time of maximum interaction. The first approach composites around the fixed spatial location of the maximum absolute value of negative PV advection by the irrotational wind at the time of maximum interaction between the primary TC and the midlatitude waveguide (as in Archambault et al. 2015). The second approach is spatially centered on the (temporally variable) secondary TCs' locations. Both approaches use a domain encompassing +/- 37.5° latitude and 45° longitude west to 90° longitude east of their respective centering points and are generated for a 96-h period between 48-h prior to and 48-h after the time of maximum interaction of the primary TC with the midlatitude waveguide.

1.2.4 Ventilation Index Calculation

The ventilation index of Tang and Emanuel (2012) is used to better understand the tropospheric-deep impacts of indirect-interaction events to the environments within which the secondary TCs are embedded. This index is defined as:

$$\Lambda = \frac{u_{shear}\chi_m}{u_{PI}} \tag{1.2}$$

where $u_{shear} = |\boldsymbol{v_{850}} - \boldsymbol{v_{200}}|$ is the bulk environmental vertical wind shear magnitude between 850 and 200 hPa, u_{PI} is the maximum potential intensity (MPI), and χ_m is the nondimensional entropy deficit. The entropy deficit χ_m is defined as:

$$\chi_m = \frac{s_m^* - s_m}{s_{SST}^* - s_b} \tag{1.3}$$

where s_m^* is the saturation entropy at 600 hPa in the TCs inner core, s_m is the environmental entropy at 600 hPa, s_{SST}^* is the saturation entropy at the sea-surface temperature (SST), and s_b is the entropy of the boundary layer. The derivation of the ventilation index and details of calculating the ventilation index from gridded data can be found in Tang and Emanuel (2012). Due to the coarseness of the ERA-Interim SST data, the SST data is substituted with daily optimum-interpolation 0.25˚ SST data (Reynolds et al. 2007; Banzon et al. 2016) for the calculations of the entropy deficit and MPI to better represent spatiotemporal SST variability; however, qualitatively identical results are obtained when instead using the ERA-Interim SSTs (not shown). Additional information on the calculation of the ventilation index on the gridded ERA-Interim domain can be found in Appendix A.

1.2.5 Forecast Error Calculation

To quantify the track/intensity predictability for the primary and secondary TCs, official warning-center (NHC for the North Atlantic, Joint Typhoon Warning Center for the western North Pacific) track and intensity forecasts are verified. Errors are calculated following NHC operational practice, such that only TCs which attain tropical-storm or hurricane/typhoon status are included in the evaluation. Additionally, forecasts which verify over land are included, but forecasts verifying after the TC is no longer classified as tropical are excluded. Forecast errors for both primary and secondary TCs are computed at multiple forecast lead times surrounding the time of maximum interaction; however, the analysis presented herein focuses only on forecasts issued between 24-48 h before the time of maximum interaction. This time corresponds with the times at which the basin-wide predictability at medium-ranges (e.g., 2-5+ days) is typically degraded due to the uncertainty in predicting the interaction of the primary TC with the upstream trough (Aiyyer 2015; Harr and Archambault 2016).

1.2.6 Statistical-Significance Testing

The extent to which composite-mean atmospheric fields (sections 1.2.3-1.2.4) and official-forecast track and intensity errors (section 1.2.5) are significantly different from climatology is assessed using Monte Carlo bootstrapping (Efron and Tibshirani 1994).

For composite-mean atmospheric fields, the climatology is defined using a fifteen-day average centered on the date of each indirect-interaction event (the time of maximum interaction) over the period 1980-2010, with this 30-year duration selected following current operational practices for defining climate normals. Next, 1,000 samples of anomalies (each with a sample size equal to the number of indirect-interaction events in each basin) are randomly drawn from dates in 1980-2010 between one week prior to one week after the date of each indirect-interaction event, with each event contributing one member per sample. Composite-mean atmospheric fields are said to be significantly different from climatology to 95% confidence when they are smaller than the 25th-ranked or larger than the 975th-ranked samples of climatological anomalies.

For official forecasts, the climatology is defined from the set of all TCs (separately for the North Atlantic and western North Pacific basins) between 1989-2018 excluding the primary and secondary TCs. Next, 10,000 samples of forecast errors (each with a sample size equal to the number of indirect-interaction events in each basin) are randomly drawn from climatology, with separate samples drawn at each forecast lead time considered (0, 12, 24, 36, 48, 72, 96, and 120 h). Composite-mean forecast errors are said to be significantly different from climatology to 95% confidence when they are smaller than the 250th-ranked or larger than the 9750th-ranked samples of climatological mean forecast errors.

1.3 Event Climatology

Twenty-six indirect interactions are identified for the North Atlantic basin (Table 1.1), whereas 56 are identified for the western North Pacific basin (Table 1.2). It is speculated that the greater number of events for the western North Pacific largely results from the larger number of TCs in this basin (approximately 24 TCs per year over the 30-year climatology; JTWC 2018) as compared to the North Atlantic basin (approximately 15 TCs per year over the 30-year climatology; Landsea and Franklin 2013). Unsurprisingly, the months in which TCs typically form are also the months with the highest numbers of indirect interaction events, with an extremely high linear-correlation coefficient (0.79 with a *p*-value of 0.11 for the North Atlantic; 0.95 with a *p*-value of 10^{-4} for the Western North Pacific; note that this and subsequent *p*-values in this subsection are assessed using a Student's *t*-test excluding all occurrences of zero for both values) between the monthly climatologies for both basins (Fig. 1.3). Further, the *annual* counts of TCs and indirect interaction events in a given basin are moderately linearly correlated (0.35 with a *p*-value of 0.18 for the North Atlantic; 0.21 with a *p*-value of 0.28 for the Western North Pacific; see also Fig. 3b,d).

Primary TC Storm Name	Secondary TC Storm Name	Date of Maximum Interaction	Interaction Metric (PVU day^{-1})
Florence (2006)	Gordon (2006)	Sep 11 0600 UTC	-2.87
Floyd (1999)	Gert (1999)	Sep 16 0000 UTC	-2.20
Ivan (2004)	Jeanne (2004)	Sep 8 1800 UTC	-1.88
Matthew (2016)	Nicole (2016)	Oct 8 1800 UTC	-1.72
Irene (2011)	Jose (2011)	Aug 28 0600 UTC	-1.60
Jeanne (2004)	Karl (2004)	Sep 17 1200 UTC	-1.58
Odette (2003)	Peter (2003)	Dec 8 0000 UTC	-1.42
Igor (2010)	Julia (2010)	Sep 19 0600 UTC	-1.41
Irma (2017)	Jose (2017)	Sep 10 1800 UTC	-1.29
Gabrielle (2001)	Felix (2001)	Sep 14 1800 UTC	-1.27
Karl (2016)	Lisa (2016)	Sep 25 0000 UTC	-1.24
Fabian (2003)	Isabel (2003)	Sep 7 1200 UTC	-1.22
Karl (2004)	Lisa (2004)	Sep 21 0000 UTC	-0.92
Gordon (2000)	Helene (2000)	Sep 16 1800 UTC	-0.79
Isidore (2002)	Kyle (2002)	Sep 25 0600 UTC	-0.79
Michael (2000)	Nadine (2000)	Oct 19 1200 UTC	-0.76
Maria (2005)	Nate (2005)	Sep 24 0000 UTC	-0.73
Fran (1996)	Hortense (1996)	Aug 30 1800 UTC	-0.60
Hanna (2008)	Ike (2008)	Sep 3 1800 UTC	-0.56
Karl (1998)	Jeanne (1998)	Sep 26 1800 UTC	-0.55
Katrina (2005)	Lee (2005)	Aug 30 1800 UTC	-0.52
Earl (2010)	Fiona (2010)	Aug 31 1800 UTC	-0.52
Danielle (2010)	Earl (2010)	Aug 29 1200 UTC	-0.49
Isabel (2003)	Juan (2003)	Sep 17 1800 UTC	-0.34
Gustav (2008)	Hanna (2008)	Aug 31 1200 UTC	-0.30
Gustav (1990)	Hortense (1990)	Sep 1 1800 UTC	-0.10

Table 1.1. Climatological information on all twenty-six primary and secondary TCs in the North Atlantic basin, as sorted in decreasing order based on the magnitude of the temporally (from 48 hours before the time of maximum interaction to 48 hours after) and spatially (over a box extending 7.5˚ in all directions from the location of maximum interaction) averaged value of the interaction metric, as defined by Archambault et al. (2013).

Primary TC Storm Name	Secondary TC Storm Name	Date of Maximum Interaction	Interaction Metric (PVU day^{-1})
Lan (2017)	Saola (2017)	Oct 21 1200 UTC	-3.69
Soulik (2006)	Rumbia (2006)	Oct 6 0000 UTC	-3.56
Songda (2004)	Sarika (2004)	Sep 7 0600 UTC	-3.54
Wipha (2013)	Francisco (2013)	Oct 15 1200 UTC	-3.47
Talas (2011)	Noru (2011)	Sep 2 1200 UTC	-3.20
Megi (2004)	Aere (2004)	Aug 18 0600 UTC	-3.16
Podul (2001)	Ling-Ling (2001)	Oct 26 1200 UTC	-3.12
Fitow (2013)	Danas (2013)	Oct 4 0600 UTC	-3.07
Melor (2009)	Nepartak (2009)	Oct 7 0000 UTC	-2.90
Zeb (1998)	Babs (1998)	Oct 17 0000 UTC	-2.70
Tokage (2004)	Nock-Ten (2004)	Oct 20 1200 UTC	-2.58
Francisco (2013)	Lekima (2013)	Oct 24 1800 UTC	-2.46
Saomai (2000)	Sonamu (2000)	Sep 15 0000 UTC	-2.46
Jelawat (2012)	Ewiniar (2012)	Sep 29 0600 UTC	-2.44
Bolaven (2012)	Tembin (2012)	Aug 28 0600 UTC	-2.38
Lupit (2009)	Mirinae (2009)	Oct 26 1800 UTC	-2.26
Kompasu (2010)	Malou (2010)	Sep 1 1800 UTC	-2.26
Chaba (2010)	Seventeen (2010)	Oct 30 0600 UTC	-2.23
Rusa (2002)	Sinlaku (2002)	Aug 31 1800 UTC	-2.21
Ketsana (2003)	Parma (2003)	Oct 25 0600 UTC	-2.19
Ryan (1992)	Sibyl (1992)	Sep 10 1800 UTC	-2.18
Dianmu (2004)	Mindulle (2004)	Jun 21 0600 UTC	-2.13
Fitow (2007)	Danas (2007)	Sep 7 1800 UTC	-2.06
Haiyan (2001)	Podul (2001)	Oct 17 1800 UTC	-2.06
Chan-Hom (2015)	Nangka (2015)	Jul 12 0000 UTC	-2.02
David (1997)	Ella (1997)	Sep 16 1200 UTC	-2.01
Goni (2015)	Atsani (2015)	Aug 25 0600 UTC	-1.92
Aere (2004)	Chaba (2004)	Aug 30 1800 UTC	-1.91
Nida (2004)	Omais (2004)	May 20 0600 UTC	-1.91
Zane (1996)	Yates (1996)	Sep 29 0600 UTC	-1.87
Chanthu (2016)	Mindulle (2016)	Aug 17 0000 UTC	-1.87
Rammasun (2002)	Chataan (2002)	Jul 5 0600 UTC	-1.85
Robyn (1993)	Steve (1993)	Aug 10 0000 UTC	-1.78
Mawar (2005)	Guchol (2005)	Aug 25 0000 UTC	-1.63
Prapiroon (2012)	Maria (2012)	Oct 18 0600 UTC	-1.57
Chataan (2002)	Halong (2002)	Jul 10 1800 UTC	-1.57
Shanshan (2006)	Yagi (2006)	Sep 17 1800 UTC	-1.56

Kong-Rey (2013)	Toraji (2013)	Aug 31 0000 UTC	-1.45
Fung-Wong (2014)	Kalmaegi (2014)	Sep 23 1800 UTC	-1.34
Prapiroon (2000)	Saomai (2000)	Aug 31 0600 UTC	-1.31
Mindulle (2004)	Ting-Ting (2004)	Jul 4 0600 UTC	-1.10
Page (1990)	Owen (1990)	Nov 29 0000 UTC	-1.09
Roger (1989)	Sarah (1989)	Aug 26 0600 UTC	-1.07
Omar (1992)	Polly (1992)	Aug 31 1200 UTC	-1.04
Sinlaku (2008)	Sixteen (2008)	Sep 10 0600 UTC	-0.96
Pabuk (2001)	Wutip (2001)	Aug 21 0000 UTC	-0.92
Kong-Rey (2018)	Trami (2018)	Sep 30 0600 UTC	-0.91
Orchid (1994)	Ruth (1994)	Sep 26 1200 UTC	-0.82
Olga (1999)	Paul (1999)	Aug 3 0000 UTC	-0.82
Muifa (2011)	Merbok (2011)	Aug 7 1200 UTC	-0.74
Violet (1996)	Tom (1996)	Sep 17 0000 UTC	-0.53
Walt (1994)	Zeke (1994)	Jul 20 0600 UTC	-0.49
Rosie (1997)	Scott (1997)	Jul 25 0600 UTC	-0.47
Damrey (2012)	Haikui (2012)	Jul 30 0600 UTC	-0.42
Rumbia (2018)	Soulik (2018)	Aug 16 0600 UTC	-0.41
Morakot (2009)	Etau (2009)	Aug 9 0600 UTC	-0.34

Table 1.2. As in Table 1.1, except for the 56 cases in the western North Pacific basin.

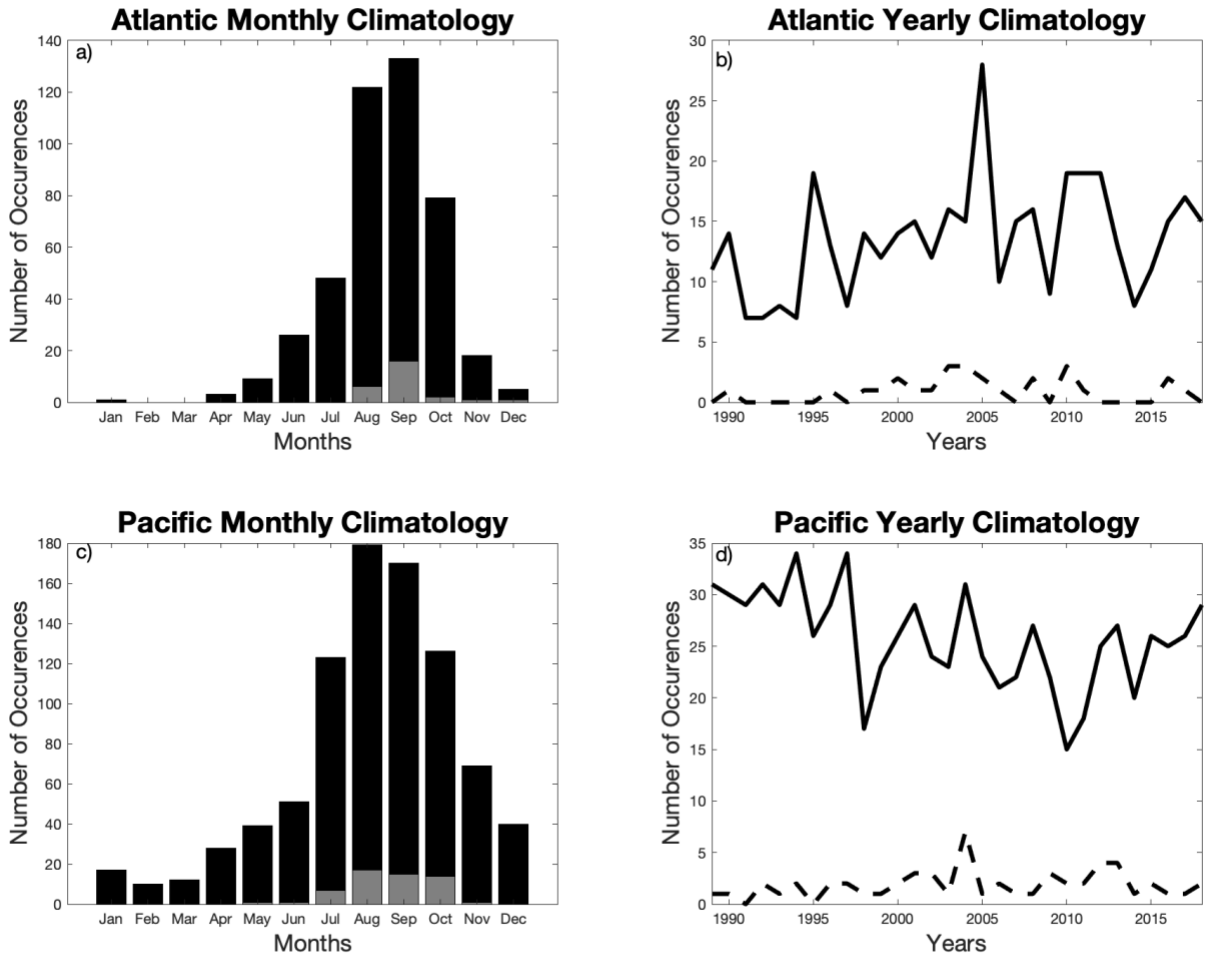

Figure 1.3. Indirect-interaction occurrence (light grey bar; dashed line) compared to the total number of TCs (black bar; solid line) as a function of month aggregated (a) over all years, and (b) yearly for the North Atlantic. The bottom two plots (c,d) are the same as in (a,b) except for the western North Pacific.

The indirect interactions identified herein are associated with highly variable tracks for both the primary and secondary TCs (Fig. 1.4) and correspondingly variable midlatitude flow configurations (Fig. 1.5). Even when centered around a common location, here given by the average location of the primary TCs at the time of maximum interaction, there is still significant track variability away from the time of maximum interaction (Fig. 1.4a,c) that is most pronounced in the North Atlantic (Fig. 1.4a). A shorter composite track for secondary TCs in both basins is representative of a slower translation speed for these TCs than their primary counterparts because the primary TCs are at higher latitudes where large-scale tropospheric-deep flow is typically stronger (Fig. 1.4). In the North Atlantic weakening secondary TCs are slightly further north and east than their strengthening or no-change counterparts (Fig. 1.4a,b and Table 1.3), whereas weakening secondary TCs in the western North Pacific are further north and slightly east of non-weakening secondary TCs (Fig. 1.4c,d and Table 1.4).

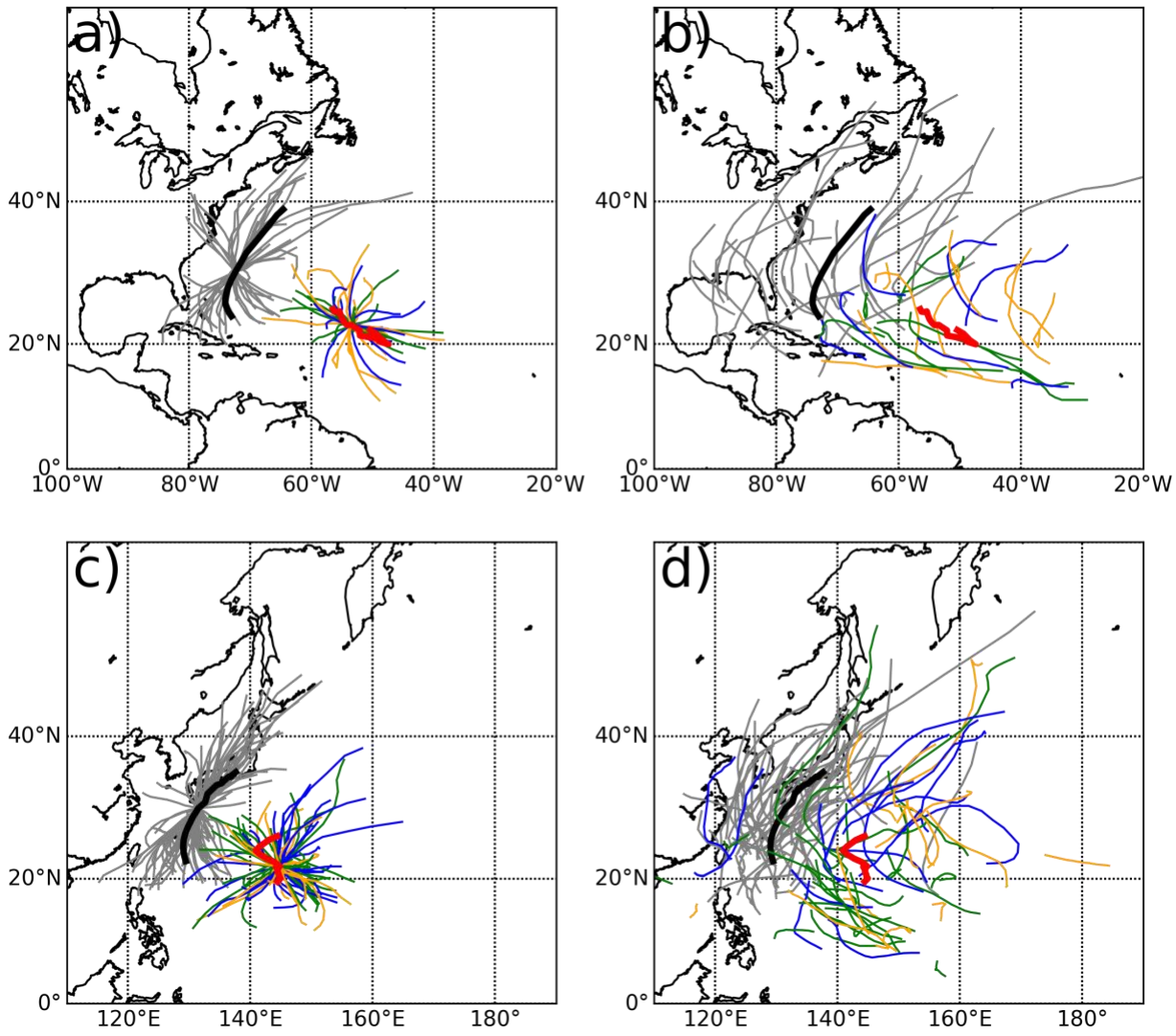

Figure 1.4. Best-track TC tracks for all indirect-interaction primary TCs (as given by the thin grey lines) in the (a, b) North Atlantic and (c, d) western North Pacific basins from 48-h before the time of maximum interaction to 48-h after at six-hour increments. Panels (a) and (c) depict tracks shifted to the average primary-TC location at the time of maximum interaction, whereas panels (b) and (d) show the unshifted TC tracks. The thick black lines depict the average primary-TC tracks over the 96-h period considered, whereas the thick red lines depict the average secondary-TC tracks over the 96-h period considered. Orange lines represent the tracks of secondary TCs which did not change intensity (again utilizing minimum central pressure to define these criteria as in Tables 3 and 4), blue lines represent the tracks of secondary TCs that weakened over the 48-h after the time of maximum interaction, and green lines represent the tracks of secondary TCs that strengthened over the 48-h after the time of maximum interaction.

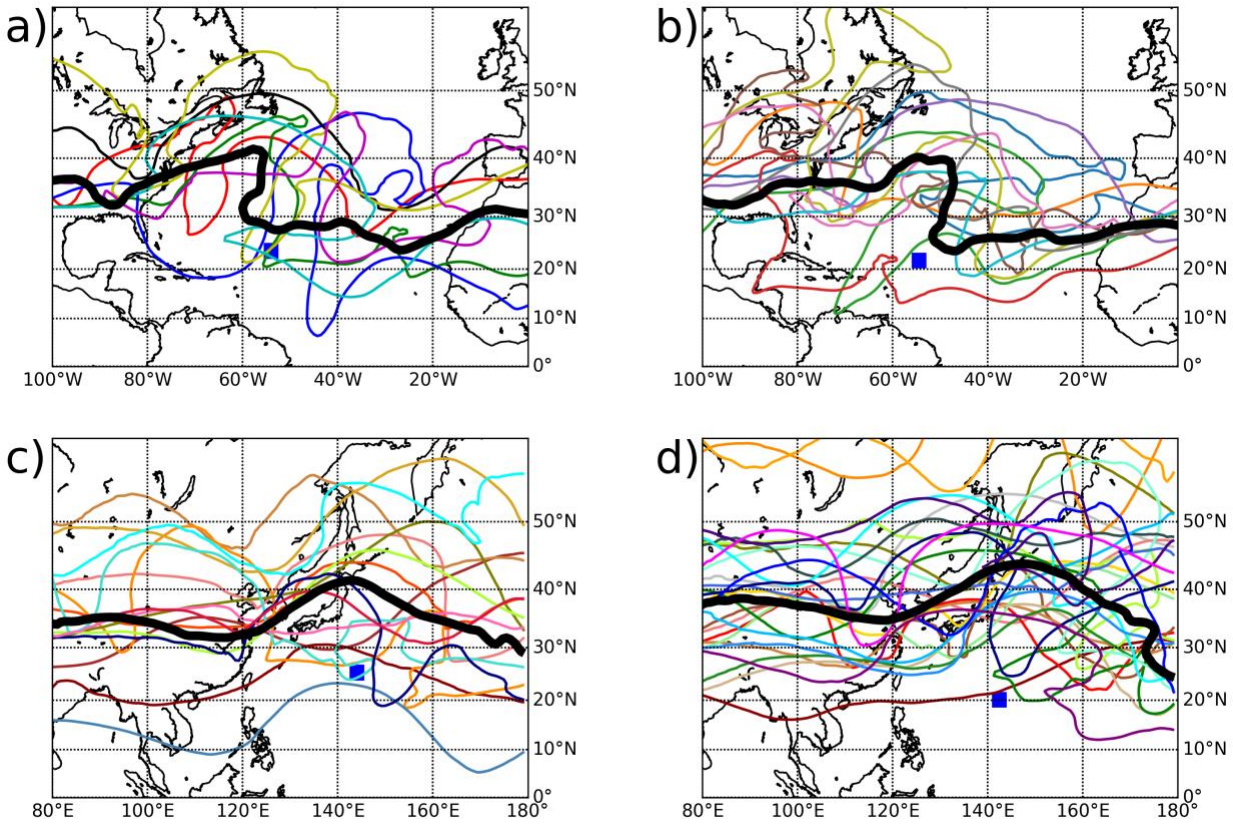

Figure 1.5. Analysis of the 2-PVU contour on the 340 K isentropic surface (taken as a proxy for the midlatitude waveguide) averaged from 48-h before the time of maximum interaction to 48-h after the time of maximum interaction for (a) the seven weakening North Atlantic, (b) the ten strengthening North Atlantic, (c) the fifteen weakening western North Pacific, and (d) the twenty-eight strengthening western North Pacific secondary TCs. Each individual waveguide is shown with different colored skinny lines, whereas the composite-mean waveguide for each subset is shown by the bold black contour. The average location of the secondary TCs over the 96-h period from 48-h before the time of maximum interaction to 48-h after the time of maximum interaction is given by the blue square.

Changes in the secondary TCs' translation speed and intensity during and after the indirect-interaction event are small on average but highly variable between cases. For instance, there is little change in average translation speed occurring after the time of maximum interaction for the secondary TCs (Fig. 1.6c,d). There are also minimal impacts to intensity (in terms of maximum wind speed) for the secondary TCs, with a 7-kt mean increase in intensity for the North Atlantic (Fig. 1.6a) and 6-kt mean increase for the western North Pacific (Fig. 1.6b) over the period from the time of maximum interaction to 48 h after. However, there is substantial case-to-case variability in intensity and translation speed before, during, and after the indirect-interaction event, as shown by the large differences between the strengthening and weakening cases in both basins (Fig. 1.6a,b). These findings are consistent with Peirano et al. (2016) and Fischer et al. (2019), as those studies highlighted significant distinctions in terms of how TC intensity changes as it encounters a trough, with these differences being largely tied to the flow geometry associated with the upstream trough and suggest the need for case-to-case diagnosis.

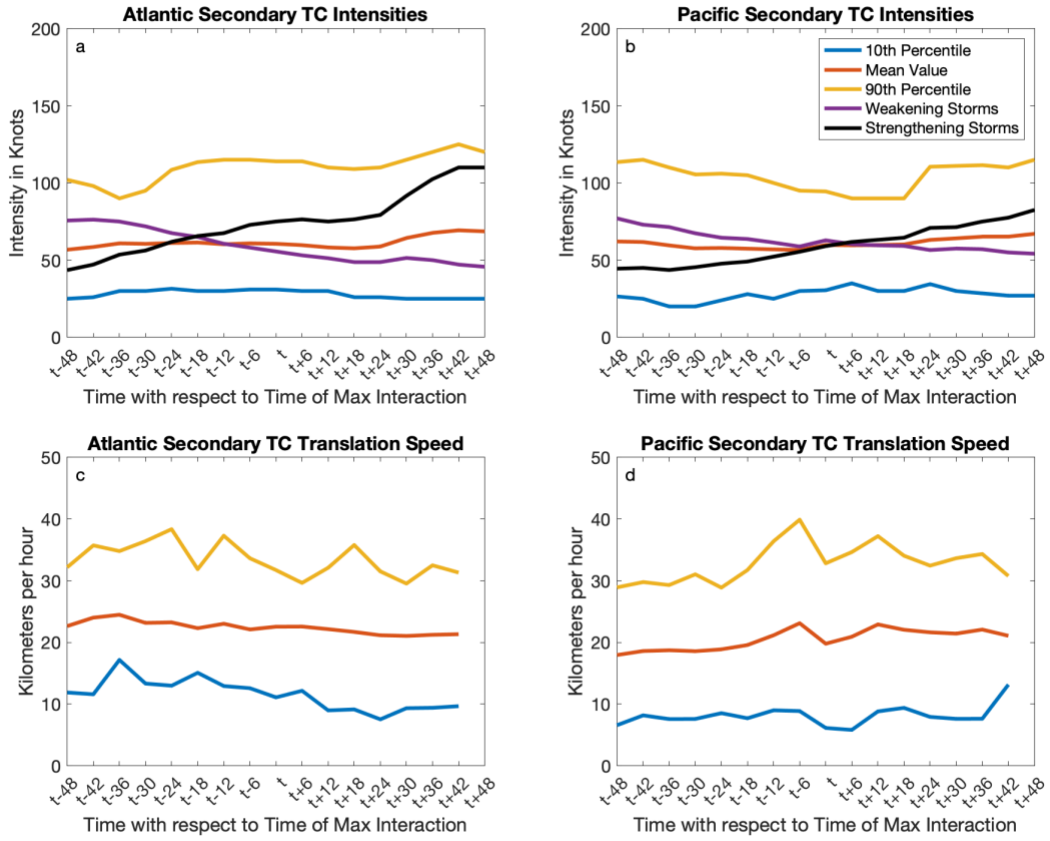

Figure 1.6. Secondary TC (a, b) intensity (kt) and (c, d) translation speeds (km h^{-1}) for the (a, c) North Atlantic and (b, d) western North Pacific (right column) basins. The blue line represents the 10th percentile of the dataset, the red line represents the mean, and the orange line represents the 90th percentile. All fields are shown at six-hour increments from 48-h prior to through 48-h after the time of maximum interaction between the primary TCs and the midlatitude waveguide. The weakening and strengthening subsets are the same as those identified in Tables 1.3 and 1.4.

With an average separation distance between the primary and secondary TCs of 2065 km in the North Atlantic and 1630 km in the western North Pacific at the time of maximum interaction, the primary and second TCs are sufficiently distant from each other for any potential influence of the primary TC on the secondary TC to largely be indirect rather than direct. For instance, although upwelling locally reduces SST along the primary TCs' paths (section 1.4.1), a majority of secondary TCs follow a track sufficiently distant from those of their predecessor primary TCs to not be significantly impacted by this upwelling and its associated atmospheric impacts (not shown). Further, the separation between the primary and secondary TCs exceeds the ~1,500 km maximum separation distance required for mutual rotation of each TC about the other to occur (Fujiwhara 1921). However, the primary TCs are sufficiently close to their respective secondary TCs to impart a weak steering current (in the composite mean) across the secondary TCs. Inverting the 850-200 hPa layer-mean relative vorticity within 4.5° of the primary TCs' center (following Galarneau and Davis 2013 and Papin 2017) at the time of maximum interaction results in a 850-200 hPa layer- and composite-mean nondivergent wind of 0.57 m s^{-1} in the North Atlantic and 0.71 m s^{-1} in the western North Pacific across the secondary TCs, albeit with significant variability between cases (standard deviation of 0.57 m s^{-1} in the North Atlantic, 0.77 m s^{-1} in the western North Pacific).

1.4 Synoptic Composites

Two compositing approaches are used to document the large-scale flow reconfiguration associated with the indirect-interaction events described in the previous section. The first, a maximum-interaction-centered approach (section 1.4.1), is used to identify the composite-mean impacts of the primary TCs' interaction with the midlatitude waveguide on downstream subtropical to midlatitude pattern (section 1.4.1). The second, a secondary-TC-centered approach

(section 1.4.2), is used to document variability in the reconfigured large-scale pattern between secondary TCs that strengthen and weaken during indirect-interaction events.

1.4.1 Composite-mean impacts of primary TCs on their synoptic-scale environments and the midlatitude waveguide

The onset of an indirect-interaction event, occurring between 48- and 24-h prior to the time of maximum interaction in each basin, is characterized by large composite-mean negative PV advection by the irrotational wind resulting from the composite-mean upper-tropospheric outflow associated with the composite-mean primary TCs impinging upon the antecedent midlatitude waveguide (Figs. 1.7-1.8a,b). Concurrently, the ventilation index is anomalously high to the south-southeast of the composite-mean location of maximum interaction in both basins (Fig. 1.9a,d); however, this primarily reflects the direct influence of the composite-mean primary TCs on their immediate environments. The anomalously high ventilation index values largely result from anomalously weak composite-mean MPI (Fig. 1.10a,d), anomalously high composite-mean entropy deficit (Fig. 1.11a,d) and, to lesser extent, anomalously high composite-mean 850-200 hPa vertical wind shear (Fig. 1.12a,d). Upwelling induced by the primary TCs is the cause of the anomalously weak MPI and anomalously large entropy deficit (see Appendix A; Hart et al. 2007; Schenkel and Hart 2015). The areas of statistical significance are larger in spatial extent for the western North Pacific than for the North Atlantic, which is hypothesized to be due to the smaller spread of primary TC locations (and thus greater local impact that rises to the level of statistical significance) in the western North Pacific (Fig. 1.4).

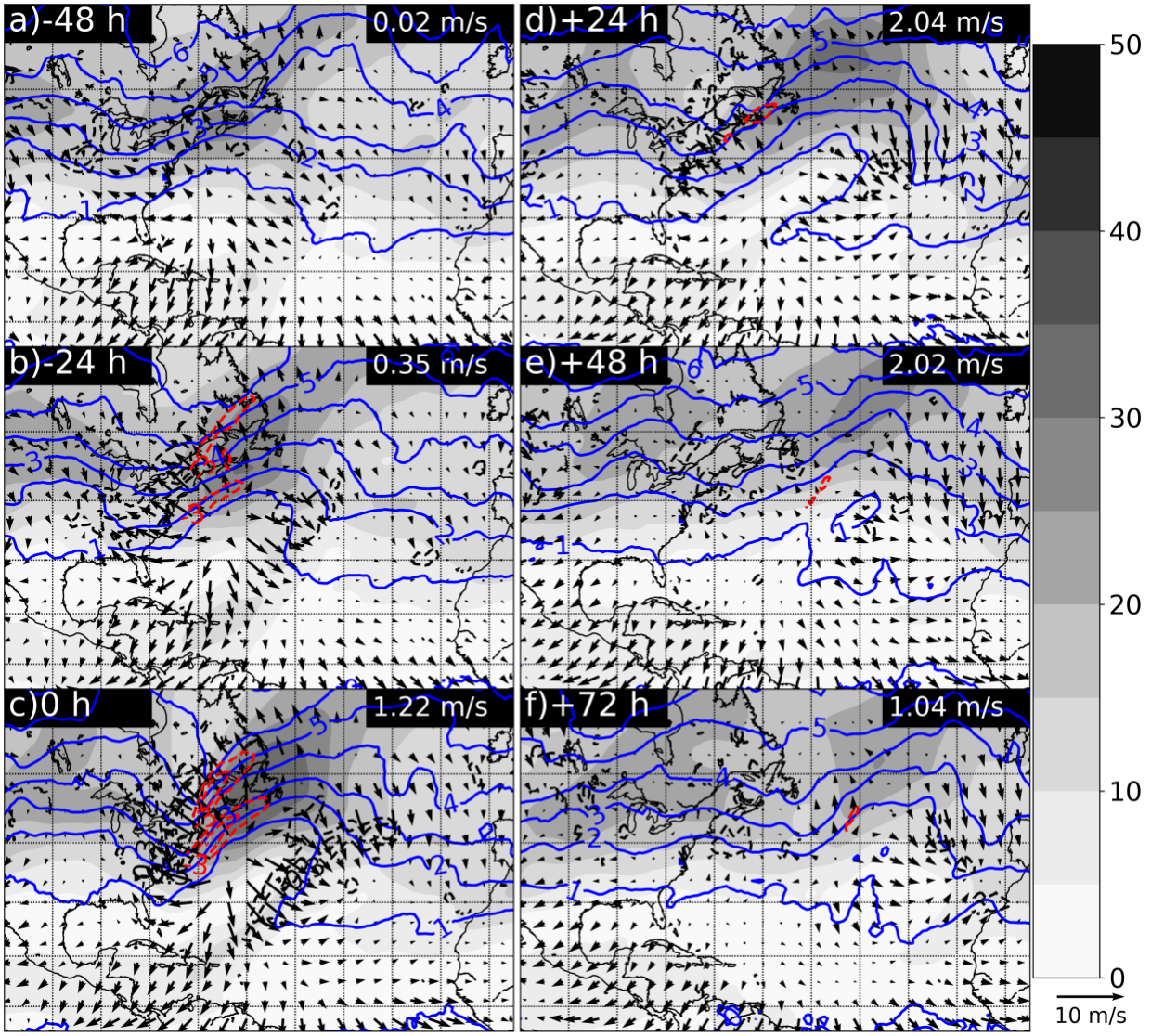

Figure 1.7. Maximum-interaction-centered composite-mean 250-150 hPa layer-mean PV (blue contours every 1 PVU starting at 1 PVU), 250-150 hPa layer-mean horizontal wind speed (grey shading in m s^{-1} per the color bar at right), 250-150 hPa layer-mean irrotational wind (vectors in m s^{-1}; reference vector at lower right), 250-150 hPa layer-mean PV advection by the layer-mean irrotational wind (red-dashed contours every -3 PVU day^{-1} starting at -3 PVU day^{-1}), and 250-150 hPa layer-mean divergence (black-dashed contours every -0.3 * 10^{-5} s^{-1} starting at 0 s^{-1}) every 24 h from (a) 48 h before the time of maximum interaction to (h) 120 h after the time of maximum interaction for the North Atlantic basin (n = 26). Latitude and longitude grid lines are drawn every 10˚. Meridional-flow index anomalies (defined as in Archambault et al. 2013 relative to a 1980-2010 monthly-mean climatology between 20-50°N, 80-20°W; units: m s^{-1}) are plotted in white text in the upper-right corner of each panel. Note that spatial composites are centered on the composite-mean location of the maximum interaction, such that the geography highlighted on the map is for spatial reference only.

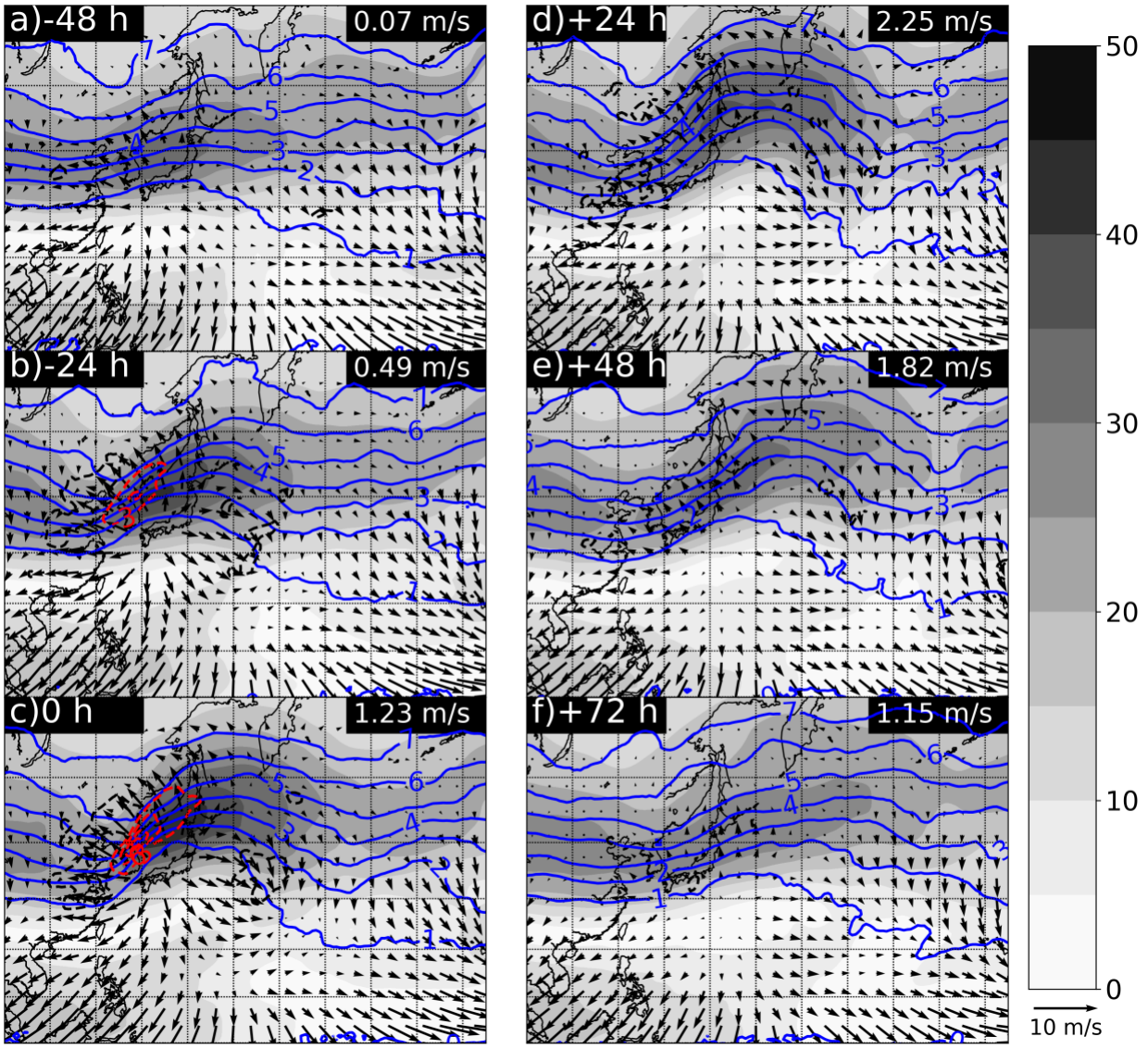

Figure 1.8. As in Fig. 1.7, except for the western North Pacific basin (n = 56). The spatial bounds for the meridional-flow index anomalies in this figure are 20-50°N, 140°E-120°E.

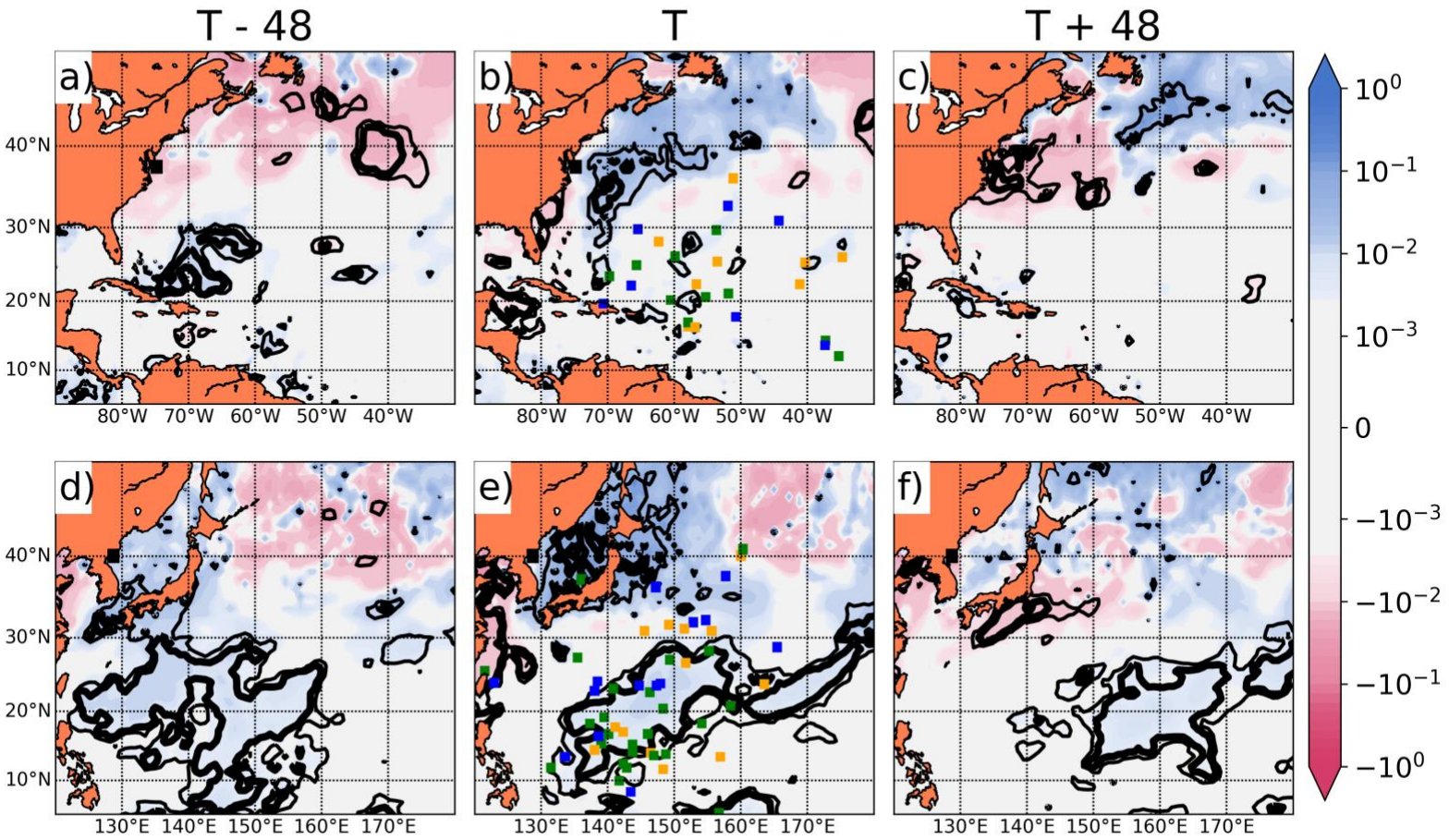
T - 48
T
T + 48
a)
b)
c)
d)
e)
f)
40°N
30°N
20°N
10°N
80°W 70°W 60°W 50°W 40°W
130°E 140°E 150°E 160°E 170°E
10^0
10^{-1}
10^{-2}
10^{-3}
0
-10^{-3}
-10^{-2}
-10^{-1}
-10^0

Figure 1.9. Maximum-interaction-centered composite-mean ventilation index anomaly (shaded per the logarithmic color bar at right; blue shading represents higher ventilation index values and a less conducive environment to TC formation and maintenance and red shading represents lower values more supportive of TC formation and maintenance) every 48 h from (a, d) 48-h before the time of maximum interaction to (c, f) 48-h after the time of maximum interaction. The thin black line denotes anomalies that are statistically significant to at least 95% confidence and the thick black line denotes anomalies that are statistically significant to at least 99% confidence. Panels (a-c) represent the North Atlantic composite whereas panels (d-f) represent the western North Pacific composite. Black squares in each panel indicate the composite-mean location of maximum interaction. Orange squares in panels (b) and (e) indicate the shifted locations of the secondary TCs (relative to the composite-mean primary TC location) at the time of maximum interaction for all TCs which did not change in intensity from 48 hours before the time of maximum interaction to 48 hours after, blue squares indicate the shifted locations of the secondary TCs that weakened, and green squares indicate the shifted locations of secondary TCs that strengthened.

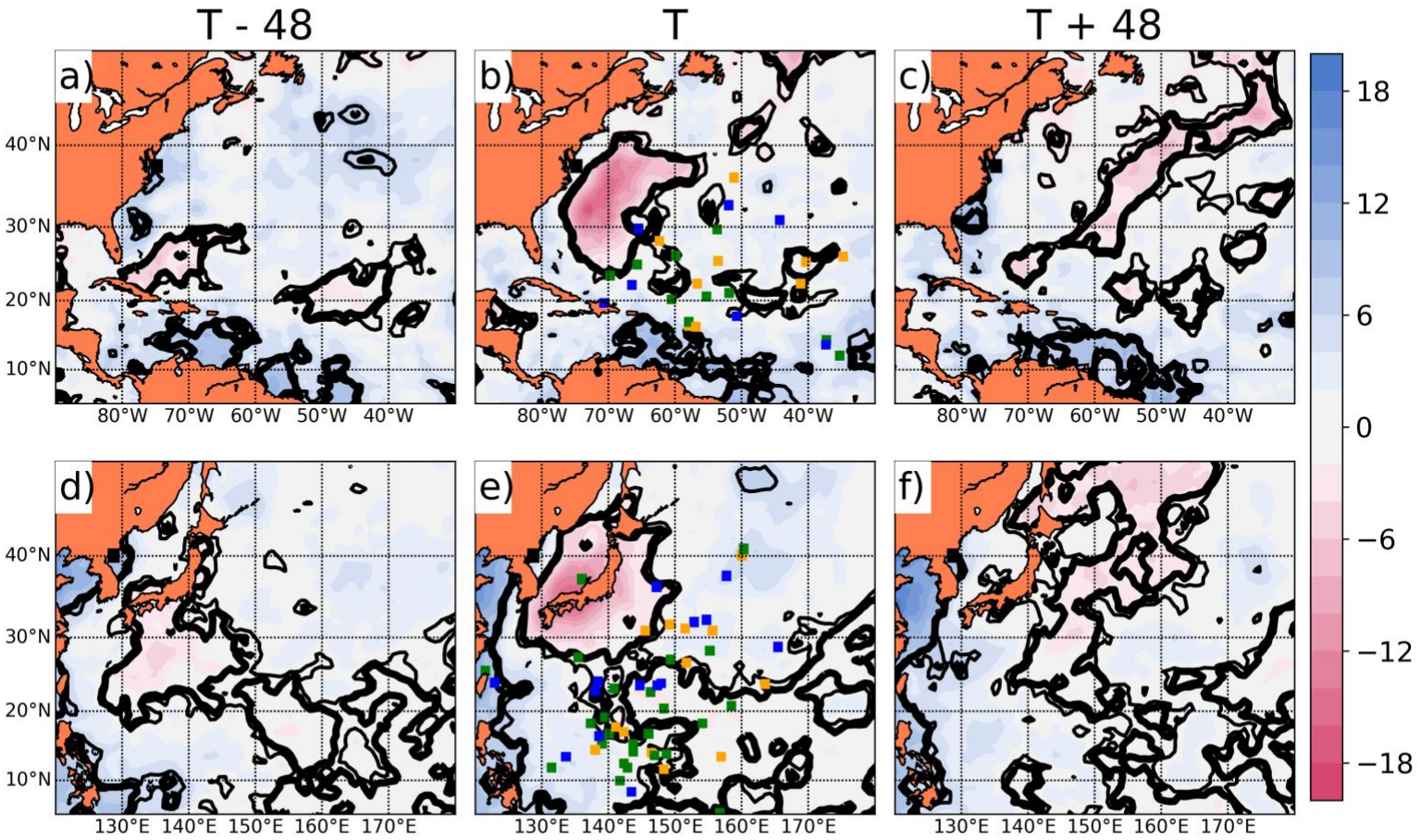
T - 48
T
T + 48
a)
b)
c)
d)
e)
f)
40°N
30°N
20°N
10°N
80°W 70°W 60°W 50°W 40°W
130°E 140°E 150°E 160°E 170°E
18
12
6
0
−6
−12
−18

Figure 1.10. As in Fig. 1.9, except for the MPI (units: m s^{-1}, shaded per the linear color bar at right) component of the ventilation index. Blue shading represents higher MPI and a more conducive environment to TC formation and maintenance and red shading represents lower MPI and a less conducive environment to TC formation and maintenance.

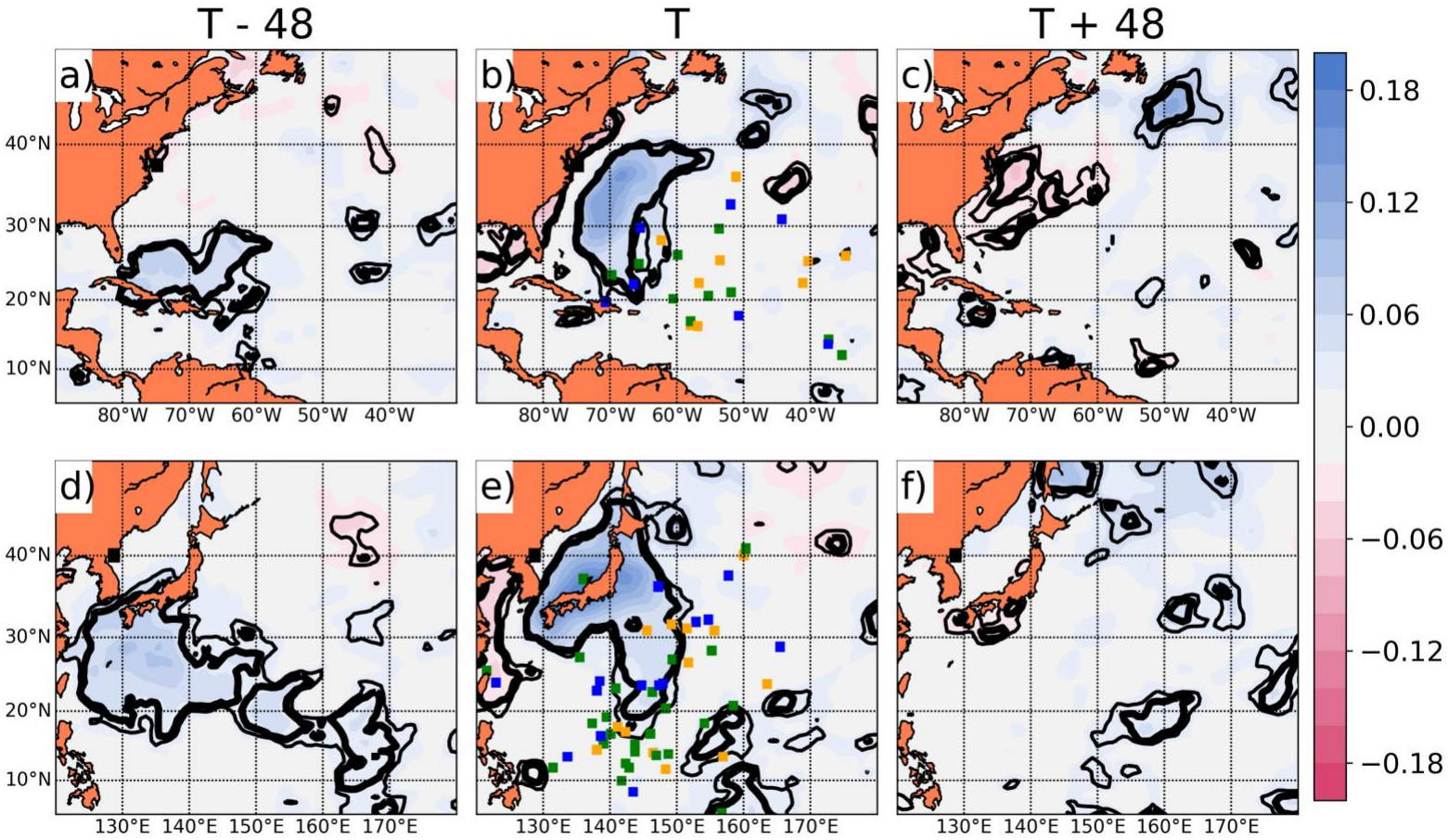
T - 48
T
T + 48
a)
b)
c)
d)
e)
f)
40°N
30°N
20°N
10°N
80°W 70°W 60°W 50°W 40°W
130°E 140°E 150°E 160°E 170°E
0.18
0.12
0.06
0.00
−0.06
−0.12
−0.18

Figure 1.11. As in Fig. 1.9, except for the entropy deficit (units: nondimensional; shaded per the linear color bar at right) component of the ventilation index. Blue shading represents larger entropy deficits representative of a less conducive environment to TC formation and maintenance and red shading represents smaller entropy deficit values representative of a more conducive environment to TC formation and maintenance.

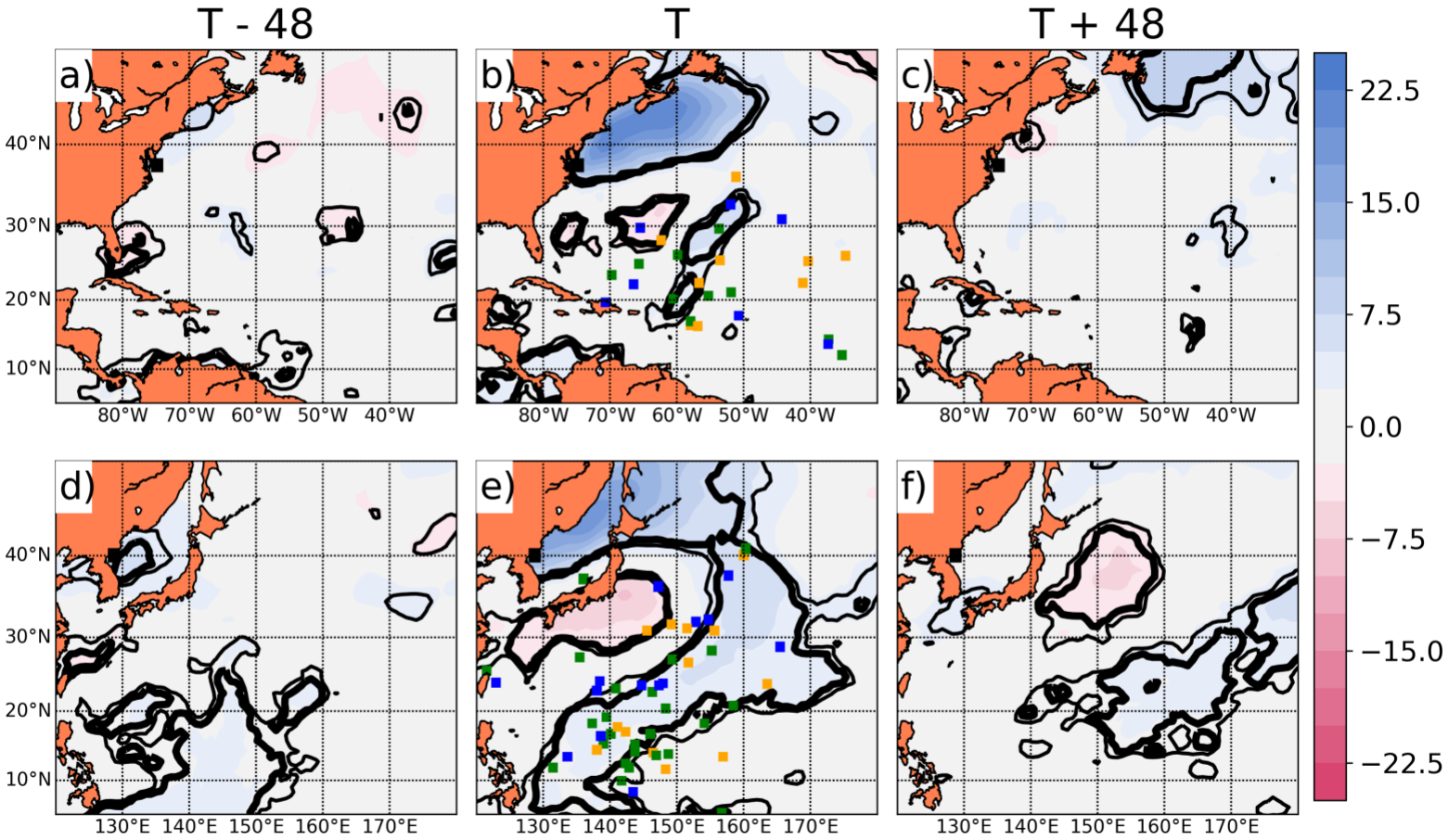
T - 48
T
T + 48
a)
b)
c)
d)
e)
f)
40°N
30°N
20°N
10°N
80°W 70°W 60°W 50°W 40°W
130°E 140°E 150°E 160°E 170°E
22.5
15.0
7.5
0.0
−7.5
−15.0
−22.5

Figure 1.12. As in Fig. 1.9, except for the 850-200 hPa vertical wind shear magnitude (units: m s^{-1}; shaded per the linear color bar at right) component of the ventilation index. Blue shading represents larger 850-200 hPa vertical wind shear values representative of a less conducive environment to TC formation and maintenance and red shading represents smaller 850-200 hPa vertical wind shear values representative of a more conducive environment to TC formation and maintenance.

By the time of maximum interaction, the primary TC has already been interacting with the midlatitude waveguide for approximately one-to-two days. Over these one-to-two days, a tightening of the horizontal PV gradient between the primary TC and the upstream trough results in local jet-streak formation and the initial amplification of the downstream midlatitude waveguide (Figs. 1.7c, 1.8c). This initial flow reconfiguration is associated with midtropospheric descent implied by convergent upper-tropospheric wind equatorward and on the eastern flank of the immediate downstream ridge (Figs. 1.7c, 1.8c), which can inhibit the formation of deep, moist convection and promote the intrusion of dry air from aloft into any TCs in the vicinity (Gray 1968). In the context of the ventilation index, anomalously high ventilation index values are aligned along a meridional corridor following the poleward movement of the primary TCs (Fig. 1.9b,e). As at earlier times, the anomalously large ventilation index values result from anomalously weak composite-mean MPI (Fig. 1.10b,e) and anomalously high composite-mean entropy deficit (Fig. 1.11b,e), both of which are again a result of upwelling along the primary TCs' track, as well as anomalously high composite-mean 850-200 hPa vertical wind shear (Fig. 1.12b,e). Elsewhere, anomalously large 850-200 hPa vertical wind shear magnitude is found in both basins in association with the amplified midlatitude jet, primarily poleward of the amplified downstream ridge, and anomalously low 850-200 hPa vertical wind shear is found near the center of this ridge (Fig. 1.12b,e). In the western North Pacific, however, anomalously large vertical wind shear also extends *equatorward* of the downstream amplified ridge, encompassing the locations of many of the secondary TCs (Fig. 1.12e).

Within 24-h after the time of maximum interaction, anomalously large composite-mean 250 – 150 hPa layer averaged PV (to the 99% confidence level; not shown) extends to the southwest on the equatorward side of the downstream ridge in the North Atlantic (Fig. 1.7d),

indicative of anticyclonic wave breaking (Thorncroft et al. 1993). This may suggest that the environment in which some secondary TCs are embedded becomes less conducive to TC development and maintenance, as anticyclonic wave breaking and associated PV streamer formation can (depending on where a TC is located relative to these features) increase vertical wind shear and the associated intrusion of cool and dry midlatitude air into a TCs circulation (Galarneau et al. 2015; Zhang et al. 2017; Zhang and Wang 2018). Anticyclonic wave breaking is not evident in the western North Pacific composite (Fig. 1.8d), however, consistent with the longer, stronger midlatitude jet along the midlatitude waveguide being more resilient against Rossby wave breaking (Wirth et al. 2018).

By two days after the time of maximum interaction, there is a significant degradation in the signal in the North Atlantic, consistent with Pohorsky et al. (2019), associated with the termination of the initiated composite-mean Rossby wave packet due to wave breaking (Fig. 1.7e). Concurrently, many of the statistically significant impacts to the ventilation index and its components directly resulting from the interaction of the primary TCs with the midlatitude waveguide have moved well into the midlatitudes and/or become indistinct (Figs. 1.9-1.12c). In the western North Pacific, however, the downstream signal remains detectable through three days after the time of maximum interaction (Fig. 1.8e,f). Anomalously large ventilation indices remain present over the subtropical portion of the western North Pacific (Fig. 1.9f), which at this time are almost exclusively the result of anomalously large vertical wind shear equatorward of the first downstream ridge (Fig. 1.12f).

1.4.2 Composite-mean secondary-TC-centered environments

Although the interaction of a primary TC with the midlatitude waveguide results in the amplification of the composite-mean downstream pattern, there is significant variability in

secondary TC locations (colored squares in Fig. 1.9b,e) relative to the midlatitude pattern. This motivates a composite analysis centered on the secondary TCs. For this analysis, secondary TCs are stratified by whether they intensified or weakened (here defined by whether their minimum sea-level pressure decreases or increases, respectively, by at least 5 hPa) over the 96-h period centered on the time of maximum interaction. As is shown below, this analysis demonstrates how the *position* of a secondary TC relative to the amplified midlatitude waveguide, more so than details of the waveguide's amplification (e.g. wave-breaking or lack thereof, amplitude, latitude of waveguide, etc.), exerts the largest control on the outcome of an indirect-interaction event on a secondary TCs intensity. However, note that this analysis only establishes association and thus does not establish *causation*; i.e., the secondary TCs do not necessarily change intensity *as a result* of the indirect-interaction events.

In the North Atlantic, secondary TCs that intensify following an indirect-interaction event are equatorward of the downstream (relative to the primary TCs) ridge (Figs. 1.5b, 1.13a-c) in a low-to-moderate shear environment well-removed from the midlatitude waveguide (Table 1.3). Conversely, secondary TCs that weaken following an indirect-interaction event are displaced southeast of the downstream ridge, closer to the midlatitude waveguide in a moderate-shear environment (Table 1.3), through the time of maximum interaction (Figs. 1.5a, 1.14a-b). This impact is consistent with that for the case of North Atlantic TC Jose (2017), which is included within this composite subset, in Fig. 1.1, and for North Atlantic TCs Earl, Fiona, and Gaston (2010) described by Fowler and Galarneau (2017). Only by 48-h after the time of maximum interaction are these TCs situated equatorward of the downstream ridge (Fig. 1.14c).

Atlantic	Strengthening	Weakening	No Change
Count	10	7	9
Average normalized time in life (1 = last advisory, 0 = first advisory)	0.23	0.41	0.44
Average normalized intensity relative to MPI (1 = at MPI, 0 = 0 kt)	0.25	0.67	0.21
Average minimum sea-level pressure change (hPa)	-22.8 hPa	12.6 hPa	-0.67 hPa
Average 850-200 hPa vertical wind shear magnitude (in m s^{-1})	4.96 m s^{-1}	6.68 m s^{-1}	5.83 m s^{-1}
Average change in 850-200 hPa vertical wind shear magnitude(in m s^{-1})	2.08 m s^{-1}	-1.59 m s^{-1}	0.58 m s^{-1}
Average Latitude	21.8˚ N	23.6˚ N	23.7˚ N
Average Longitude	-54.5˚ W	-54˚ W	-50.4˚ W
Average great-circle distance from waveguide (km)	607.7 km	440.8 km	450 km

Table 1.3. Selected parameters for the secondary TCs in the North Atlantic basin, separated by whether the secondary TCs strengthened, weakened, or did not change intensity. A change in central pressure of less than 5 hPa over the 96-hour period from 48 hours before the time of maximum interaction to 48 hours after following the indirect-interaction event classified a TC as no change, an increase of 5 hPa or greater as weakening, and a decrease of 5 hPa or greater as strengthening. The average time in the life cycle is represented by a 0 for the beginning of the TCs life and a 1 for the ending. MPI is calculated following the calculation in Tang and Emanuel (2012) over a 5˚ by 5˚ moving domain located 48 h ahead of each secondary TC along its track to attain the environmental MPI (i.e., that uninfluenced by the TC). Vertical wind shear magnitude is calculated over a 5° by 5° moving domain following each secondary TC with the secondary TCs circulation removed using vorticity inversion.

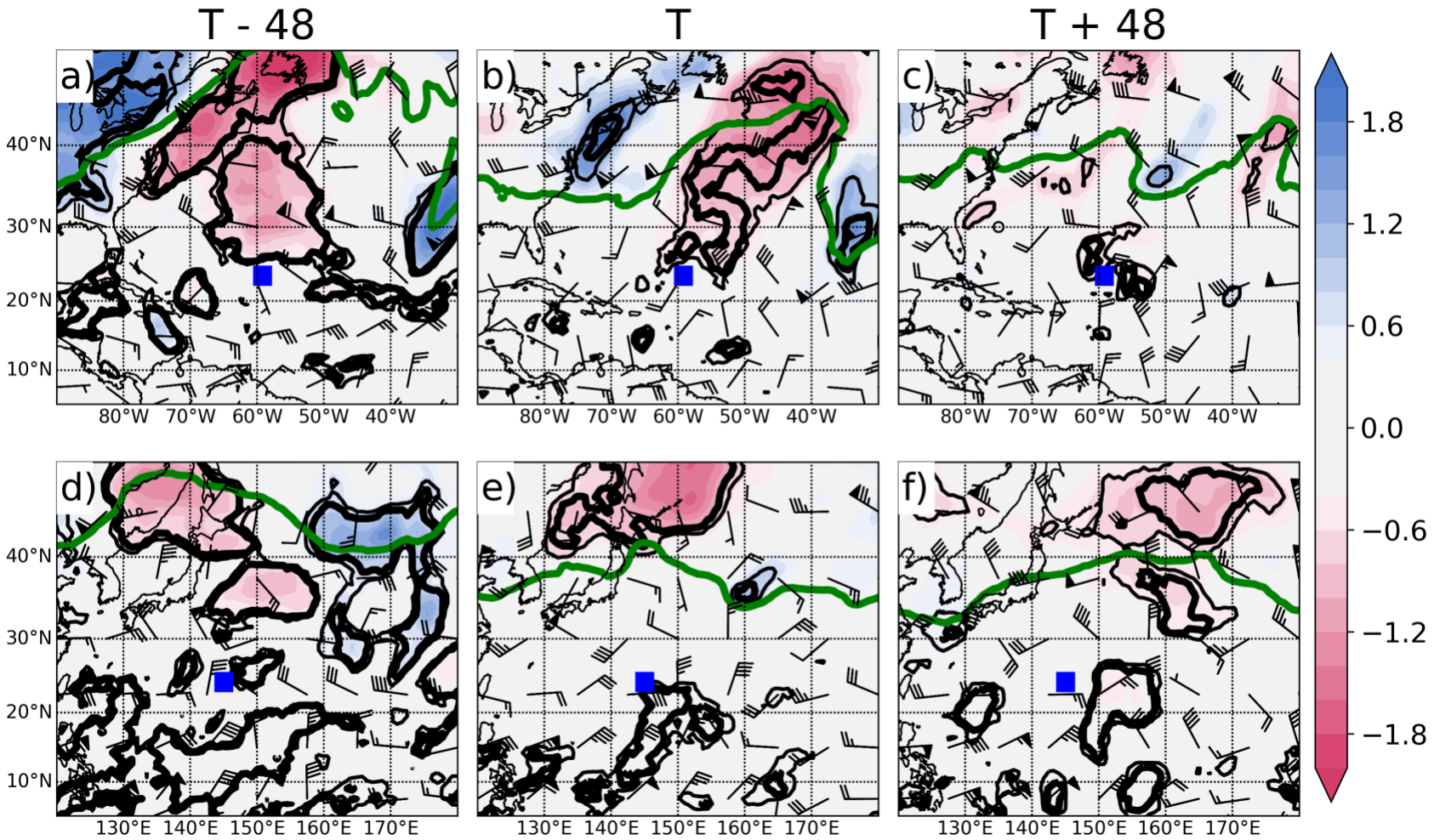
T - 48
T
T + 48
a)
b)
c)
d)
e)
f)
40°N
30°N
20°N
10°N
80°W 70°W 60°W 50°W 40°W
130°E 140°E 150°E 160°E 170°E
1.8
1.2
0.6
0.0
−0.6
−1.2
−1.8

Figure 1.13. Secondary-TC-centered composite-mean PV anomalies on the 340-K isentropic surface every 48 h from (a, d) 48-h before the time of maximum interaction to (c, f) 48-h after the time of maximum interaction for all strengthening secondary TCs (as given by the green squares in Fig. 9b,e). The thin black line denotes anomalies that are statistically significant to at least 95% confidence and the thick black line denotes anomalies that are statistically significant to at least 99% confidence. The thick green line represents the instantaneous 2 PVU level on the 340-K isentropic surface averaged over all strengthening cases in each respective basin. Panels (a-c) represent the North Atlantic composite whereas panels (d-f) represent the western North Pacific composite. The blue squares represent the average location of the secondary TCs at each time. The anomalies are computed by comparing raw values versus a climatology defined using a fifteen-day average centered on the date of each indirect-interaction event (the time of maximum interaction) over the period 1980-2010.

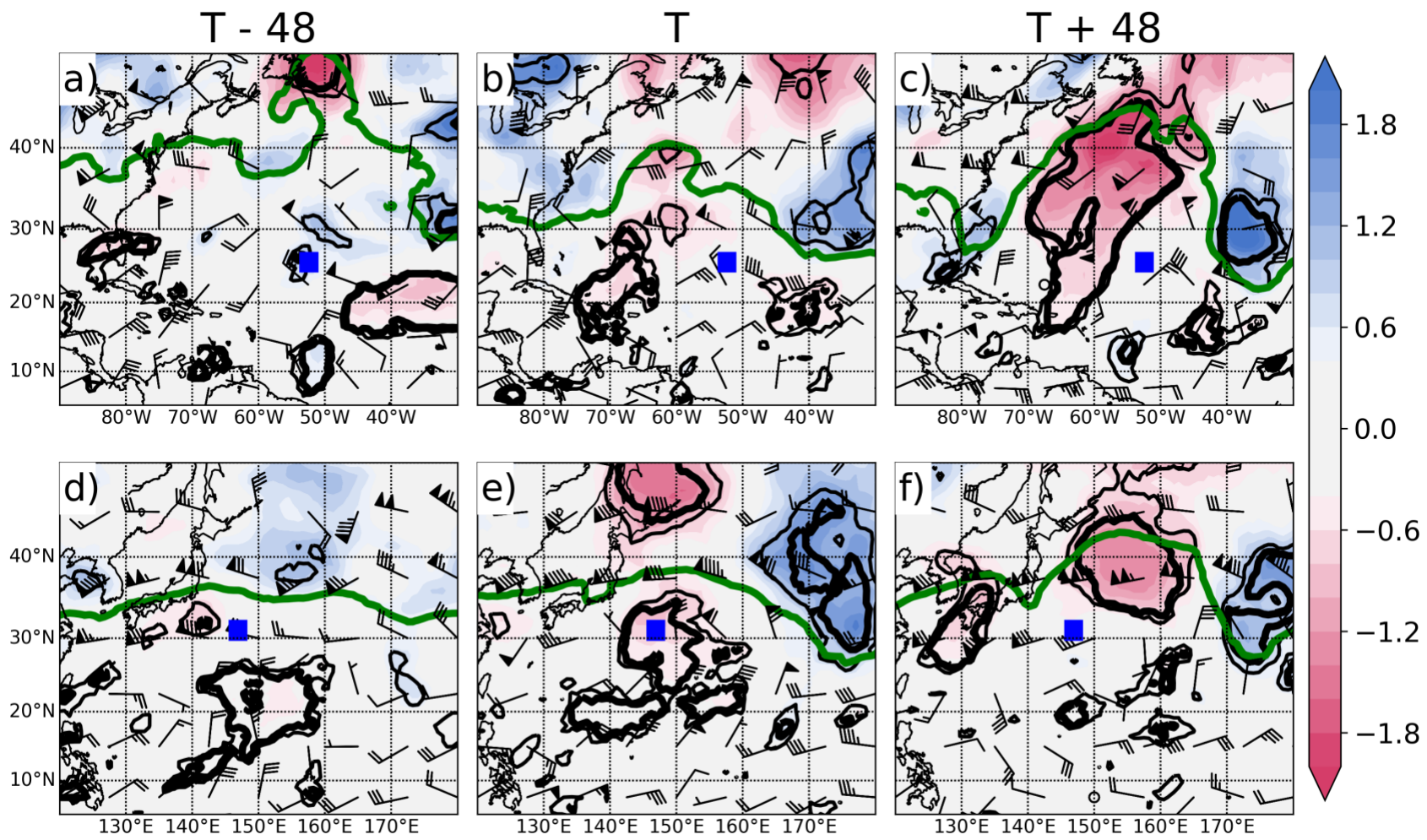

Figure 1.14. As in Fig. 1.13, except for all weakening TCs (as given by the blue squares in Fig. 1.9b,e).

In the western North Pacific, weakening versus strengthening secondary TCs primarily stratify by latitude, with strengthening secondary TCs being located significantly further south, further away from the midlatitude waveguide in a weaker-shear environment, as compared to their weakening counterparts (Table 1.4; Figs. 1.5cd, 1.13d-f, 1.14d-f). In these strengthening cases, the large-scale flow amplification is confined to latitudes poleward of the secondary TCs, such that these secondary TCs could be considered to *not* be indirect-interaction events given the apparent lack of impact of the primary TCs on these secondary TCs' environments. In contrast, the composite-mean signal for the weakening secondary TCs in the western North Pacific suggests that at least some of these TCs are interacting with the midlatitude waveguide themselves, as evidenced by the downstream ridge building from the composite-mean secondary TC position two days after the time of maximum interaction (Fig. 1.14f). Case-study analysis is necessary to document the extent to which the flow reconfiguration downstream of the primary TCs contributes to these weakening secondary TCs, however.

Pacific	Strengthening	Weakening	No Change
Count	28	15	13
Average normalized time in life (1 = last advisory, 0 = first advisory)	0.30	0.66	0.39
Average normalized intensity relative to MPI (1 = at MPI, 0 = 0 kt)	0.24	0.74	0.30
Average minimum sea-level pressure change (hPa)	-20.8 hPa	23.3 hPa	-0.6 hPa
Average 850-200 hPa vertical wind shear magnitude (m s^{-1})	2.62 m s^{-1}	5.22 m s^{-1}	4.28 m s^{-1}
Average change in 850-200 hPa vertical wind shear magnitude (m s^{-1})	0.02 m s^{-1}	4.21 m s^{-1}	1.11 m s^{-1}
Average latitude	19.9˚ N	25.4˚ N	24.2˚ N
Average longitude	142.3˚ E	144˚ E	152˚ E
Average great-circle distance from waveguide (km)	986.5 km	826.3 km	911.5 km

Table 1.4. As in Table 1.3, except for the 56 cases in the western North Pacific basin.

1.5 Impacts to Primary and Secondary TC Track and Intensity Predictability

The previous two sections have demonstrated the large-scale flow reconfiguration resulting from the interaction of a primary TC with the midlatitude waveguide and the conditions under which secondary TCs typically intensify or weaken during the indirect-interaction process. Given the basin-wide reduction in medium-range predictability for forecasts initialized one to two (or more) days prior to the interaction of a TC with the midlatitude waveguide (e.g., Harr and Archambault 2016), however, it is unclear as to the extent that these secondary TC outcomes are predictable. In this section, official track and intensity forecasts issued 24-48 h prior to time of maximum interaction are verified for both primary and secondary TCs to provide an answer (at least in part) to this question.

In terms of official track forecasts, forecasts of both primary and secondary TC tracks have slightly reduced predictability compared to climatology through 48 h after forecast issuance, but not to the 95% confidence level (Fig. 1.15a,c). However, consistent with previous studies (McTaggart-Cowan et al. 2007; Fowler and Galarneau 2017), official forecast track errors for the primary and secondary TCs in the western North Pacific and the secondary TCs in the North Atlantic are associated with significantly reduced predictability between 72-96 h after forecast issuance (Fig. 1.15a,c). While the cause for these increased errors is not immediately clear, one possibility is inaccuracies in forecasting the interaction of the primary TC with the upstream trough, which is well-known to be a significant source of forecast error in forecasts initialized prior to the time of maximum interaction (e.g., Komaromi et al. 2011; Scheck et al. 2011; Riemer and Jones 2014; Harr and Archambault 2016; Keller et al. 2019). In these forecasts, small errors in numerical model forecasts originating near the interaction point

between the primary TC and midlatitude waveguide can propagate downstream and grow, ultimately impacting the skill of official track forecasts that are partially based off of numerical model forecasts.

Conversely, in terms of official intensity forecasts, only forecasts of North Atlantic primary TCs verifying at 12-48 h after forecast issuance are associated with reduced predictability compared to climatology (Fig. 1.15b). In fact, in the western North Pacific, both the primary and secondary TCs are associated with statistically significantly *increased* predictability at 72-, 96-, and 120-h (Fig. 1.15d). This is an unexpected result, particularly given the significantly reduced track predictability at these lead times (Fig. 1.15b). However, the sample sizes at these forecast times (particularly 96- and 120-h) are very small, such that only a few TCs (which may be outliers) contribute to the results shown (Fig. 1.15). While preliminary findings suggest very little correlation between increased wind shear and increased predictability of the downstream TCs, potential future research could determine whether TCs in regions of large tropospheric-deep wind shear are slightly more predictable due to the high likelihood that the TC will weaken given that other parameters important to intensification/maintenance are not met (e.g. warm SSTs and high midtropospheric water content; Rios-Berrios and Torn 2017) or not. Additionally, while a diagnosis of the secondary storms does not reveal a correlation between improved forecast skill with storms which systematically weakened post-interaction, there is an average improvement in skill (with respect to baseline forecasts from the OCD5 [Operational Intensity blend of the Climatology and Persistence and Decary SHIFOR models] for the North Atlantic and from the ST5D [5 day STIFOR model] in the western North Pacific) of approximately 40% at later forecast times (particularly 72- and 96-h).

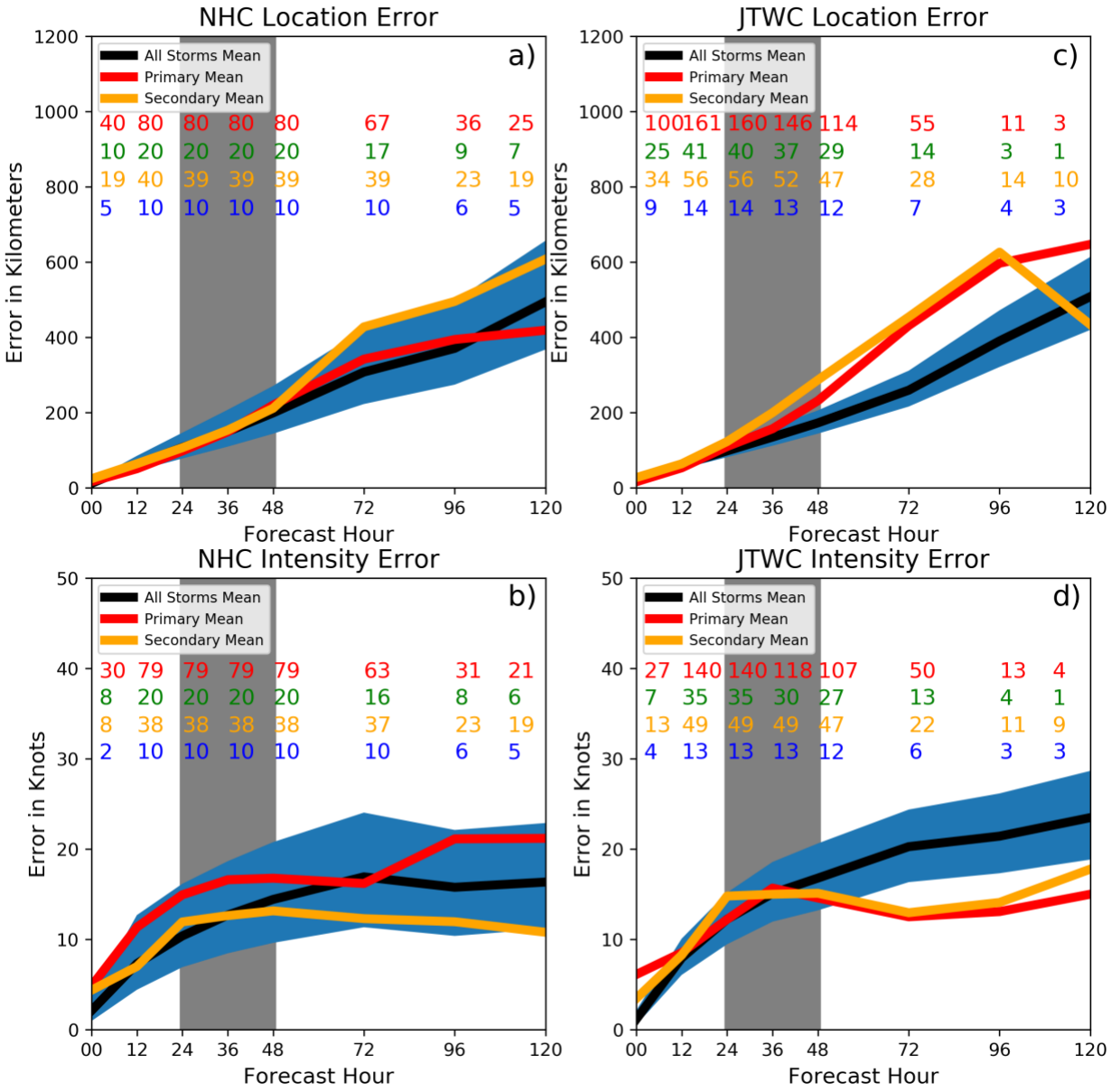

Figure 1.15. NHC-forecast (a) track (great-circle distance in km) and (c) intensity (kt) error for all cases of all forecasts of primary (red) and secondary (orange) TCs initialized between 48 to 24 hours before the time of maximum interaction. The red and orange numbers represent the number of valid forecasts at that forecast lead time for the primary and secondary TCs, respectively. The green and blue numbers represent the number of TCs used in the averaging at that forecast lead time for the primary and secondary TCs, respectively. The black lines represent the mean error and the blue shading represents the 2.5th-97.5th percentiles of errors for all 1989-2018 TCs excluding the primary and secondary TCs (following the procedure described in section 2f). (b, d) As in (a, c), except for JTWC official forecasts. The 0-h forecast counts in this figure are lower due to the limited availability of these data.

1.6 Conclusions

Substantial research has been published on the interaction of TCs with the midlatitude flow as they recurve into the midlatitudes and undergo ET, including the associated reduction in downstream midlatitude predictability. Separately, others have published on the concurrence of multiple TCs within a given basin. However, only a limited number of case studies have been conducted to examine the influence, direct or indirect, that a recurving TC can have on the downstream subtropical to tropical environment, including secondary TCs located within such environments. This study represents an attempt to bridge this divide by creating a climatology of indirect TC interaction events facilitated by TC-waveguide interaction and using this climatology to document the associated flow reconfiguration in proximity to the secondary TCs.

Over the thirty-year period between 1989-2018, twenty-six and 56 indirect interactions are identified in the North Atlantic (Table 1.1) and western North Pacific (Table 1.2) basins, respectively. Consistent with previous studies (as synthesized in Keller et al. 2019) of TC-waveguide interactions, the interaction of a primary TC with the midlatitude waveguide results in significant downstream *midlatitude* flow reconfiguration, most notably in the amplification of the immediate downstream ridge, with impacts lasting up to two to three days after the time of maximum interaction (Fig. 1.16). However, with the exception of increased vertical wind shear equatorward of the amplified downstream ridge in the western North Pacific (Fig. 1.12d-f), most of the associated environmental impacts are confined to the midlatitudes. Additionally, it was found that while upwelling from the primary TCs can impact the environment immediately surrounding them, there are no impacts to the secondary TCs (see Appendix A).

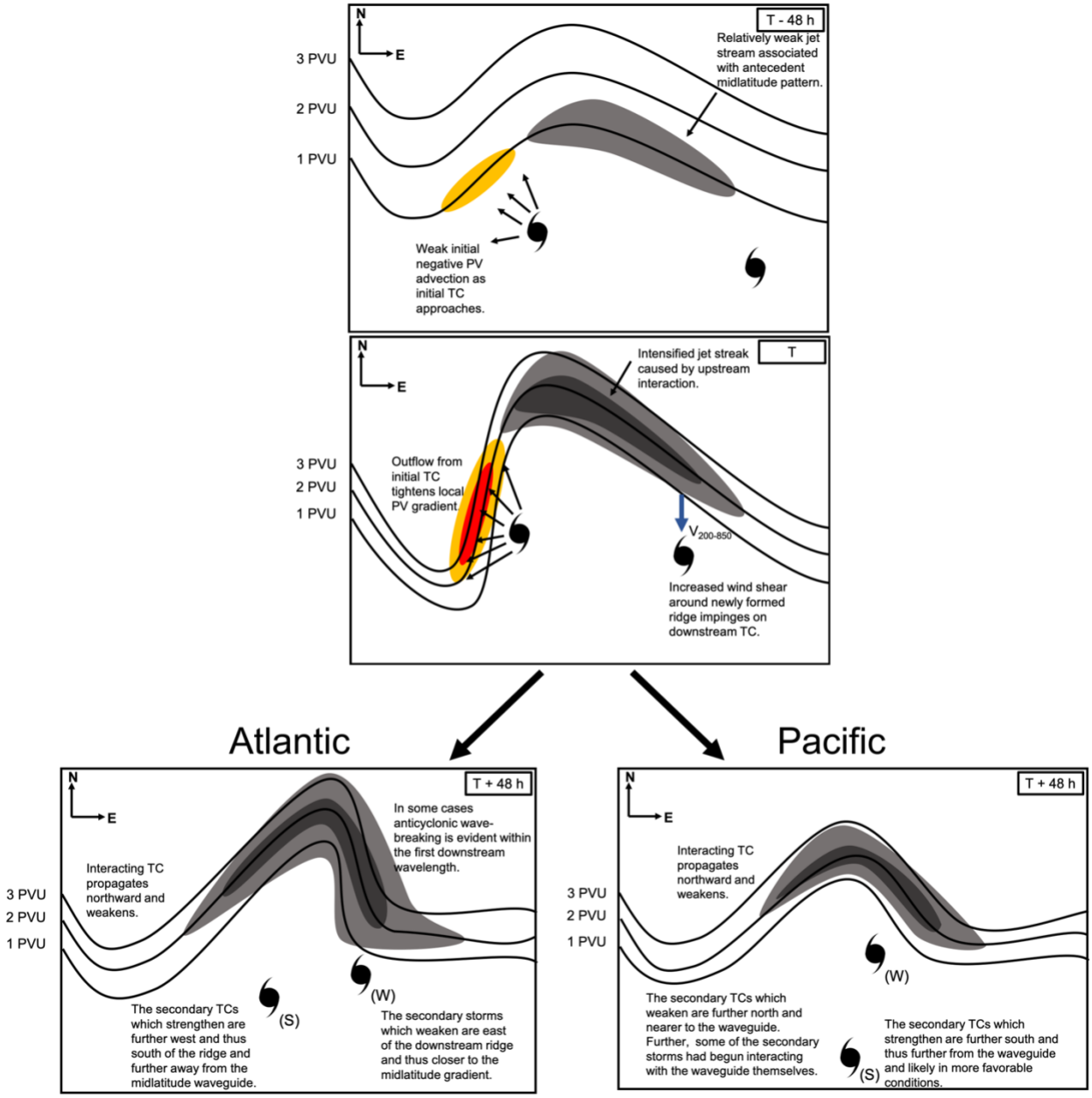

Figure 1.16. Conceptual schematic of the downstream flow reconfiguration and associated environmental changes associated with a primary TCs interaction with the midlatitude waveguide every 48 h between (top) 48-h before the time of maximum interaction and (bottom) 48-h after the time of maximum interaction. Black vectors denote the upper-tropospheric irrotational wind, orange and red shading denotes increasing levels of negative PV advection by the upper-tropospheric irrotational wind, and grey shading denotes increasing upper-tropospheric wind speed. The bottom row is split between the North Atlantic and western North Pacific basins to highlight key differences between the two basins.

This study identifies two pathways by which a secondary TC can weaken following an indirect-interaction event. In the Atlantic, weakening secondary TCs are closer to the midlatitude waveguide on the southeastern edge of the amplified midlatitude ridge (consistent with Fowler and Galarneau 2017), whereas strengthening secondary TCs are further from the waveguide and equatorward of the amplified midlatitude ridge (Table 1.3; Fig. 1.16, bottom left). Conversely, western North Pacific strengthening and weakening secondary TCs are primarily stratified by latitude, with weakening secondary TCs located nearly 6° latitude poleward of their strengthening secondary TC counterparts at the time of maximum interaction, as opposed to their positions relative to the midlatitude pattern (Fig. 1.16, bottom right). Strengthening secondary TCs remain well-equatorward of the midlatitude waveguide and are largely unaffected by changes in the midlatitude flow, whereas weakening secondary TCs rapidly approach the midlatitude waveguide following the time of maximum interaction (Table 1.4; Fig. 1.16, bottom right). This insight can foster increased forecaster situational awareness during future indirect-interaction events that may allow them to make more-skillful secondary-TC intensity forecasts during and after the time of maximum interaction. That said, it is arguable as to the extent that the primary TCs' interaction with the midlatitude waveguide influences these outcomes in either basin; the outcomes depicted herein are merely associative rather than causative in the absence of case-study analyses utilizing numerical-model simulations with piecewise PV inversion techniques.

By definition, indirect-interaction events require there to be multiple concurrent TCs within a given basin, the likelihood of which is strongly governed by the seasonal cycle and modulated by sub-seasonal modes of variability such as the Madden-Julian Oscillation (MJO) and convectively coupled equatorial waves (Schenkel 2016 and references therein). The extent to

which these modes of variability project on the synoptic-scale midlatitude pattern before, during, and after an indirect-interaction event is unclear, however. That said, using archived MJO index data from the Australian Bureau of Meteorology, a significant portion of the western North Pacific interactions occur when the MJO is in phases 6 or 7 (not shown), consistent with previous research connecting increased TC activity in this basin to these MJO phases (Li and Zhou 2013; Klotzbach 2014). Likewise, most North Atlantic indirect-interaction events occur when the MJO is in phases 1 or 2 (not shown), which is also consistent with previous works connecting increased TC activity in the North Atlantic to these MJO phases (Klotzbach 2010, 2014). Thus, in both basins, indirect-interaction events are more frequent when multiple TCs themselves are more frequent. Further research is necessary to quantify the MJO's impact, if any, on the flow reconfigurations associated with these indirect-interaction events, however.

The analyses presented in this research motivate further research to better document indirect-interaction events and their impacts on secondary TCs' track and intensity. For instance, case studies are necessary to quantify the extent to which the primary TC in each case contributes to the subsequent downstream flow evolution and secondary TC track and intensity. Techniques such as piecewise PV inversion (e.g., Grams et al. 2013a,b), analog compositing (Pohorsky et al. 2019), and ensemble-based sensitivity analysis (e.g., Torn and Hakim 2015; Torn 2016), each as applied to the primary TC and/or antecedent midlatitude pattern, can be used to diagnose such sensitivities. Research is under way to do so for the indirect interaction between North Atlantic TCs Irma and Jose in 2017 described in section 1.1. Further, the use of the negative PV advection by the irrotational wind metric to identify indirect-interaction events leaves out other potential indirect-interaction pathways, including through Rossby wave radiation (Schenkel 2016, 2017; Krause and Sobel 2008) and primary-TC outflow into an upper-

tropospheric low that is in close proximity to another TC (e.g., TCs Rita and Philippe in 2005; Franklin 2006). This could motivate further research to diagnose the relative occurrence and importance of each pathway not only in the indirect interactions identified here but in a larger set of cases. Further, the forecast-error analysis presented herein focuses only on forecasts issued by official warning centers, which represent expert syntheses of a wide range of available model guidance and observational data. However, numerical modeling systems likely have varying skill for these events (e.g., Keller et al. 2011), and future research to quantify such skill variations may provide insight into the synoptic-scale conditions and/or model configuration parameters that lead to particularly enhanced or degraded forecast skill. Finally, the sample sizes of indirect-interaction events in both basins are small, and the subsets of events by the secondary TCs' intensity evolution are even smaller. Future research using a longer climatology (albeit subject to increasingly large uncertainty at earlier times) and/or global coupled ocean-atmosphere model output is warranted to constrain the analysis uncertainty resulting from these small sample sizes.

Chapter 2

A Case-Study Analysis of Convective-Scale Contributions to Midlatitude Waveguide Preconditioning Preceding a Tropical Cyclone-Midlatitude Waveguide Interaction

As previously noted, global forecast models such as the Global Forecast System (GFS) or European Centre for Medium-Range Weather Forecasts (ECMWF) Integrated Forecast System can struggle to accurately represent the interaction between a TC and the midlatitude waveguide, leading to large forecast errors downstream. The source of this error has been hypothesized to be the misrepresentation of convective-scale processes, and the intense diabatic hearting associated with it, in TC-trough interaction (Anwender et al. 2008). While the current horizontal and vertical resolutions of both the GFS and ECMWF models can resolve the impact stratiform heating profiles have on the moist potential temperature field, convective-scale processes will still be parameterized. This naturally leads to the question of if the source of error in TC-midlatitude waveguide interactions (and the indirect interactions discussed in Section 1) is the misrepresentation of convective-scale processes and, if so, how do these errors contribute to the larger scales (e.g., physically how do convective-scale processes meaningfully impact the large-scale flow)? The work in this section has been provisionally accepted for publication in the *Journal of the Atmospheric Sciences*.

2.1 Introduction

The recurvature of a TC from the tropics or subtropics into the midlatitudes may lead to highly amplified midlatitude waveguide patterns locally and downstream from the recurving TC

due to interaction between the TC and an upstream midlatitude trough. In a TC-trough interaction, strong latent heat release inside of the TC leads to the vertical redistribution of low potential-vorticity (PV) air into the upper troposphere. When the interaction is favorable, the TC recurves east of the bifurcation point (Riemer and Jones 2014), in which the low PV air in the core of the TC is then diabatically driven radially away from the TCs core by the TCs secondary circulation against the eastern flank of an upstream midlatitude trough. This advection of near-zero PV air tightens the local PV gradient on the east side of the trough, leading to local jet streak formation and subsequent downstream impacts which can last for several days (Archambault et al. 2013, 2015; Grams and Archambault 2016; Grams et al. 2011, 2013a,b). Outcomes of TC-trough interactions depend on the inertial stability of the jet (as dictated by the jet speed and latitude), the shape and phase speed of the upstream trough, and the magnitude of the TCs outflow (Finocchio and Doyle 2019; Komaromi and Doyle 2018; Riemer and Jones 2014). The impacts from TC-trough interactions can extend several thousand kilometers downstream, with recent downstream high-impact weather such as indirect TC interactions (Prince and Evans 2020), high-impact precipitation events (Pohorsky et al. 2019), blocking anticyclones (Riboldi et al. 2019), and the formation of PV streamers (Keller 2017; Quinting and Jones 2016; Riemer et al. 2008; Riemer and Jones 2010) being attributed to upstream TC-trough interactions.

Interactions between TCs and the midlatitude waveguide may be occasionally accompanied by preconditioning (Grams and Archambault 2016). Preconditioning is often manifest in the form of a predecessor rain event (PRE), a meso- and/or subsynoptic-scale region of high-impact heavy rainfall well in advance of a recurving TC (Cote 2007; Galarneau et al. 2010). Warm, moist air advected poleward by a TCs outer circulation impinges upon a baroclinic

zone 500-2000 km away (Bosart and Carr 1978), whereupon it ascends and generates a broad region of stratiform precipitation with embedded deep, moist convection. The vertical gradient of diabatic warming in both deep, moist convection and stratiform precipitation reduces upper-tropospheric potential vorticity (PV) through vertical redistribution. Diabatically driven divergent outflow above the PRE radially advects this low-PV air away from the PRE near the tropopause (Keller et al. 2019). This diabatically driven negative PV advection aloft associated with convective and stratiform precipitation inside of the PRE is analogous to the diabatically driven negative PV advection aloft by a TCs secondary circulation (Archambault et al. 2013), which can assist with anchoring of the midlatitude jet and the diabatic formation of a Rossby wave (Grams et al. 2011; Grams and Archambault 2016; Keller et al. 2019).

On synoptic scales, it is often assumed that vertical diabatic-heating gradients are the primary contributors to isentropic PV non-conservation following the motion, with horizontal diabatic-heating gradients having a secondary, often negligible contribution. Consequently, the PV tendency equation along an isentropic surface is often written as:

$$\frac{D}{Dt}PV \approx \frac{1}{\sigma}(\zeta + f)\frac{\partial \dot{\theta}}{\partial p} \tag{2.1}$$

where $\sigma = -\frac{1}{g}\frac{\partial p}{\partial \theta}$, ζ is the relative vorticity, p is pressure, $\dot{\theta}$ is the diabatic heating rate, θ is potential temperature, g is gravity, and f is the Coriolis parameter. However, (2.1) does not hold in the presence of strong horizontal diabatic-heating gradients, such as those found with individual thunderstorms.

On thunderstorm scales, deep, moist convection in a vertically sheared background flow can generate PV anomalies with values an order of magnitude larger than typical synoptic-scale PV anomalies (Chagnon and Gray 2009; Oertel et al. 2020). In a PV framework, this is

represented by intense horizontal gradients of diabatic warming $\dot{\theta}$ (Chagnon and Gray 2009), which are not represented in (2.1) and require the fully three-dimensional form written as:

$$\frac{D}{Dt}PV = -\frac{1}{\sigma}\left[(\nabla \times \vec{v} + fk) \cdot \nabla_\theta \dot{\theta}\right] \quad (2.2)$$

where $\vec{v}_\theta = (u, v, \dot{\theta})$ represents the three-dimensional wind on an isentropic surface, $\nabla = (\partial_x, \partial_y, \partial_\theta)$ represents the three-dimensional gradient operator on an isentropic surface, and $k = (0,0,1)$ represents the unit vector perpendicular to an isentropic surface.

This process is analogous to the tilting of horizontal vorticity into the vertical by a localized updraft that produces cyclonic and anticyclonic circulations straddling the updraft (e.g., Davies-Jones 1986). The structure of these anomalies is dictated by the direction of the vertical wind shear vector, with negative PV anomalies resulting to the left of the deep-layer vertical wind shear vector and positive PV anomalies resulting to the right of the deep-layer vertical wind shear vector (Oertel et al. 2020). Given a primarily westerly background vertical wind shear vector in the midlatitudes, convection inside of a PRE equatorward of the midlatitude waveguide between the jet and a recurving TC would produce convective-scale strongly negative PV poleward of the convective cell, against the waveguide (see Fig. 1 of Oertel et al. 2020).

While the PV anomalies produced by a single thunderstorm are small in scale and individually insignificant on the synoptic scales, a collection of organized thunderstorms may cause a meaningful impact to the large-scale flow by opposing the background horizontal flow and generating a distinct negative anomaly in wind speed (Oertel and Schemm 2022). However, whether these impacts are meaningful on the meso-$\propto$ to sub-synoptic scales has yet to be determined. Energy in large-scale turbulence is generally thought to cascade into progressively smaller eddies, eventually reaching the Kolmogorov scale where viscosity dominates, and turbulent kinetic energy is dissipated into heat (Pope 2000). In some cases, however, an inverse

energy cascade (Kraichnan 1967) may transfer energy from smaller to larger scales (Eyink 2005ab; Chen et al. 2006; Xiao et al. 2009). In this context, small-scale features add energy to the large-scale flow, which has been hypothesized to be supported by a 'thinning' of small-scale vorticity anomalies by the large-scale flow; however, the physical mechanism by which this inverse cascade is accomplished is an ongoing discussion.

This study tests the hypothesis that deep, moist convection associated with a PRE modified the synoptic-scale midlatitude waveguide in a recent TC-midlatitude waveguide interaction by way of the production of convective-scale intensely negative PV against the waveguide by deep, moist convection A convection-allowing simulation of the PRE in advance of North Atlantic TC Irma (2017)'s interaction with the midlatitude waveguide is performed to test this hypothesis.

2.2 Methods

2.2.1 Case Overview

The PRE associated with North Atlantic TC Irma in September 2017 (Fig. 2.1), which caused approximately $50 billion in damage in Florida (NHC 2018), is selected for study. TC Irma's interaction with an upstream midlatitude trough following the PRE amplified the initial downstream anticyclone, which in turn influenced the track and intensity of the downstream TC Jose (Prince and Evans 2020).

At 1200 UTC 10 September 2017, TC Irma is located in the Florida Straits (Fig. 2.1, denoted by I) downstream of a midlatitude trough over the southeastern United States (Fig. 2.1). A PRE is located along the southeast United States coastline, poleward of TC Irma and eastward of the midlatitude trough (Fig. 2.1; denoted by P). Upper-tropospheric outflow associated with the PRE and TC Irma's outer rainbands is impinging upon the upstream trough's eastern flank,

as characterized by upper-tropospheric negative PV advection by the irrotational wind (Fig. 2.1), which subsequently strengthens the upper-tropospheric PV gradient on the trough's eastern flank. Following this time, TC Irma favorably interacts with the upstream trough, amplifying the downstream flow, trapping TC Jose equatorward of the downstream upper-tropospheric anticyclone within a high-shear environment (Prince and Evans 2020).

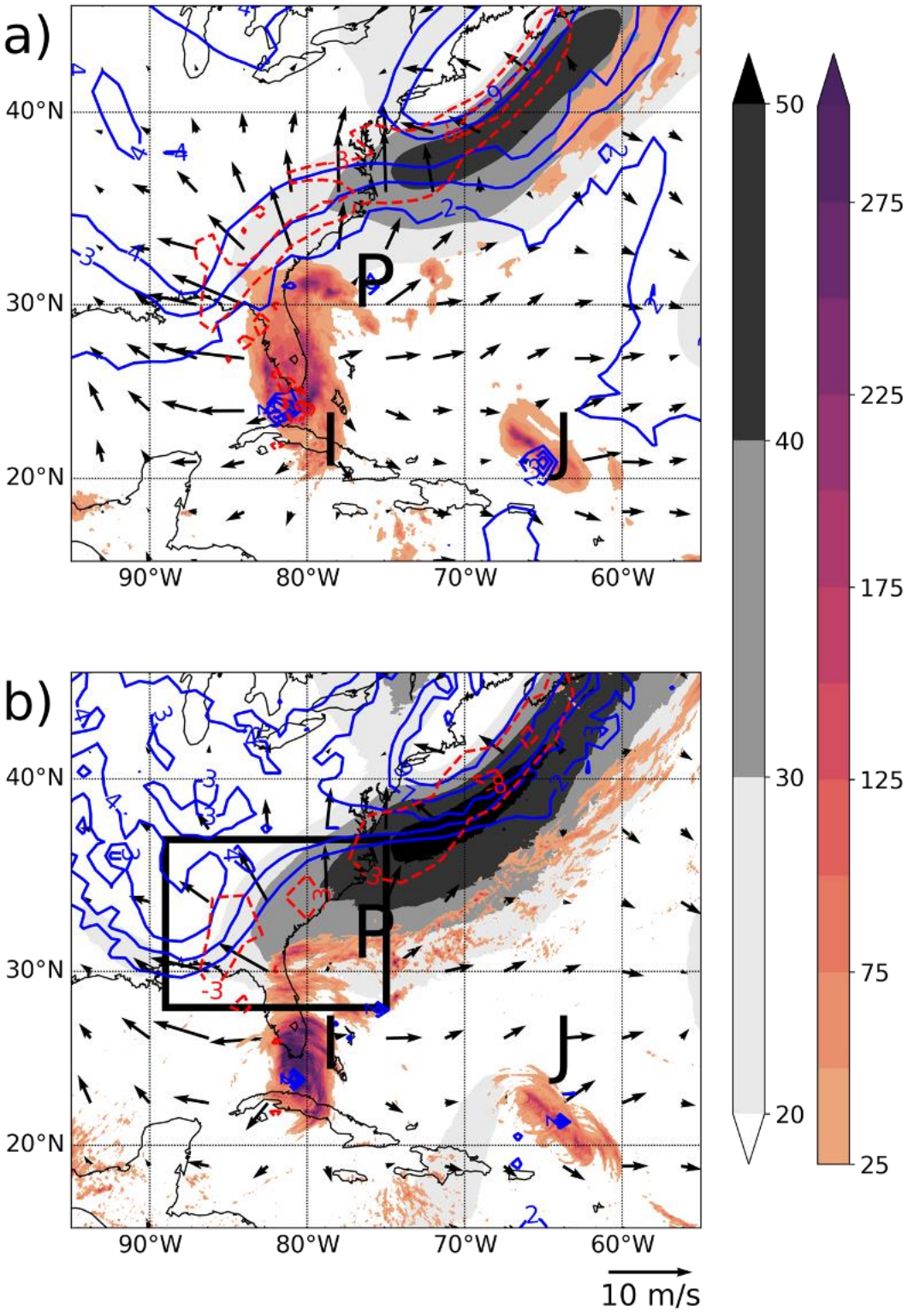
a)
40°N
30°N
20°N
90°W
80°W
70°W
60°W
P
I
J
b)
40°N
30°N
20°N
90°W
80°W
70°W
60°W
P
I
J
10 m/s
50
40
30
20
275
225
175
125
75
25

Figure 2.1. 250-150 hPa layer-mean PV (blue contours at 2, 3, 4, 7, and 9 PVU, where 1 PVU = 1 x 10^{-6} m^2 s^{-1} K kg^{-1}), 250-150 hPa layer-mean horizontal wind speed (grey shading in m s^{-1} per the color bar at right), 250-150 hPa layer-mean irrotational wind (vectors; m s^{-1}; reference vector at lower right), horizontal advection of the 250-150 hPa layer-mean potential vorticity by the 250-150 hPa layer-mean irrotational wind (red-dashed contours at -8 and -3 PVU day^{-1}), and 24-h (0000 – 2359 UTC) accumulated precipitation (color shading in mm per the color bar at right) at 1200 UTC 10 September 2017. (a) from the ERA5 reanalysis (Hersbach et al. 2020) except for 24-h accumulated precipitation, which is obtained from the 0.1˚ X 0.1˚ NASA Integrated Multi-Satellite Retrievals for GPM (IMERG; Huffman et al. 2019) version 06 dataset, and (b) from the numerical simulation performed in this study (described below). TC Irma, TC Jose, and the PRE are indicated by the bold I, J, and P, respectively. The black box in subplot b denotes the region over which all area-averages are performed in this study.

2.2.2 Simulation Configuration

A single numerical simulation is performed using the Advanced Research version of the Weather Research and Forecast (WRF-ARW) mesoscale model version 4.0 (Skamarock et al. 2019). The WRF-ARW is a fully compressible, nonhydrostatic numerical model. A doubly nested domain is utilized, with the outer domain containing 1000 X 1250 horizontal grid points at a grid spacing of 9 km and the inner domain containing 1753 X 2002 horizontal grid points at a grid spacing of 3 km (Fig. 2.2). Both domains contain 50 terrain-following (σ) vertical levels, including seven vertical levels near the tropopause ($0.15 \leq \sigma \leq 0.25$). The simulation extends 180 h from 0000 UTC 9 September 2017 to 1200 UTC 16 September 2017. The initialization time ensures appropriate spin-up time of circulations which the initial conditions are unable to represent before the initiation of the PRE (~1200 UTC 9 Sep 2017). The simulation's long duration allows for verification of the downstream midlatitude evolution following the PRE (and, subsequently, TC Irma) with the upstream trough. Initial and lateral boundary conditions for the model are provided by 6-hourly 0.25˚ National Centers for Environmental Prediction (NCEP) Global Forecast System (GFS; NCEP 2015). Physical parameterizations are selected following previous TC modeling studies using the WRF-ARW model (e.g., Torn and Davis 2012; Rios-Berrios et al. 2015). A full list of model configuration parameters is given in Table 2.1.

Model Parameter	Selected Configuration
Model Version	WRF-ARW v4.0 (Skamarock et al. 2019)
Domains	Domain 1 (outer), 1000 X 1250 X 50 levels Domain 2 (inner), 1753 X 2002 X 50 levels
Duration	180 h, 0000 UTC 09 September to 1200 UTC 16 September 2017
Horizontal Grid Spacing	9 km (Domain 1), 3 km (Domain 2)
Initial and Boundary Conditions	6-hourly 0.25˚ GFS operational analyses
Deep Cumulus Parameterization	Domain 1: New Tiedtke parameterization (Zhang and Wang 2017) Domain 2: No parameterization
Microphysical Parameterization	WRF Single-moment 6-class parameterization (Hong and Lim 2006)
Boundary-Layer Parameterization	YSU (Hong et al. 2006)
Surface-Layer Parameterization	Revised MM5 parameterization (Jimenez et al. 2012)
Land Surface Parameterization	Unified Noah Land Surface Model (Tewari et al. 2004)
Longwave Radiation Parameterization	RRTM parameterization (Mlawer et al. 1997)
Shortwave Radiation Parameterization	Dudhia parameterization (Dudhia 1989)

Table 2.1. Model configuration. Unless specified, all parameters apply to both the outer and inner simulation domains.

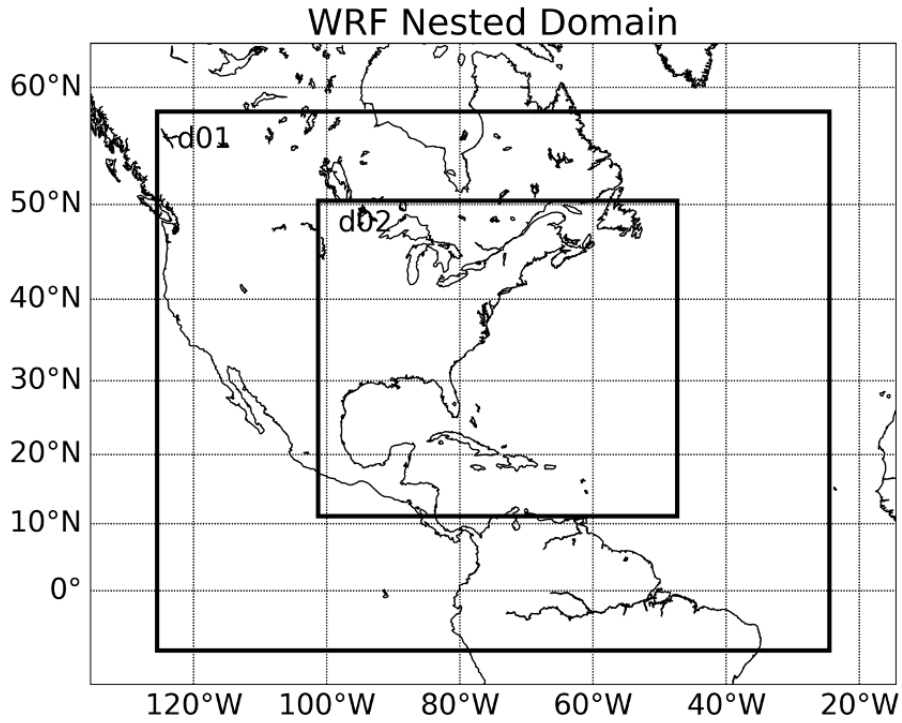

Figure 2.2. Simulation domain.

2.2.3 PV Tendency Equation in Isentropic Coordinates

The three-dimensional PV tendency equation on an isentropic surface, including nonhydrostatic effects but excluding friction, non-microphysical diabatic processes, and contributions from the planetary boundary layer parameterization (due to the scale of these processes being several orders of magnitude smaller than the microphysical tendency), is an expanded form of (2.2) comprised of adiabatic advective and diabatic nonconservative tendencies:

$$\frac{\partial PV}{\partial t} = -\vec{v} \cdot \nabla PV + PV\frac{\partial \dot{\theta}_{mp}}{\partial \theta} - \frac{1}{\sigma}\left[(\nabla \times \vec{v} + fk) \cdot \nabla_\theta \dot{\theta}_{mp}\right] \quad (2.3)$$

where $\vec{v} = (u, v, \dot{\theta})$ represents the three-dimensional wind, $\nabla = (\partial_x, \partial_y, \partial_\theta)$ represents the three-dimensional gradient operator on an isentropic surface, $k = (0,0,1)$ represents the unit vector perpendicular to an isentropic surface, $\dot{\theta}_{mp}$ represents the microphysical diabatic heating (H_DIABATIC in the WRF-ARW model), and f represents the planetary vorticity. In (2.3), the first right- side term represents the conservative (adiabatic) three-dimensional advection of PV, the second right-side term represents the nonconservative diabatically driven vertical redistribution of isentropic potential vorticity, and the third right-side term represents the nonconservative diabatically driven horizontal redistribution of potential vorticity. (2.3) is evaluated using model outputs at three-minute intervals to capture the short-lived nature of the convective elements in the simulation, with partial derivatives approximated utilizing a forward finite difference for time and a fourth-order–accurate centered finite difference for space. A derivation of (2.3) can be found in Appendix B.

2.2.4 Local Energy Flux and the Inverse Energy Cascade

To diagnose the potential impacts of convective-scale processes on the larger-scale flow, the local energy flux, which can be contextualized as the deformation work performed on small-

scale turbulent stress by large-scale strains (Eyink 2006ab; Chen et al. 2006; Xiao et al. 2009), is calculated. The local energy flux is negative when large-scale strains thin smaller-scale turbulent stresses, describing the situation where the larger-scale flow extracts kinetic energy from the turbulent anomalies.

To compute the local energy flux, the filtering approach demonstrated in Meneveau and Katz (2000) is first used to define a "large-scale" ($\overline{\boldsymbol{u}_\ell}$), where $\boldsymbol{u} = (u, v)$. In this approach, a "large-scale" velocity field at length scale ℓ is introduced using a low-pass filter,

$$\overline{\boldsymbol{u}_\ell} = \int dr\ G_\ell(r)\ \boldsymbol{u}(x + r) \tag{2.4}$$

where,

$$G_\ell(r) = \frac{1}{\ell^2} G(\frac{r}{\ell}) \tag{2.5}$$

and $G_\ell(r)$ can be any Gaussian function with unit integral (sum equal to one). Following Xiao et al. (2008), $G(r)$ is defined as,

$$G(r) = \sqrt{\frac{6}{\pi}} \exp\ (-6r^2) \tag{2.6}$$

where $G_\ell(r)$ represents a Gaussian convolution filter in physical space. An example of applying (2.6) to the two-dimensional horizontal wind on the 335-K isentropic surface is given in Fig. 2.3ab. A Gaussian convolution is selected over other potential convolution filters (such as spectral and box filters) because it is quasi-local in both physical and spectral space (Xiao et al. 2009), which allows the interpretation of the spatial properties at a particular length scale (ℓ) of the field being filtered. Note that the large-scale $\overline{\boldsymbol{u}_\ell}$ defined above is not identical to a Reynolds-averaged quantity, such that the average of perturbations is not equal to zero ($\overline{\boldsymbol{u}'_\ell} \neq 0$).

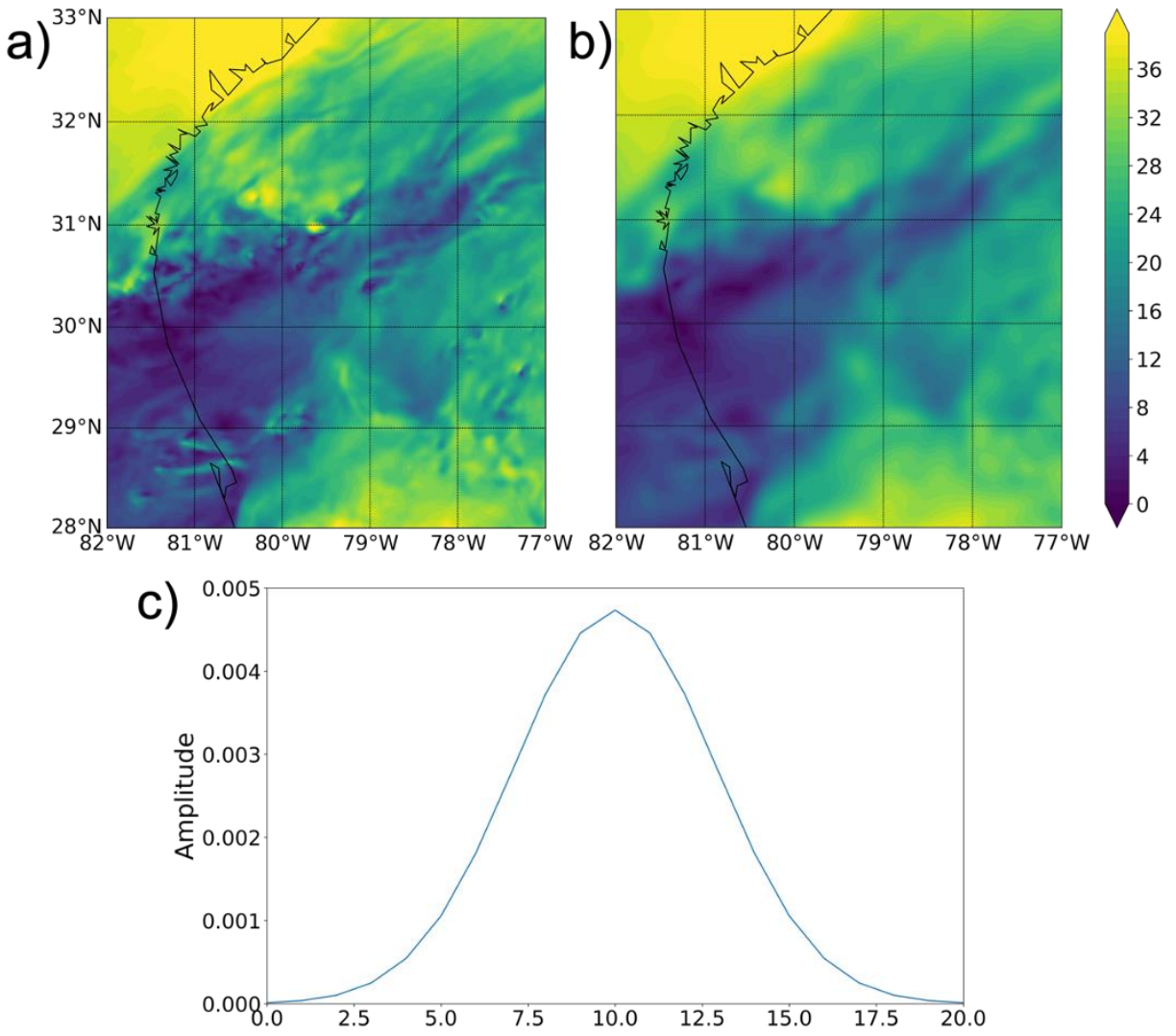

Figure 2.3. Horizontal wind speed on the 335-K isentropic surface (shaded in m s^{-1} per the color bar at right) at 0900 UTC 10 September 2017 (a) before and (b) after filtering applied by a (c) Gaussian filter with a length scale ℓ of 60 km (width of twenty grid points in the simulation domain, as shown by the x-axis).

The local energy flux across a particular length scale ℓ is defined as:

$$\Pi_\ell(x,t) = -\overline{S_\ell}(x,t) \cdot \tau_\ell \tag{2.7}$$

where $\overline{S_\ell}$ is the large scale-strain tensor, given by:

$$\overline{S_\ell} = \frac{1}{2}[(\nabla \overline{\boldsymbol{u}}_\ell) + (\nabla \overline{\boldsymbol{u}}_\ell)^T] \tag{2.8}$$

and τ_ℓ is the small-scale stress tensor, given by:

$$\tau_\ell = \overline{(\boldsymbol{uu})}_\ell - \overline{\boldsymbol{u}}_\ell \overline{\boldsymbol{u}}_\ell \tag{2.9}$$

The local energy flux (2.7) can alternatively be viewed as a deformation work (Eyink 2006ab; Xiao et al. 2009) done on small-scale turbulent stresses (τ_ℓ) by the large-scale strain field ($\overline{S_\ell}$). As a reminder, negative deformation work represents the large-scale strain extracting energy from small-scale turbulent stresses, characterizing an inverse cascade of energy from small to large scales, whereas positive deformation work represents the large-scale strain transferring energy to small-scale turbulent stresses. A full derivation of (2.7) from the filtered two-dimensional Navier-Stokes equations can be found in Xiao et al. (2009).

Although the local energy flux (2.7) can illustrate the direction of energy transfer in physical space, it is also necessary to evaluate the physical processes that contribute to energy changes in spectral space. The spectral kinetic energy budget first introduced by Peng et al. (2014a) and applied in Menchaca and Durran (2019) is used to do so. First, the horizontal kinetic energy budget can be defined as:

$$\frac{\partial}{\partial t} KE_h = T(k) + B(k) + V(k) + D(k) \tag{2.10}$$

where the subscript of *h* denotes horizontal, and *k* denotes the one-dimensional wavenumber. From right to left, the forcing terms of (2.10) represent the nonlinear advective transfer of energy between wavenumbers (*T*), the conversion of available potential energy to horizontal kinetic

energy (associated with buoyancy, *B*), the divergence of the vertical kinetic energy flux (*V*), and dissipation (*D*). All terms are defined following Menchaca and Durran (2019).

The nonlinear advective transfer term *T* is given by:

$$T(k) = -\bar{\rho}\left\{\left[\boldsymbol{u}, \boldsymbol{u}\cdot\nabla\mathbf{u} + \tfrac{1}{2}\boldsymbol{u}(\nabla\cdot\boldsymbol{u})\right]_k - \tfrac{1}{2}(\partial_z\boldsymbol{u}, w\boldsymbol{u})_k + \tfrac{1}{2}(\boldsymbol{u}, w\partial_z\boldsymbol{u})_k\right\} + \text{c.c.} \qquad (2.11)$$

where ρ is density, $\boldsymbol{u} = (u, v)$, and c.c. denotes the complex conjugate of the bracketed term. Terms of the form $(\boldsymbol{a}, \boldsymbol{b})_{\boldsymbol{k}}$ can be written as $\widehat{\boldsymbol{a}}^*(\boldsymbol{k})\cdot\widehat{\boldsymbol{b}}(\boldsymbol{k})$, where a hat denotes the forward Fourier transform and an asterisk denotes the complex conjugate (Peng et al. 2014a; Menchaca and Durran 2019). The overbar on density in (2.11) and subsequent equations denotes the average over the analysis domain.

The buoyancy forcing term *B* is given by:

$$B(k) = c_p\bar{\rho}\bar{\theta}(w, \partial_z\pi')_k + c.c. \qquad (2.12)$$

where c_p is the specific heat at constant pressure, θ is the potential temperature, w is the vertical velocity, and π' is the perturbation Exner pressure.

The divergence of the vertical kinetic energy flux *V* is given by:

$$V(k) = -\tfrac{1}{2}\partial_z[\bar{\rho}(\boldsymbol{u}, w\boldsymbol{u})_k] - c_p\partial_z[\bar{\rho}\bar{\theta}(w, \pi')_k] + c.c. \qquad (2.13)$$

Finally, the dissipation term *D* is calculated as a residual from (2.10). The full derivation of the terms on the right-hand side of (2.10) from the horizontal kinetic energy and the horizontal momentum equations can be found in Appendix C.

All terms are interpolated to height surfaces every 500 m between 5.5 km and 17 km above ground level. Horizontal derivatives are calculated on constant height surfaces and all partial derivatives are approximated utilizing a second-order–accurate centered finite difference. Fourier transforms are performed on one-dimensional zonal splices of data using the fast Fourier transform available in Python's SciPy package (Virtanen et al. 2020), then averaged meridionally

over the analysis domain. Given that the simulation (Fig. 2.2) and analysis (defined in section 2.5) domains are limited in area, a Tukey window is applied to the one-dimensional splices of data prior to performing the fast Fourier transform (Bloomfield 2000). This window tapered the data to zero on both ends, which will not remove all artificial noise produced by the decomposition, yet the tapering was selected to be gradual enough to minimize artificial noise produced by drastic gradients in the FFT operation.

To examine energy transfer across wavenumbers, each forcing term in (2.10) can be expressed in terms of its cumulative sum (Π_X) over all wavenumbers *k* (Menchaca and Durran 2019). For any variable $X(k)$,

$$\Pi_X(k) = \sum_{k \le l \le N} X(l) \tag{2.14}$$

where N is the maximum one-dimensional wavenumber. In this framework, wavenumbers at which Π_X has a negative slope (e.g., higher values at smaller wavenumbers) represent wavenumbers at which $X(k)$ increases kinetic energy. Conversely, wavenumbers at which Π_X has a positive slope (e.g., higher values at larger wavenumbers) represent wavenumbers at which $X(k)$ decreases kinetic energy. Since $T(k)$ describes conservative energy transfers between wavenumbers, the sign of Π_T indicates whether there is an upscale or downscale cascade of energy. Consequently, positive values of $\Pi_T(k)$ indicate downscale energy transfer to larger wavenumbers whereas negative values of $\Pi_T(k)$ indicate upscale energy transfer to smaller wavenumbers.

2.3 Model Verification

Given this study's emphasis on diagnosing the influence of convective-scale diabatically generated PV anomalies on the midlatitude waveguide, the verification presented herein focuses on diagnosing the extent to which the model simulation accurately predicted rainfall within the

PRE and, subsequently, the tracks and intensities of TCs Irma and Jose. TC tracks are primarily dictated by tropospheric-deep mean flow (Velden and Leslie 1991), therefore accurate track (and subsequent intensity) forecasts for the two TCs are indicative of the simulation accurately capturing the large-scale flow pattern in the vicinity of the TCs.

The interaction between the upstream trough, Irma, and the PRE, appears to be well captured in the simulation, with the placement and strength of the midlatitude jet being well captured 36-h into the simulation (Fig. 2.1). Positioning of the precipitation inside of the PRE was also well captured by the simulation, with a distinct maximum of precipitation oriented from east to west along the 31st parallel (Fig. 2.4). While precipitation totals were generally well represented in the simulation, the heavier precipitation covered a smaller spatial area than observed (Fig. 2.4), although this may be at least be partially due to resolution differences between the two datasets. Given that our study is interested in the amount of diabatic heating occurring in the PRE, the amount of precipitation which fell (vs. positioning the precipitation) is of primary concern, which appears to have been well captured by the simulation (Fig. 2.4).

The simulation accurately predicts TC Irma's track and intensity (Fig. 2.5ab). The TC Irma lifetime average track error is 92 km (compared to the climatological 72-h track forecast error of 191 km; Cangialosi 2018), with a slight east bias following landfall (Fig. 2.5a), and the TC Irma lifetime average intensity error is 6 kt (3.1 ms^{-1}; compared to the climatological 72-h intensity forecast error of 12.6 kt [6.5 ms^{-1}]; Cangialosi 2018), with the simulated minimum sea-level pressure and 10-m wind speeds closely resembling their National Hurricane Center best-track values (Fig. 2.5b). Simulated track and intensity errors for TC Jose are slightly larger (Fig. 2.5cd). Both the simulated and observed TCs complete an anticyclonic loop; however, the simulated TCs loop is somewhat more circular and extends further to the west (Fig. 2.5c).

Despite these differences, however, the TC Jose lifetime average track error is only 83 km (compared to the climatological 120-h track forecast error of 364 km; Cangialosi 2018), with a lifetime-maximum error of 168 km at 0600 UTC 16 September 2017. Jose's intensity forecast errors were occasionally quite large, with a peak intensity error of nearly 60 kt (31 ms^{-1}; compared to the climatological 120-h intensity forecast error of 14.3 kt [7.4 ms^{-1}]; Cangialosi 2018) near the end of the simulation (Fig. 2.5d). These large errors are potentially driven by the small size of Jose, with the simulation being unable to depict the sharp horizontal gradients of pressure and wind near the TCs center. The simulated intensity traces still approximately follow the same trends as what was observed until the last 36 h of the simulation.

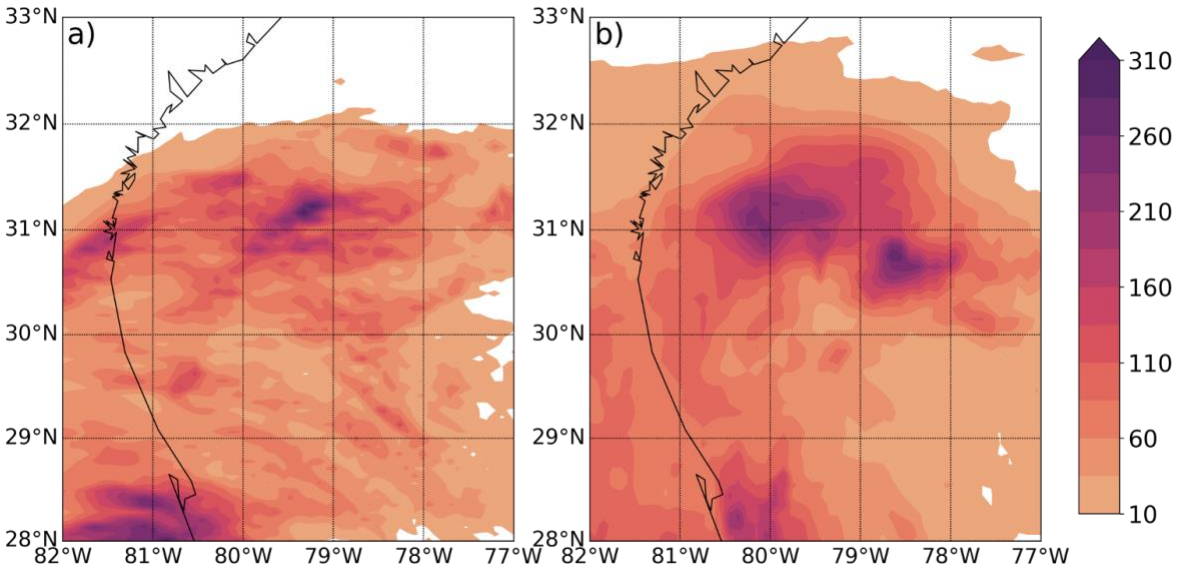

Figure 2.4. 24-h accumulated precipitation (shaded in mm per the color bar at right) between 0000-2359 UTC 10 September 2017 from the (a) WRF-ARW simulation coarsened to 0.1˚ X 0.1˚ horizontal grid spacing and (b) 0.1˚ X 0.1˚ NASA IMERG version 06 dataset.

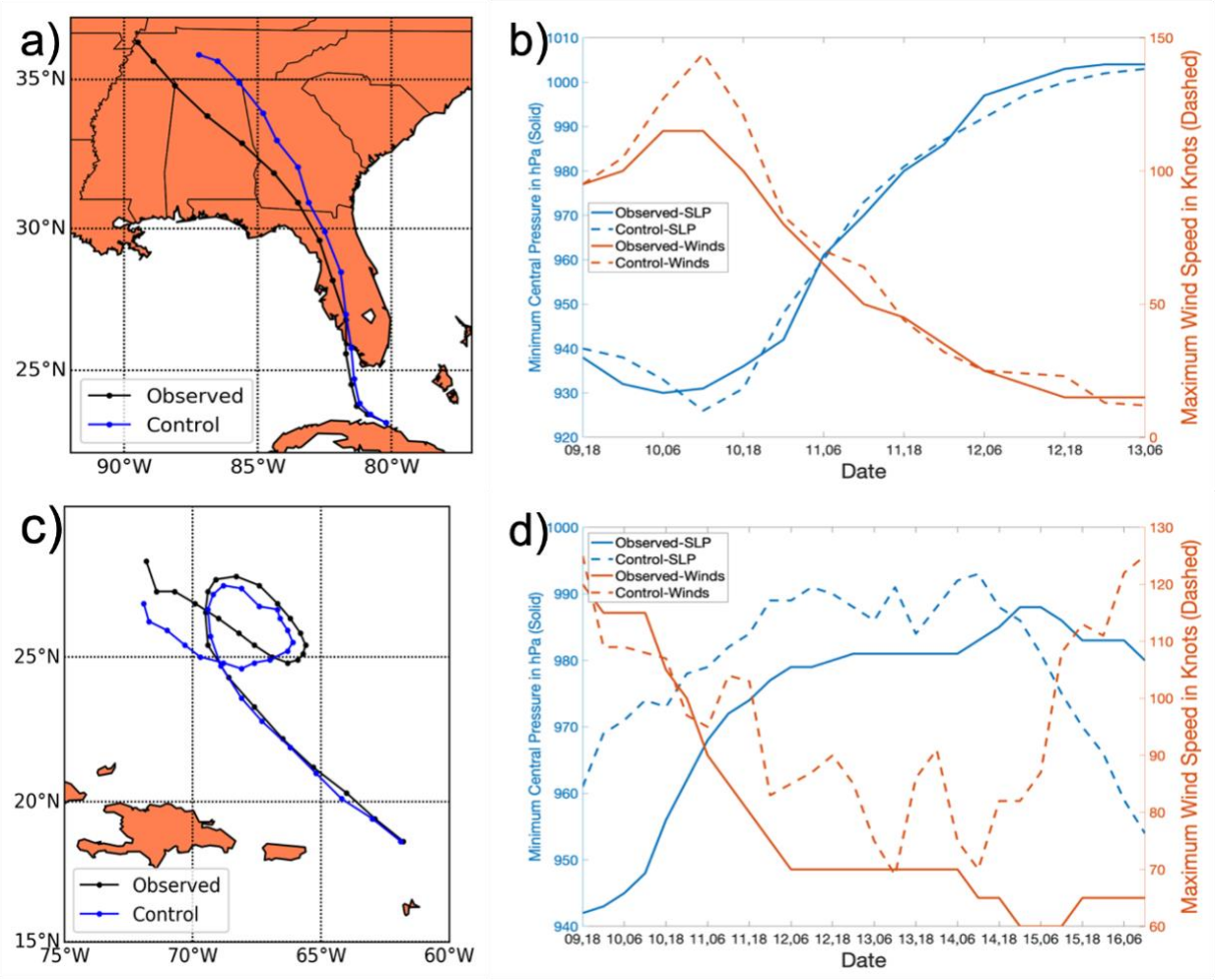

Figure 2.5. (a, c) Simulated (blue lines) and National Hurricane Center best-track (black lines) tracks for (a) TC Irma (between 1800 UTC 9 September and 0600 UTC 13 September 2017, at which time TC Irma was declared post-tropical) and (c) TC Jose (over the simulation's entirety). (b, d) Simulated (dashed lines) and National Hurricane Center best-track (solid lines) minimum sea-level pressure (hPa; blue lines) and maximum sustained 10-m wind speed (kt; orange lines) for (b) TC Irma (between 1800 UTC 9 September and 0600 UTC 13 September 2017, at which time TC Irma was declared post-tropical) and (d) TC Jose (over the simulation's entirety).

2.4 Convective-Scale PV Anomalies Production and Maintenance

The PRE poleward of TC Irma is associated with two major convective bursts, one between 1300 UTC 9 September and 0000 UTC 10 September 2017 (Fig. 2.6) and another between 0400-1300 UTC 10 September 2017 (not shown), within a broader region of predominantly stratiform precipitation. These convective bursts are associated with widespread intense PV dipoles along a baroclinic zone (as inferred from the large vertical wind shear; Fig. 2.6a) extending from southwest to northeast along the southeastern United States coastline. Negative PV anomalies are located poleward of the corresponding positive anomalies, which is consistent with the deep-layer vertical wind shear's direction (Fig. 2.6). Near initiation, while the positive and negative anomalies remain together, the net circulation across the two is roughly equal to zero (not shown), indicating a minimal impact to the surrounding flow. Several hours later, the positive anomalies have largely weakened and/or remained near their initiation locations (Fig. 2.6b), whereas the negative PV anomalies become elongated and begin to merge into a narrow but long filament (Fig. 2.6b). By 6 h after initiation (Fig. 2.6c), the negative PV anomalies continue to persist and have propagated north of their original location immediately offshore from the southeastern United States coastline. Altogether, the inertially unstable negative PV anomalies persist for multiple hours after their initiation. After the negative anomalies separate from their positive counterparts, the net circulation over the remaining negative anomaly is nonzero, thus its impact to the surrounding flow would also be nonzero.

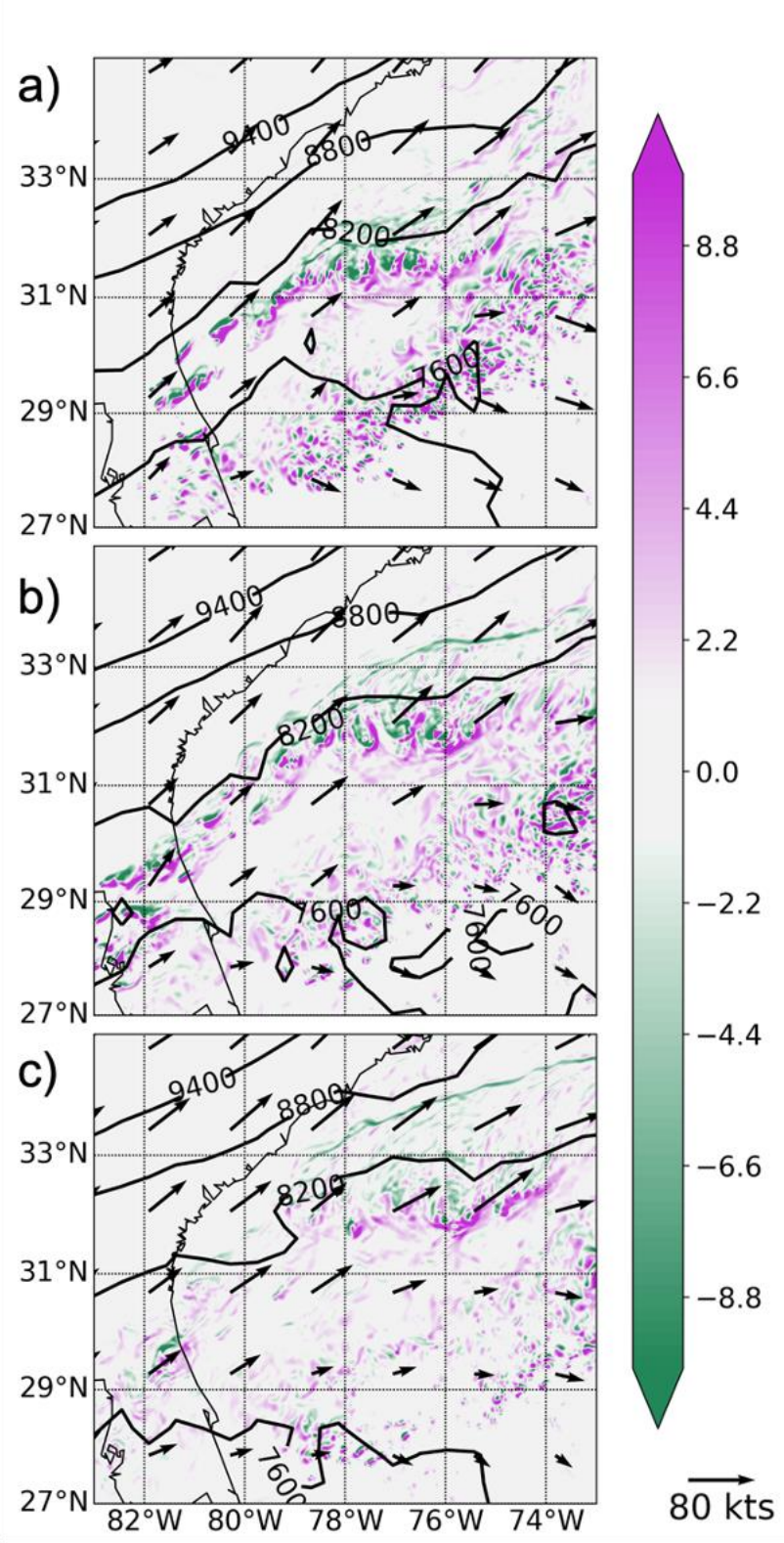

Figure 2.6. 335-K geopotential height (black contours every 600 m), 335-K PV (shaded in PVU per the color bar at the right), and 350-to-320–K vertical wind shear (vectors; kt; reference vector at lower right) at (a) 1600 UTC, (b) 1900 UTC, and (c) 2200 UTC 9 September 2017.

The isentropic PV tendency equation (2.3) is used to diagnose the physical processes by which the PV anomalies initiate, doing so in the context of a representative isolated thunderstorm embedded within the PRE (Fig. 2.7). Near initiation, horizonal gradients of microphysical heating dominate the right-hand side of (2.3), generating a PV dipole on the order of $\pm$10 PVU in a matter of minutes (Fig. 2.7b). As this dipole initiates, the background wind field advects the newly generated anomalies, contributing to a non-zero advective tendency (Fig. 2.7a). These structures extend across an isentropic depth of nearly 30 K (Fig. 2.8ab), corresponding to a layer depth of approximately 5000 m (from approximately 5000-10000 m; not shown). The isolated updraft quickly weakens and tilts downshear, although the PV dipoles persist (Figs. 2.7cd, 2.8cd). Since microphysical heating is directly tied to ascent, the contributions from the nonconservative tendencies quickly dissipate, leaving the advective tendency as the sole non-negligible contributor to the total PV tendency (Figs. 2.7cd, 2.8cd). This process continues forward in time (Figs. 2.7ef, 2.8ef), with near-zero nonconservative tendencies and non-zero advective tendencies persisting in time. Since the nonconservative tendencies are approximately zero shortly after the PV dipoles' initiation, it is not surprising that the PV anomalies persist for multiple hours (Fig. 2.6). Over time, the intense localized negative and positive PV anomalies slowly weaken due to implicit numerical dampening associated with the WRF-ARW model's fifth-order–accurate horizontal and third-order–accurate vertical advection parameterizations (Skamarock et al. 2019; not shown).

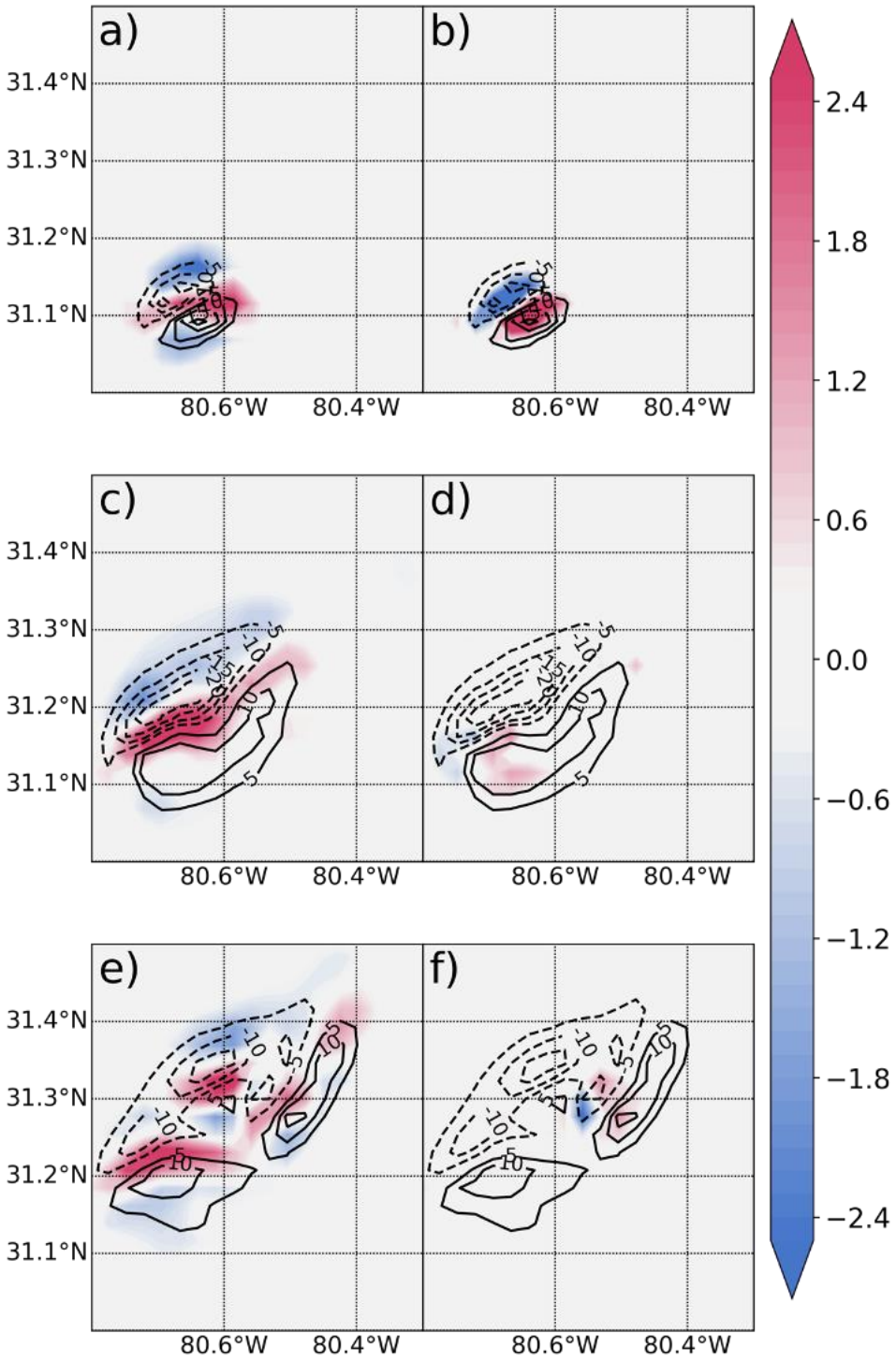

Figure 2.7. (a, c, e) Three-dimensional advective PV tendency (term 1 on the right side of (2.3), shaded in PVU min^{-1} per the color bar at right) and PV (black contours at -20, -15, -10, -5, -2, 2, 5, 10, 15, and 20 PVU) on the 335-K isentropic surface at (a) 1433 UTC, (c) 1457 UTC, and (e) 1521 UTC 9 September 2017. (b, d, f) As in (a, c, e), except for the total nonconservative tendency (terms 2 and 3 on the right side of (2.3)).

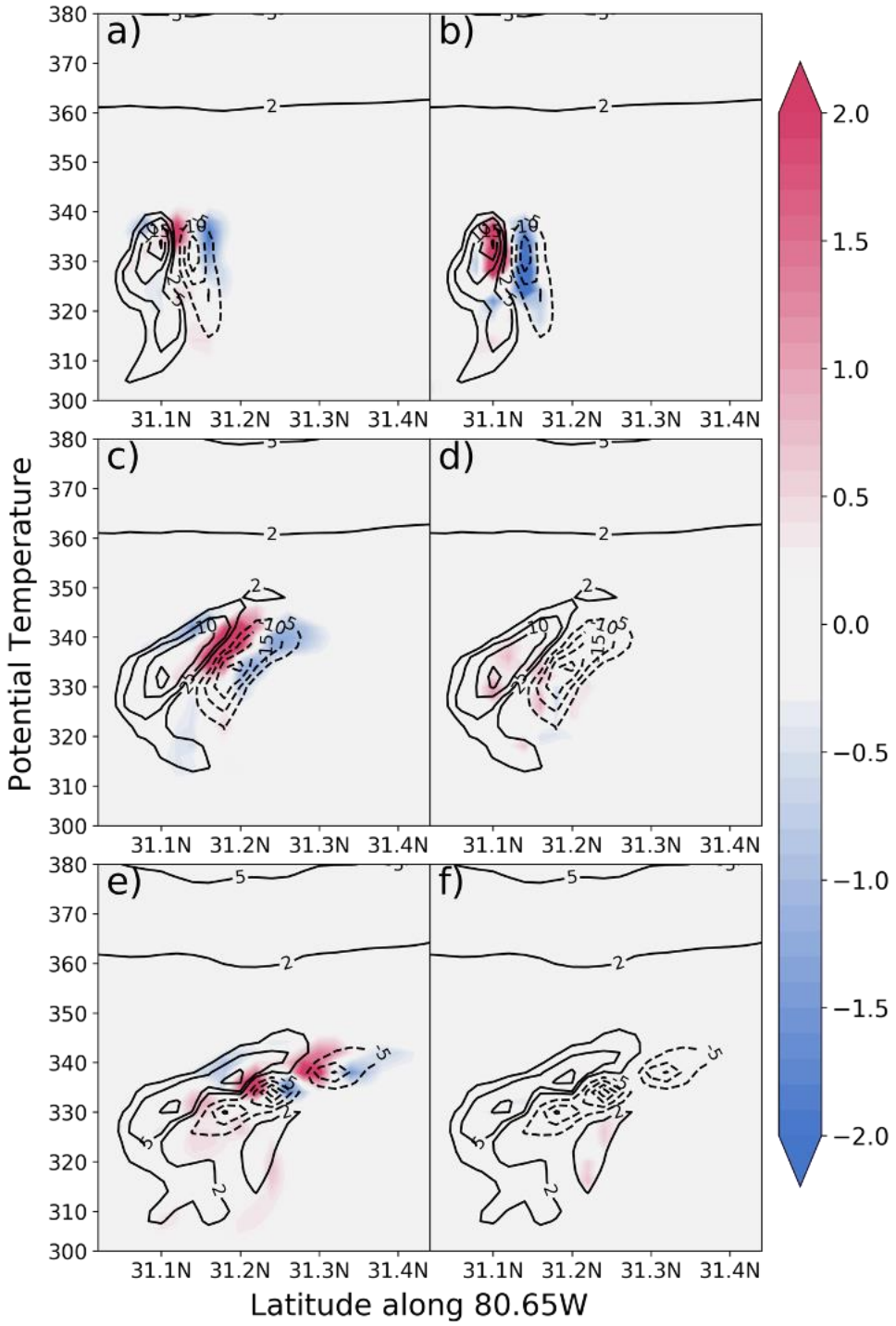

Figure 2.8. (a, c, e) Vertical cross-section (between 300-380 K along 80.65°W, averaged between 31-31.5°N) of the three-dimensional advective PV tendency (term 1 on the right side of (2.3), shaded in PVU min^{-1} per the color bar at right) and PV (black contours at -20, -15, -10, -5, -2, 2, 5, 10, 15, and 20 PVU) on the 335 K isentropic surface at (a) 1433 UTC, (c) 1457 UTC, and (e) 1521 UTC 9 September 2017. (b, d, f) As in (a, c, e), except for the total nonconservative tendency (terms 2 and 3 on the right side of (2.3)).

2.5 Local Energy Flux and the Inverse Energy Cascade

The local energy flux and spectral kinetic energy budget diagnostics introduced in sections 2.2.4 are each functions of the kinematic field, whereas the PV anomalies detailed in section 2.4 include both thermodynamic and kinematic structures. As might be expected, however, there is a strong correspondence between PV and kinetic energy anomalies (Fig. 2.9). PV anomalies directly correspond to absolute-vorticity anomalies (contours in Fig. 2.9), with a substantial reduction in kinetic energy between the PV/absolute vorticity anomalies (shading in Fig. 2.9). Between the PV anomalies, the PV anomalies' induced circulations act against the southwesterly background flow, weakening the horizontal wind and thus kinetic energy between them (Fig. 2.9; Oertel and Schemm 2021). Conversely, poleward of the negative PV anomaly and equatorward of the positive PV anomaly, the horizontal wind and kinetic energy are strengthened by enhancement of the background flow by the circulations' induced flows (Fig. 2.9c).

Before the convective cells initiate in the PRE and produce regions of convective scale PV/absolute vorticity, nearly all (~90-95%) of the spectral power of the absolute vorticity in the vicinity of the PRE is concentrated at the two largest wavelengths (1200 km and 600 km; Fig. 2.10). By 0900 UTC 9 September 2017 (9 hours into the simulation), the model has sufficiently spun-up, which is highlighted by stable behavior from the 90^{th} percentile line (Fig. 2.10). The percentage of spectral power concentrated at longer wavelengths decreases during the PRE's two convective bursts (from approximately 1300 UTC 9 September to 0000 UTC 10 September 2017 and 0400 UTC to 1300 UTC 10 Sep 2017; Fig. 2.10). The primary increase in power for both convective bursts occur in the range of wavelengths from 300 km to 60 km, which is larger than a single convective cell, yet match the approximate size of the clusters of convection identified

earlier (Figs. 2.6 and 2.10). A reduction of nearly 25% in the total spectral power contribution at the lowest wavenumbers suggests a significant amount of energy which is supplied to mesoscale wavelengths before being transferred upscale and going on to have a non-zero impact to the large-scale flow (Fig. 2.10).

While the spectral power suggests an increase in energy at meso-α to subsynoptic scales, it cannot demonstrate whether that energy is being transferred to the large scales, or not. To address this, the local energy flux is calculated in the vicinity of the PRE (Fig. 2.11). In the sense of the local energy flux, the localized PV, absolute-vorticity, and kinetic-energy anomalies contribute to the u'_ℓ upon which the large-scale strain $\bar{u}_\ell$ would act. Model-resolved thunderstorms are associated with positive and negative local energy fluxes (suggestive of forward and inverse energy cascades, respectively) on the meso-gamma-scale (Fig. 2.11a). At convective-scale wavelengths, the small-scale positive and negative regions of the local energy flux largely cancel, causing the mean local energy flux to be closer to zero, albeit with a large amount of temporal variability (Fig. 2.11e). The local energy flux becomes increasingly negative at larger length scales, suggestive of a broad region of energy cascading from smaller to larger scales (Fig. 2.11b-d). Area averaging of the local energy flux reveals that at larger wavelengths the temporally and area averaged local energy flux is increasingly negative, demonstrating an inverse cascade of energy up to 1500 km in the vicinity of the PRE (Fig. 2.11e).

To test the existence of the 'thinning' mechanism mentioned earlier, the temporally averaged large-scale strain field in the vicinity of the PRE is calculated (Fig. 2.12). The environment between TC Irma and the upstream midlatitude trough is characterized by synoptic-scale deformation, with the axis of dilatation (red line in Fig. 2.12) extending from the southeastern Gulf of Mexico northeastward across Florida and along the Gulf Stream offshore of

the southeast United States coastline. Thunderstorms embedded within the PRE roughly align with this axis of dilatation, the flow associated with which performs negative work on the turbulent anomalies as it filaments them along the deformation flow (Fig. 2.12).

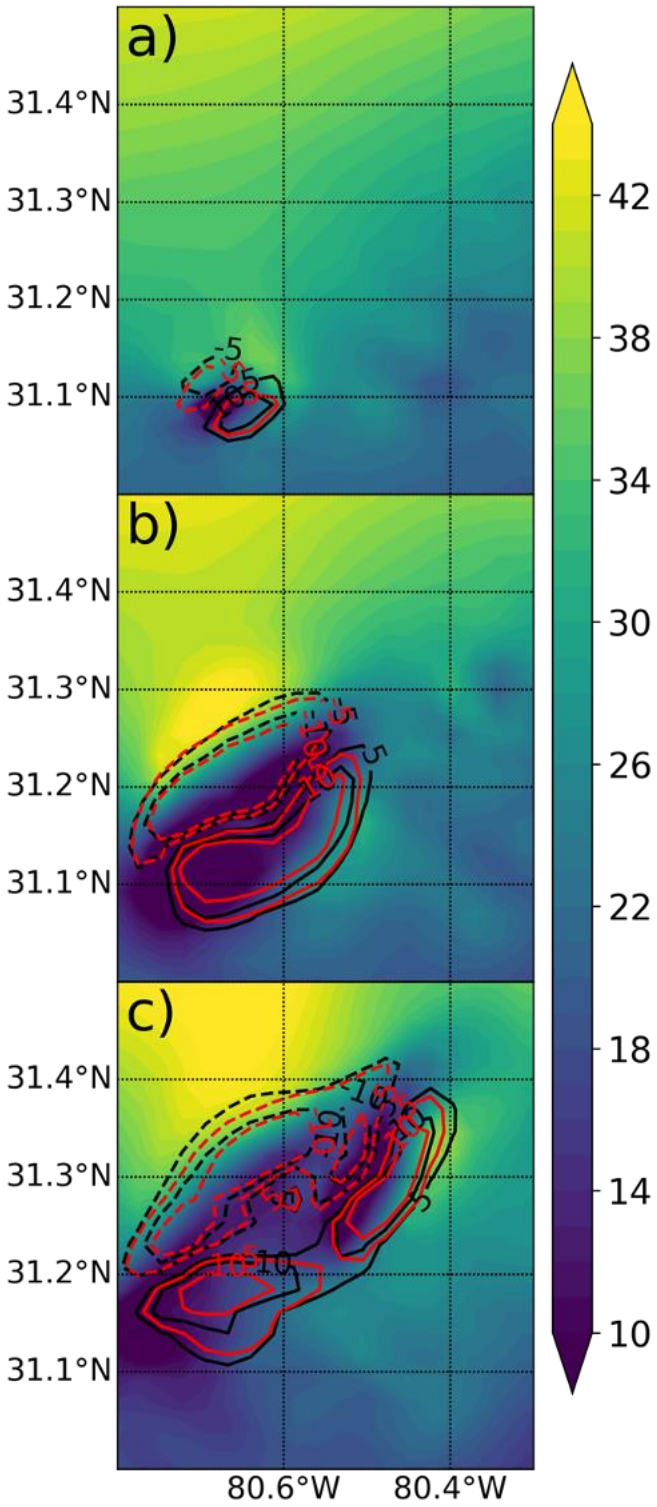

Figure 2.9. Horizontal kinetic energy (shaded in 10 x 10^6 J per the color bar at right), absolute vorticity (black contours at -10, -5, 5, and 10 x 10^{-4} s^{-1}), and PV (red contours at -10, -5, 5, and 10 PVU) on the 335 K isentropic surface at (a) 1433 UTC, (c) 1457 UTC, and (e) 1521 UTC 9 September 2017.

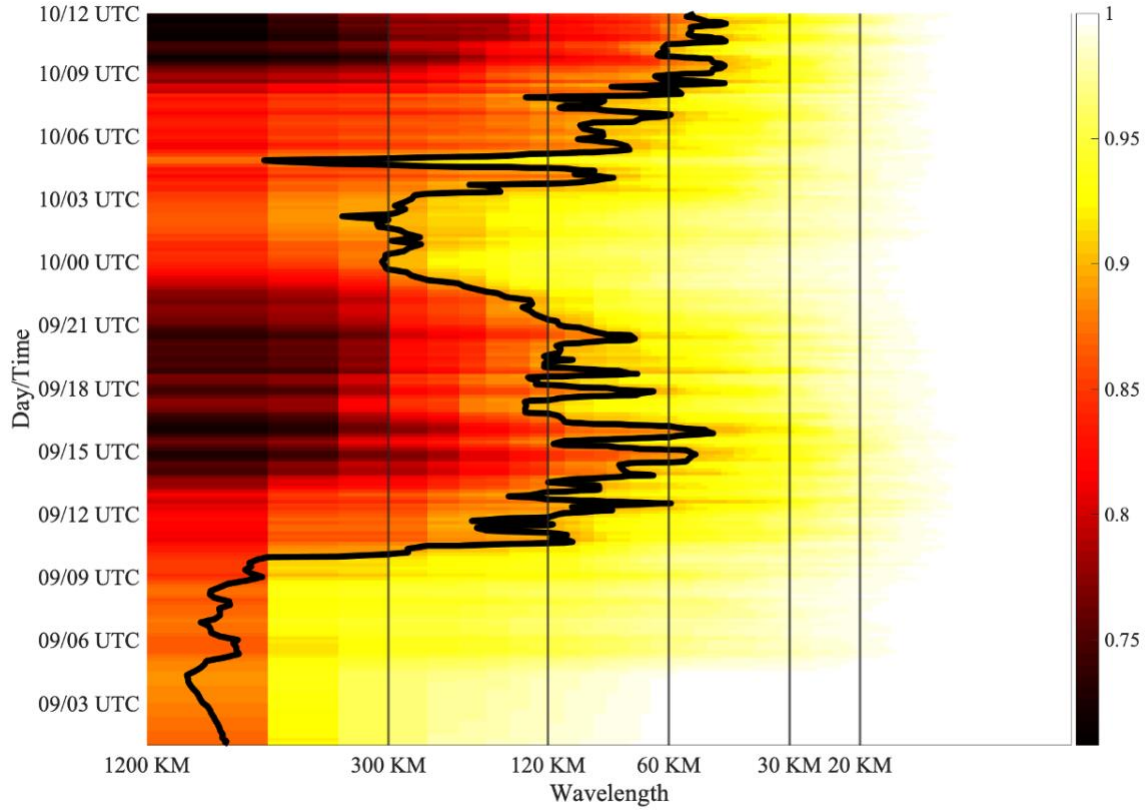

Figure 2.10. Cumulative normalized spectral power of area-averaged (between 28°-37°N, 89°-75°W matching the box in figure 2.1b) absolute vorticity on the 335-K isentropic surface (unitless; shaded per color bar at right). The bold black line denotes the 0.9 (90%) cumulative normalized spectral power contour; i.e., the wavelength above which 90% of the cumulative normalized spectral power is contained.

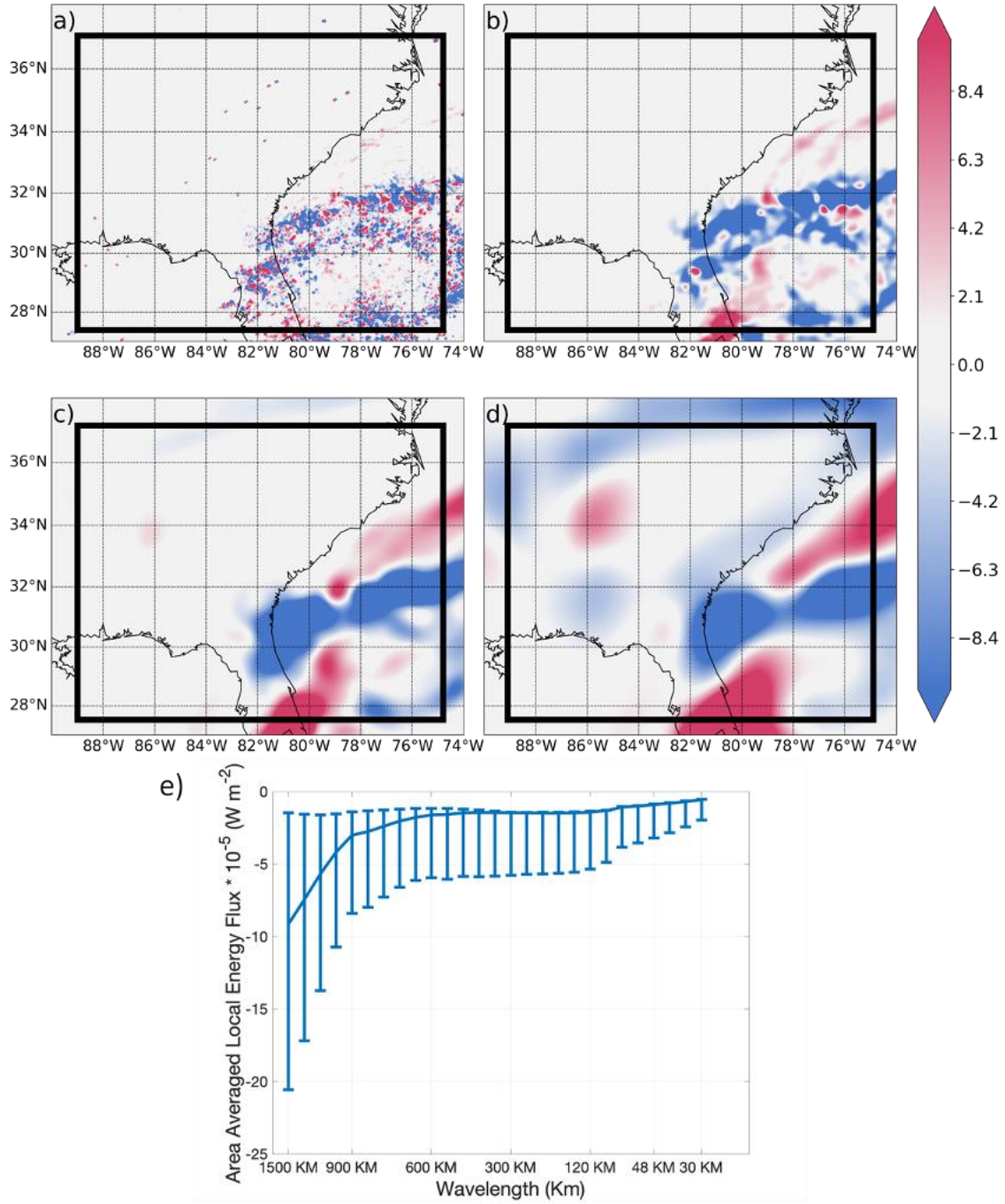

Figure 2.11. (a-d) Temporally averaged (between 1800 UTC 9 September and 1200 UTC 10 September 2017) local energy flux (10^{-5} Watts m^{-2}; shaded per the color bar at right) on the 335 K isentropic surface for a length scale ℓ of (a) 30 km, (b) 120 km, (c) 300 km, and (d) 600 km. (e) Area- (between 28°-37°N and 89°-75°W, as denoted by the black box which matches the box in figure 2.1b) and temporally (between 1800 UTC 9 September and 1200 UTC 10 September 2017) averaged local energy flux as a function of length scales between 30-1500 km. Error bars in (e) represent the 95th percentile spread of the area-averaged local energy flux over time.

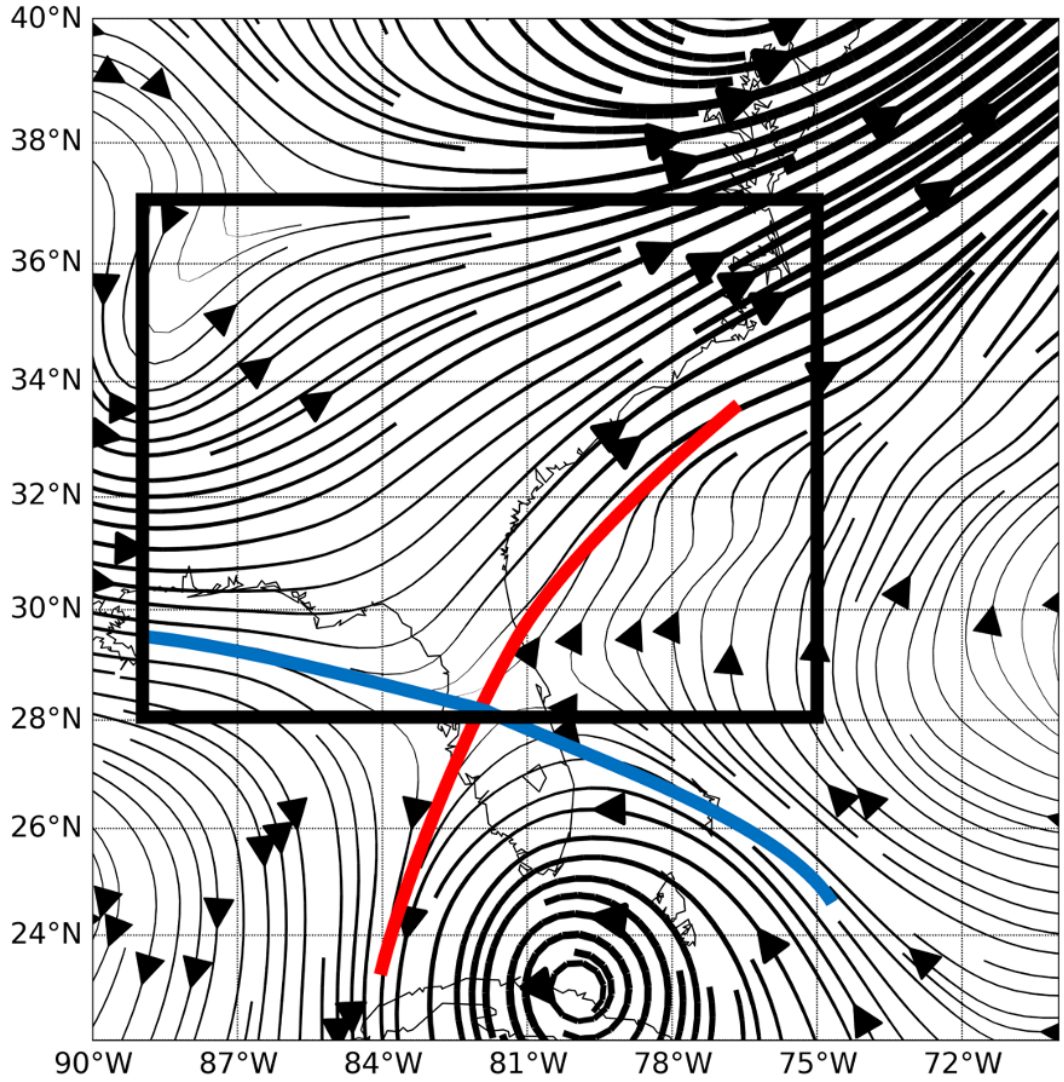

Figure 2.12. Streamlines of the temporally averaged (between 1800 UTC 9 September and 1200 UTC 10 September 2017) large-scale flow $\bar{u}_\ell$, where ℓ = 300 km, on the 335-K isentropic surface. The blue line denotes the approximate axis of contraction, and the red line denotes the approximate axis of dilatation, while the black box denotes the region over which area-averaging in previous and subsequent analyses are performed which matches the box in figure 2.1b.

The above analyses demonstrate the impacts convective cells have on the local PV and kinetic energy fields and suggest the existence of an inverse cascade of energy in the vicinity of the PRE. However, they cannot quantify the magnitude of the energy being transferred to large scales or explain the physical processes which transfer this kinetic energy to the upper troposphere. To address these limitations, the kinetic energy framework adopted in Menchaca and Durran (2019) is employed. It is found that thunderstorm updrafts inside of the PRE transport (by way of the vertical advective flux) kinetic energy from the lower to the upper troposphere (Fig. 2.13ab), whereupon the kinetic energy is transferred upscale by way of an inverse energy cascade (Fig. 2.13b). This result is insensitive to the precise bounds of the PRE region depicted in Fig. 2.1b (not shown).

The midtropospheric (5.5-9 km AGL; encompassing the lower portion of the PV anomalies induced by convection [Fig. 2.8]) kinetic energy budget in the vicinity of the PRE (black box in Fig. 2.1b) is characterized by spectral transports and buoyancy forcing that increase kinetic energy and by vertical fluxes and dissipation that decrease kinetic energy (Fig. 2.13a). Specifically, there is a cascade of energy from large to small scales over all wavelengths ($\Pi_T > 0$; Fig. 2.13a). The buoyancy force also acts to increase KE from 5.5 km-9 km over all wavelengths ($^{\partial \Pi_B}/_{\partial k} < 0$), which is likely driven by energy supplied by convective updrafts (Fig. 2.13a). The vertical advective flux, however, extracts energy away from the 5.5 km-9 km layer at wavelengths of approximately 75 km and larger ($^{\partial \Pi_V}/_{\partial k} > 0$; Fig. 2.13a), possibly as convective updrafts extract energy from lower levels. Additionally, the dissipative term acts to decrease KE at nearly all wavelengths and all vertical layers (Fig. 2.13a-c).

In the mid- to upper troposphere (9.5-13 km), both the vertical advective and buoyancy fluxes are acting to add KE at nearly all wavelengths ($^{\partial \Pi_V}/_{\partial k} < 0$ and $^{\partial \Pi_B}/_{\partial k} < 0$), suggesting a depositing of energy by convective updrafts at higher levels (Fig. 2.13b). After being injected into the upper troposphere by convective updraft, the energy concentrated at wavelengths of less than approximately 200 km is cascaded from large to small scales ($\Pi_T > 0$), but for energy at wavelengths greater than or equal to 200 km, there is an inverse cascade to larger wavelengths ($\Pi_T < 0$; Fig. 2.13b). In the lower stratosphere (13.5-17 km), the vertical advective flux increases KE at all wavelengths (Fig. 2.13c). Additionally, the buoyancy term has weakened significantly at mesoscale wavelengths, likely due to the rarity of convective updrafts

travelling to heights of > 15 km (Fig. 2.13c). The inverse cascade of energy is no longer present and has reversed back to a cascade of energy from large to small scales over all wavelengths (Fig. 2.13c).

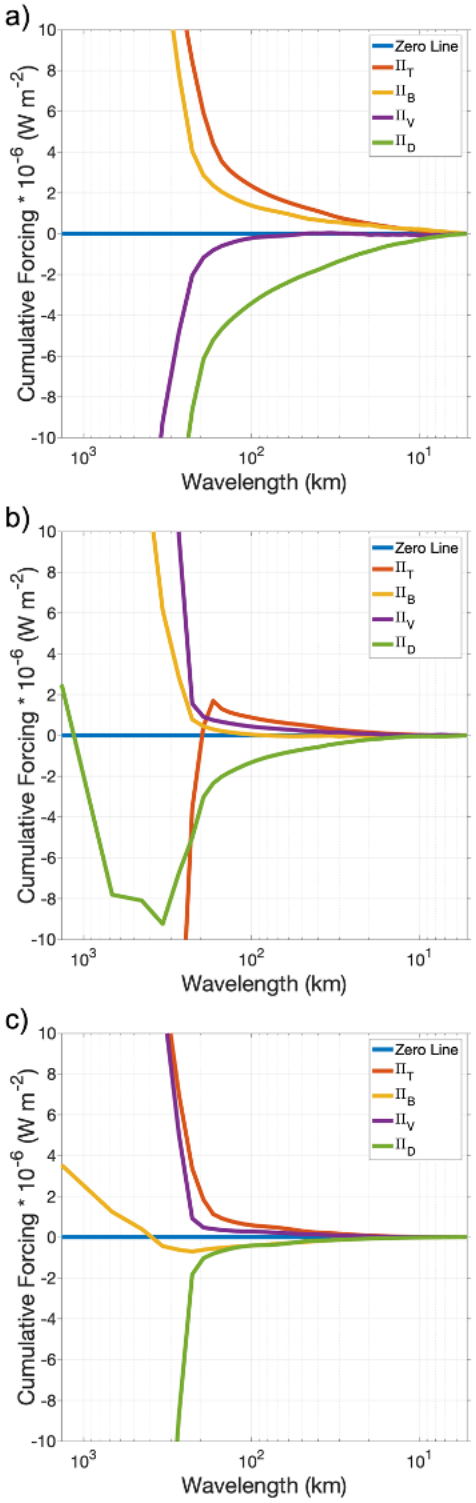

Figure 2.13. (a-c) Cumulative transport (orange line), buoyancy (yellow line), divergence of the vertical kinetic energy flux (purple line), and dissipation (green line) forcing terms in the spectral kinetic energy budget, as calculated over the black box depicted in Figure 2.1b and averaged between (a) 5.5-9 km, (b) 9.5-13 km, and (c) 13.5-17 km above ground level temporally averaged from 1800 UTC 9 Sep to 1200 UTC 10 Sep 2017.

2.6 Conclusions

Interactions between TCs- and midlatitude troughs are typically conceptualized as being driven by the large-scale, diabatically driven vertical redistribution of PV, with the smaller-scale, diabatically driven horizontal redistribution of PV typically neglected. However, a separate vein of research has demonstrated the existence of intense convective-scale PV dipoles generated by strong latent heating in deep moist convection. Given that diabatic processes are a potential source of forecast error in TC-trough interactions (Anwender et al. 2008), this study tests the hypothesis that deep, moist convection associated with a PRE modified the synoptic-scale midlatitude waveguide in a recent TC-midlatitude waveguide interaction by way of the production of convective-scale intensely negative PV against the waveguide by deep, moist convection. A convection-allowing simulation of the PRE in advance of North Atlantic TC Irma (2017)'s interaction with the midlatitude waveguide is performed to test this hypothesis.

The physical processes that allow for thunderstorm-scale PV anomalies to modify the synoptic-scale flow can be conceptualized as follows (Fig. 2.14). When a thunderstorm initiates within a vertically sheared flow, its associated horizontal gradients of diabatic heating generate PV anomalies aligned perpendicular to the background vertical wind shear vector, with negative PV anomalies to the left of the shear vector and positive PV anomalies to the right of the shear vector (Figs. 2.6 and 2.7ab). On the eastern flank of the upstream trough and to the north of Irma, the large-scale strain field can be approximated as having an axis of dilatation oriented from southwest to northeast (Fig. 2.12). This large-scale strain deforms the convectively generated PV anomalies, stretching them along the axis of dilatation (Figs. 2.6ac). The newly deformed PV anomaly covers a larger area than it did before, such that from the circulation theorem its rotation rate must decrease. Due to the alignment of the deformed anomaly with the large-scale strain

field, a tensile stress is applied to the large-scale strain, thus reinforcing the large-scale strain, and adding energy to the large-scale flow (Fig. 2.14). The inverse energy cascade is accomplished by the filamentation of the negative PV anomalies (Fig. 2.14).

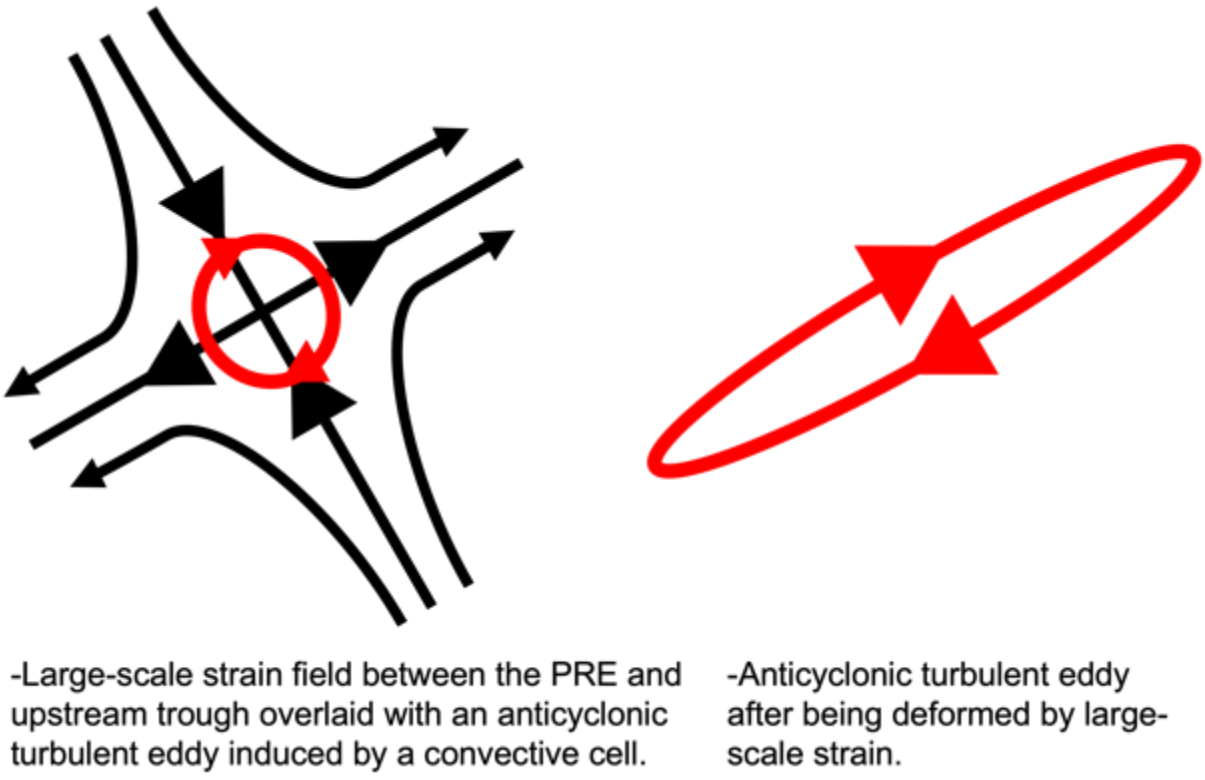

Figure 2.14. Conceptual model demonstrating the impact of large-scale strain (black) on small-scale anticyclonically rotating turbulent eddies (red) such as those convectively generated within a PRE. The cyclonic eddy was neglected as only the anticyclonic eddies propagate northward against the waveguide in our simulation.

This study's results largely support Oertel et al. (2020, 2021) and Oertel and Schemm (2021), each of which demonstrate that convectively generated PV anomalies align perpendicular to the background vertical wind shear vector, the negative PV anomalies separate from their positive PV anomaly counterparts, and the negative PV anomalies subsequently modify the surrounding flow. The present study builds on these results by identifying an inverse energy cascade in the PRE's vicinity and outlines a physical mechanism by which this cascade is accomplished following methodology presented in Menchaca and Durran (2019).

While this study identifies a pathway by which convective-scale processes inside of a PRE may modify the large-scale midlatitude pattern, the extent to which the results are generalizable is unclear. This study considers a single numerical simulation of a single case at a single initialization time, and further investigation over a larger sample of cases is warranted to assess the extent to which these findings are representative of all PREs and not just the PRE studied herein. Furthermore, our simulation does not inhibit larger-scale processes from occurring such that it cannot conclusively be said that the PRE's modification of the waveguide is entirely driven by smaller-scale processes and an upscale energy cascade. Therefore, it cannot yet be said how much of the waveguide modification is driven by smaller scales vs. how much is driven by larger scales. This study can only demonstrate that the smaller scales can have a larger-scale impacts in this study.

Future studies will test this sensitivity by performing sensitivity analyses in which impacts from convection will be limited/removed by way of piecewise PV inversion (e.g., Grams et al. 2013ab), or by modifying the diabatic warming in the PRE's vicinity (e.g., turning off diabatic warming in a local area, removing large- and/or small-scale contributions to the diabatic warming, etc.). While this study was only applied to a PRE well to the north of Irma, it could be

argued that clusters of embedded convection in the outer rainbands of a TC could be viewed in the same fashion. Due to the nature of a TCs rotational wind field, the vertical wind shear vector around the TC would be oriented such that negative PV would always be on the outer radius. One could then view the TC as a feature which “radiates” negative PV anomalies, driven by the TCs secondary circulation.

Chapter 3

Relative Contributions of Microphysical Heating Within a Predecessor Rain Event and Tropical Cyclone in a Tropical Cyclone-Midlatitude Waveguide Interaction

3.1 Introduction

Section 2 identifies a physical pathway by which convective-scale processes may have an influence on the large-scale flow. These impacts are manifest by the filamentation of intense PV dipoles produced by horizontal gradients of diabatic warming in deep, moist convection. In section 2, the filamentation mechanism supporting the inverse cascade of energy from the small to the large-scales was identified through an examination of North Atlantic TC Irma (2017) wherein deep, moist convection inside of a PRE to the north of North Atlantic TC Irma in September 2017 influenced the behavior of an upstream midlatitude trough by the generation of intensely negative PV against the eastern flank of the trough, promoting an optimal interaction between Irma and the midlatitude waveguide. In this final part of the study, we attempt to quantify the impacts of microphysical heating inside of the PRE and Irma on the evolution of the indirect interaction between North Atlantic TCs Irma and Jose (2017) discussed in sections 1 and 2.

The purpose of the third part of this study is to test the hypothesis that deep moist convection inside of a PRE in a TC-midlatitude waveguide interaction impacts the evolution and predictability of the strength of the interaction and subsequent downstream evolution by way of the production of negative PV against the equatorward flank of the midlatitude waveguide. This

hypothesis is tested by performing a series of sensitivity simulations in which microphysical heating is systematically turned off in the vicinity of the PRE, Irma, or both, and over varying times.

3.2 Methods

3.2.1 Model Setup

The case of interest in this study is the indirect interaction between North Atlantic TCs Irma and Jose in September of 2017. A description of the synoptic setup of this case be found in section 2.2.1. Additionally, the Control simulation here is the simulation explored in section 2, of which the model setup description can be found in section 2.2.2, with the model parameters described in Table (2.1) and the simulation domain shown in Figure (2.2). The modifications which were done to the WRF code to systematically turn off diabatic warming in the simulation are outlined in Appendix D.

3.2.2 Sensitivity Simulations

Five sensitivity simulations are performed (Table 3.1) in which diabatic heating is turned off over a portion of the simulation domain to exclude any contributions by the microphysical parameterization. The first region is labelled as “PRE” and attempts to turn off microphysical heating for convection in the PRE, while largely leaving the core and outer rainbands of TC Irma unaffected (Fig. 2.6). The second domain is labelled as “Irma” and aims to primarily turn off microphysical heating in TC Irma’s core, while also attempting to turn off microphysical heating in Irma’s rainbands without impacting convection in the PRE (Fig. 2.6). Finally, the “PRE&Irma” domain covers an expansive region, which aims to turn off microphysical heating in both TC Irma and the PRE (Fig. 2.6). The PRE domain needed to cover an extensive enough area to ensure as much convective activity along the baroclinic zone was suppressed (Fig. 2.6)

while leaving the core of Irma unaffected. This led to a southern boundary of approximately 26˚N for the PRE domain (Fig. 3.1), with a minimum distance between Irma's core and the boundary of approximately 175 km at 1200 UTC 10 September (not shown). The Irma domain was originally tested with western and eastern extents of 86˚W and 77˚W, respectively, however, due to Irma's circulation being so expansive, radial convective bands were still initiated outside of the region's extent. This led to an expansion of the boundaries to 90.5˚W and 74.3˚W (Fig. 3.1). Utilizing the western and northern boundaries from the Irma and PRE domains respectively, and the southern and eastern extent of the Irma domain, the PRE&Irma domain covers an expansive region with the goal of limiting all impacts from both features (Fig. 3.1). The PRE&Irma domain also encompasses a region that neither the PRE nor the Irma domains cover, yet this is not believed to be an issue, as intense convective-scale processes are not present in this additional region (not shown).

There are two potential shortcomings of the domains selected worth noting. The first being the cutoff between the Irma and PRE domains of 26˚N. While the PRE and Irma start as distinct features, Irma's outer rainbands start to become indistinguishable from the PRE near 1200 UTC 10 September 2017 (Fig. 3.2). Given this, the selection of a different parallel may be equally as reasonable as 26˚N, which may lead to different solutions. The second is that the PRE&Irma domain encompasses at least part of the upstream trough (Figs. 2.1 and 3.1). While limiting diabatic heating in the vicinity of the upstream trough is bound to lead to some differences, in all but one simulation (PRE&IrmaWS), the time over which diabatic heating is turned off in the vicinity of the trough (< 36 h), is likely much shorter than the time it would take for the troughs circulation to spin down significantly.

Around 1200 UTC 10 September 2017, as Irma's outer rainbands start to become indistinguishable from convection in the PRE (Fig. 3.2), diabatic heating is turned back on from this time onward to prevent any unintended impacts to Irma's core circulation (Table 3.1). For consistency, this time is also utilized for the PRE&Irma and Irma simulations as well (Table 3.1). This leaves two simulations, the first of which is the PRE18 simulation, which extended the timing over which diabatic heating is turned off in the PRE until 1800 UTC 10 September 2017 to test the temporal sensitivity of denying the production of convective-scale PV in the PRE (Table 3.1). The other outlier is the PRE&IrmaWS simulation, in which diabatic heating is continuously neglected for the entirety of the 180-h simulation (Table 3.1). This is meant to be the most extreme case, which not only removes any impacts from Irma and the PRE, but also neglects microphysical warming in the midlatitude trough as well (Fig. 3.1).

Simulation Name	Description
PRE	Contributions to the potential temperature perturbation by microphysical heating are neglected in the vicinity of the PRE until 1200 UTC 10 Sep 2017.
PRE18	Like the PRE simulation, yet microphysical heating impacts are neglected until 1800 UTC 10 Sep 2017.
Irma	Contributions to the potential temperature perturbation by microphysical heating are neglected in the vicinity of Irma until 1200 UTC 10 Sep 2017.
PRE&Irma	Contributions to the potential temperature perturbation by microphysical heating are neglected in the vicinity of Irma and the PRE until 1200 UTC 10 Sep 2017.
PRE&IrmaWS	Like the PRE&Irma simulation, yet microphysical heating is neglected for the entirety of the simulation.

Table 3.1 Descriptions of the five sensitivity simulations performed.

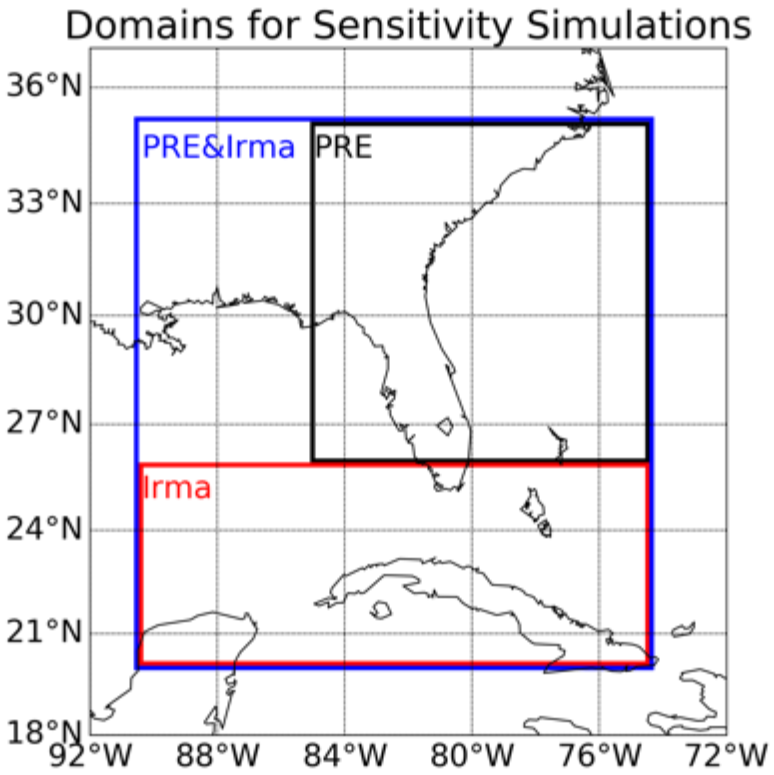

Figure 3.1. The spatial extent over which equation (3.2) is modified for the different sensitivity simulations. The PRE domain is utilized in the "PRE" and "PRE18" simulations. The Irma domain is utilized in the "Irma" simulation, and the PRE&Irma domain is utilized in the "PRE&Irma" and "PRE&IrmaWS" simulations.

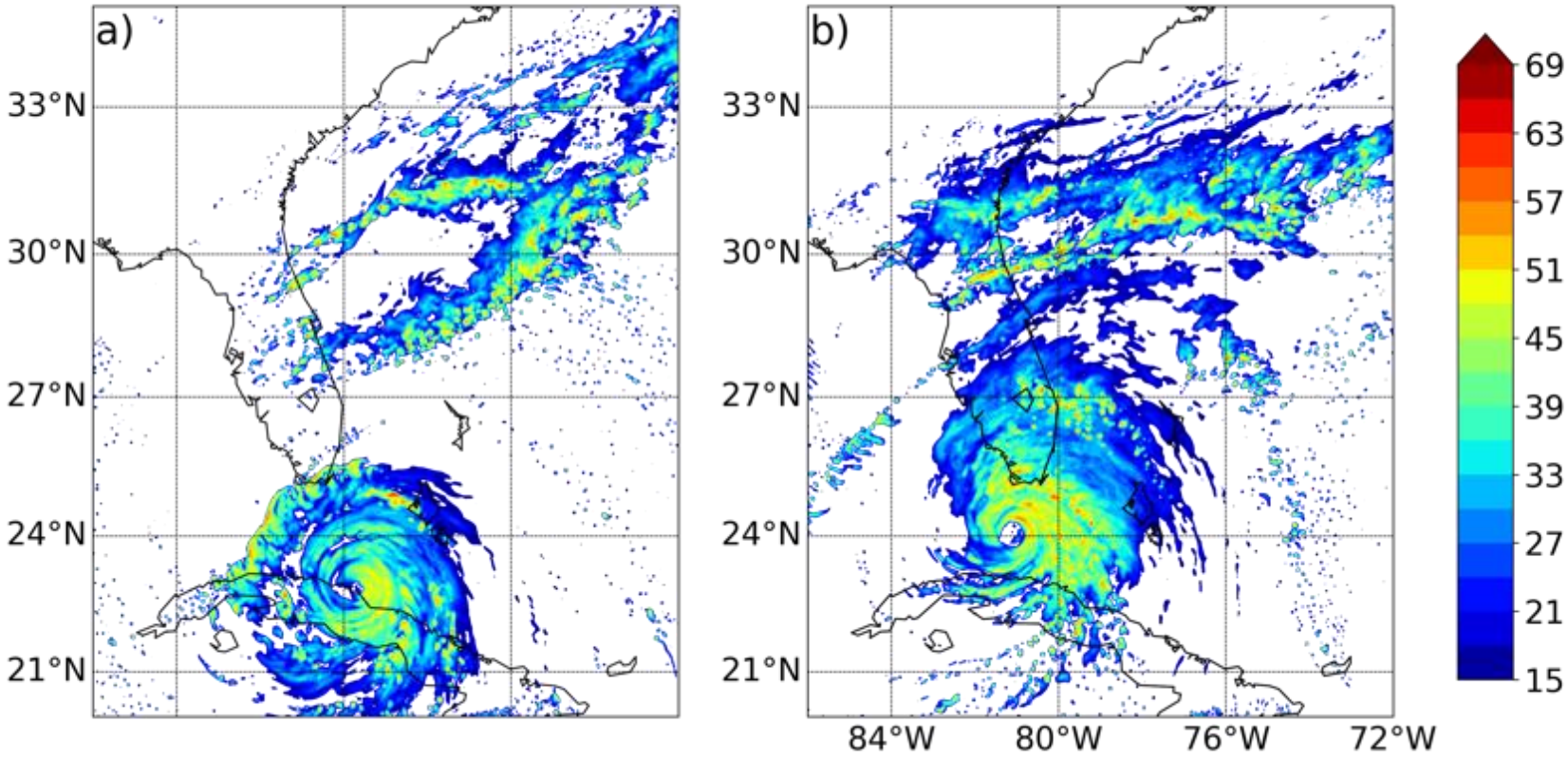

Figure 3.2. Maximum reflectivity (dBz; per the color bar on the right) at (a) 1600 UTC 9 September 2017 and (b) 1200 UTC 10 September 2017 encompassing the PRE off the eastern coast of northeastern Florida and southeastern Georgia and Irma.

3.3 Results

3.3.1 Convective-Scale PV in the PRE and TC Irma

Twenty-four hours into all simulations (0000 UTC 10 September 2017), deep, moist convection has already been active for several hours in both Irma and the PRE, producing intense convective-scale PV anomalies except for in regions where microphysical heating has been neglected (Figs. 3.2 and 3.3). Term two on the right-hand side of (3.2) can be visualized as the "warm bubble" caused by condensational warming in deep, moist convection, which, when neglected, severely weakens, or prevents the production of, intense updrafts. This lack of a "warm bubble" also prevents intense horizontal gradients of microphysical heating to be present, thus preventing the production of the PV anomalies discussed in Section 2 (Fig. 3.3). Additionally, the lack of deep, moist convection in the PRE appears to be associated with weaker poleward ridge amplification (compare latitude of the 8200 m isohypse between Figs. 3.3a,d and Figs. 3.3b,c,e,f). In simulations in which microphysical heating is turned off in the vicinity of Irma, there is a lack of convective-scale PV anomalies associated with convection embedded in spiral rainbands, yet a several-hundred-kilometer-wide positive PV anomaly persists as Irma's circulation slowly winds down (Fig. 3.3d-f). The PRE&IrmaWS simulation is associated with the weakest poleward ridge amplification across all simulations (Fig. 3.3f), potentially driven by a combination of the lack of mass transport to the middle- and upper-troposphere by deep, moist convection, and a weaker advection of warm, moist air transport northward by Irma's weaker primary circulation as the TC weakens (Fig. 3.3f).

By another twenty-four hours later (0000 UTC 11 Sep 2017), microphysical heating is active throughout the domain in all simulations apart from the PRE&IrmaWS simulation (Fig.

3.4). The Control simulation and all simulations which only limited microphysical heating in the PRE's vicinity show the remaining existence of a positive PV tower associated with Irma's core and are associated with a northward progression of the geopotential height contours (Fig. 3.4a-c). For simulations limiting microphysical heating in TC Irma, the cyclonic circulation and associated positive PV tower and geopotential height anomaly associated with the TC is substantially weaker (Fig. 3.4d,e) or no longer exists (Figs. 3.4f). The Control and removed-PRE-only simulations subsequently evolve similarly, with TC Irma's remnants travelling into the southeastern United States (Figs. 3.5a-c) and interacting favorably with the upstream trough (not shown). The Irma and PRE&Irma simulations show a slight northward progression of the geopotential contours off the southeastern Atlantic coast, yet are not quite as far north than in the the control and PRE only simulation (Figs. 3.5a-e). The PRE&IrmaWS simulation is the most drastically different from all other solutions, with no indications of downstream ridge building and a progression of the upstream trough much further to the east than any other simulation (Fig. 3.5).

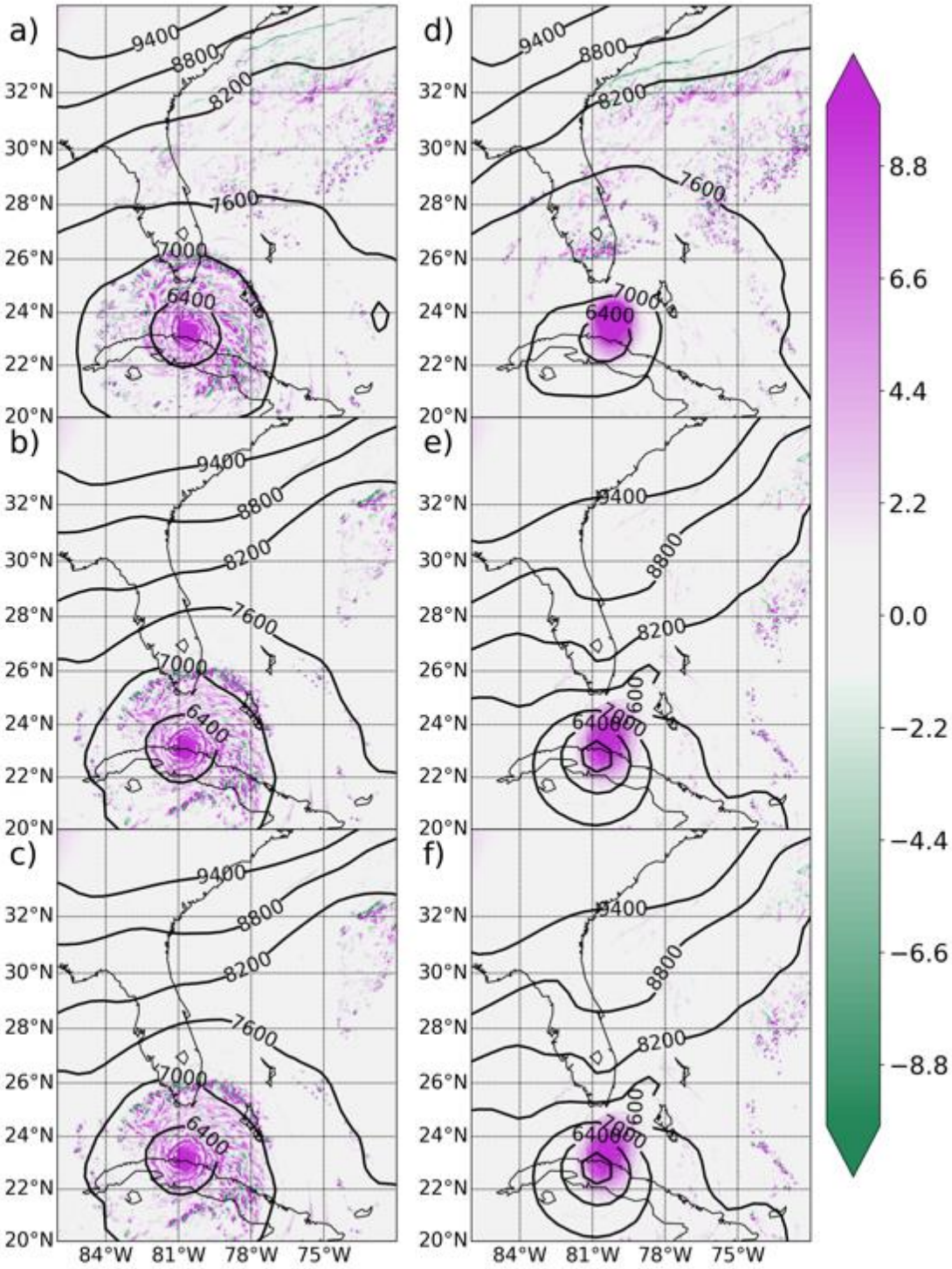

Figure 3.3. 335-K geopotential height (black contours every 600 m), and 335-K PV (shaded in PVU per the color bar at the right) for the (a) Control, (b) PRE, (c) PRE18, (d) Irma, (e) PRE&Irma, and (f) PRE&IrmaWS simulations at 0000 UTC 10 September 2017.

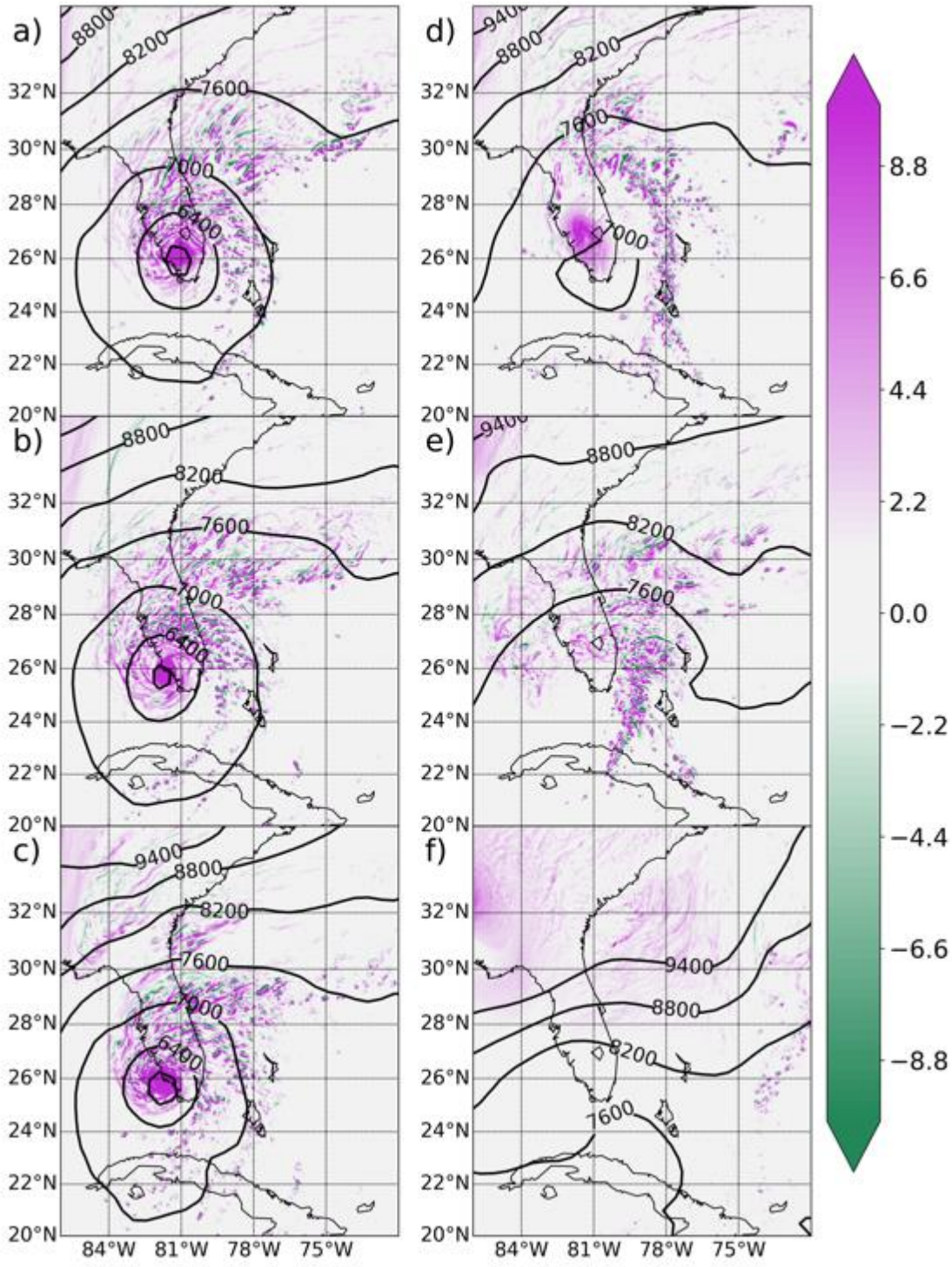

Figure 3.4. As in Figure 3.3 but for 0000 UTC 11 September 2017.

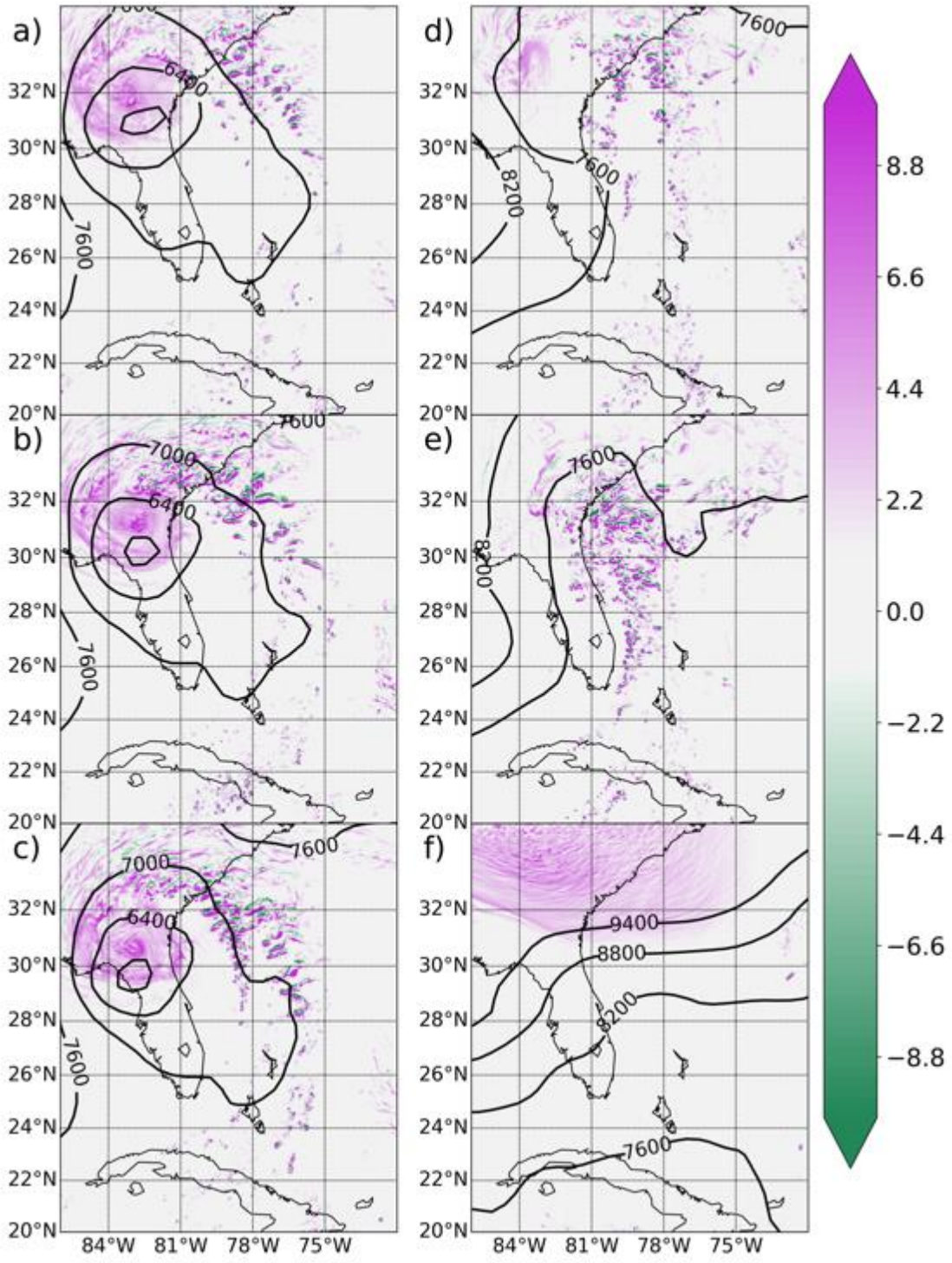

Figure 3.5. As in Figure 3.3 but for 0000 UTC 12 September 2017.

3.3.2 Downstream Impacts to Jose

Twenty-four hours into each simulation (0000 UTC 10 September 2017), TC Jose has an average maximum wind speed of approximately 112 knots and is travelling northeastward as it approaches a midlatitude ridge immediately downstream of TC Irma and the PRE (Figs. 3.6-3.7). At this time, TC Jose's circulation remains robust in every simulation, with a clear anticyclonic signature in the vertical wind shear vector extending several degrees away from the TC's center (Fig. 3.6). While the Control simulation does not accurately capture TC Jose's initial intensity, it does capture TC Jose's general weakening trend, with TC Jose's simulated intensity in the Control converging on the observed intensity within approximately 36 hours of the start of the simulations (Fig. 3.8).

By 48 hours into each simulation (0000 UTC 11 September 2017), the Control, PRE, and PRE18 simulations indicate a weakening TC Jose (Fig. 3.8). This weakening may be caused by TC Jose being in an environment of northerly vertical wind shear (Figs. 3.9a-c), which can support the intrusion of cooler, drier environmental air into the TC's circulation. Conversely, the Irma, PRE&Irma, and PRE&IrmaWS simulations indicate a strengthening TC Jose (Fig. 3.8). In simulations where TC Jose is weakening, the TC is on the eastern periphery of the midlatitude ridge as denoted by the broadly anticyclonic vertical wind shear vectors (Figs. 3.9a-c). Conversely, simulations which have TC Jose strengthening either have a weaker ridge, TC Jose directly underneath the ridge axis, or both (Figs. 3.9d-f).

By 0000 UTC 12 September 2017, in the Control, PRE, and PRE18 simulations, TC Jose has weakened to have an average maximum surface wind speed of 88 knots, while the Irma, PRE&Irma, and PRE&IrmaWS simulations have TC Jose attain an average maximum surface wind speed of 132 knots (Fig. 3.8). Additionally, two distinct patterns begin to arise in the track

of TC Jose. The Control, PRE, and PRE18 simulations have TC Jose largely undergoing a similar anticyclonic loop, while the Irma, PRE&Irma, and PRE&IrmaWS simulations have TC Jose either beginning to recurve into the midlatitudes, or largely remaining in place (Fig. 3.7). Like twenty-four hours previous, the simulations which have TC Jose weakening have the TC in an environment of northerly vertical wind shear on the eastern flank of the upstream trough, while the strengthening TC Jose simulations have the TC either directly under the ridge axis or slightly to the east of the ridge (Fig. 3.10).

Four days into each simulation (0000 UTC 13 September 2017), three distinct outcomes for TC Jose are evident. The first outcome is present in the Control, PRE, and PRE18 simulations, which all had TC Jose complete an anticyclonic loop while weakening to an average maximum wind speed of 88 knots (Figs. 3.7 and 3.8). Consistent with previous times, the weakening simulations continue to have TC Jose placed on the eastern edge of the midlatitude ridge, and in an environment of northerly vertical wind shear, which is likely advecting cool moist air into the TC (Fig. 3.11a-c). The second outcome is evident in the Irma and PRE&Irma simulations, in which TC Jose largely remains in place before slowly travelling northwestward while keeping TC Jose comfortably at an average maximum surface wind speed of 146 knots (Figs. 3.7 and 3.8). In these simulations, TC Jose remains in an environment of weak steering flow and vertical wind shear, allowing the storm to remain in place and strengthen (Figs. 3.11d,e). Finally, the third outcome is evident in the PRE&IrmaWS simulation, in which TC Jose weakens slightly as it begins to recurve ahead of the trough that progresses eastward in the absence of both TC Irma and the PRE (Figs. 3.7, 3.8, and 3.11f).

Summarizing, simulations in which microphysical heating is temporarily neglected exclusively within the PRE have solutions for TC Jose that are very similar to that in the Control

simulation, suggesting that the evolution of this TC-midlatitude waveguide interaction is largely insensitive to the existence of the PRE (Figs. 3.6-3.11). Conversely, simulations in which microphysical heating is temporarily or permanently neglected within TC Irma are associated with downstream synoptic-scale flow evolutions that are quite different than that within the Control simulation (Figs. 3.6-3.11). These varying evolutions lead to TC Jose either remaining in place, or recurving, as opposed to undergoing an anticyclonic loop, and strengthening rather than weakening (Figs. 3.7 and 3.8).

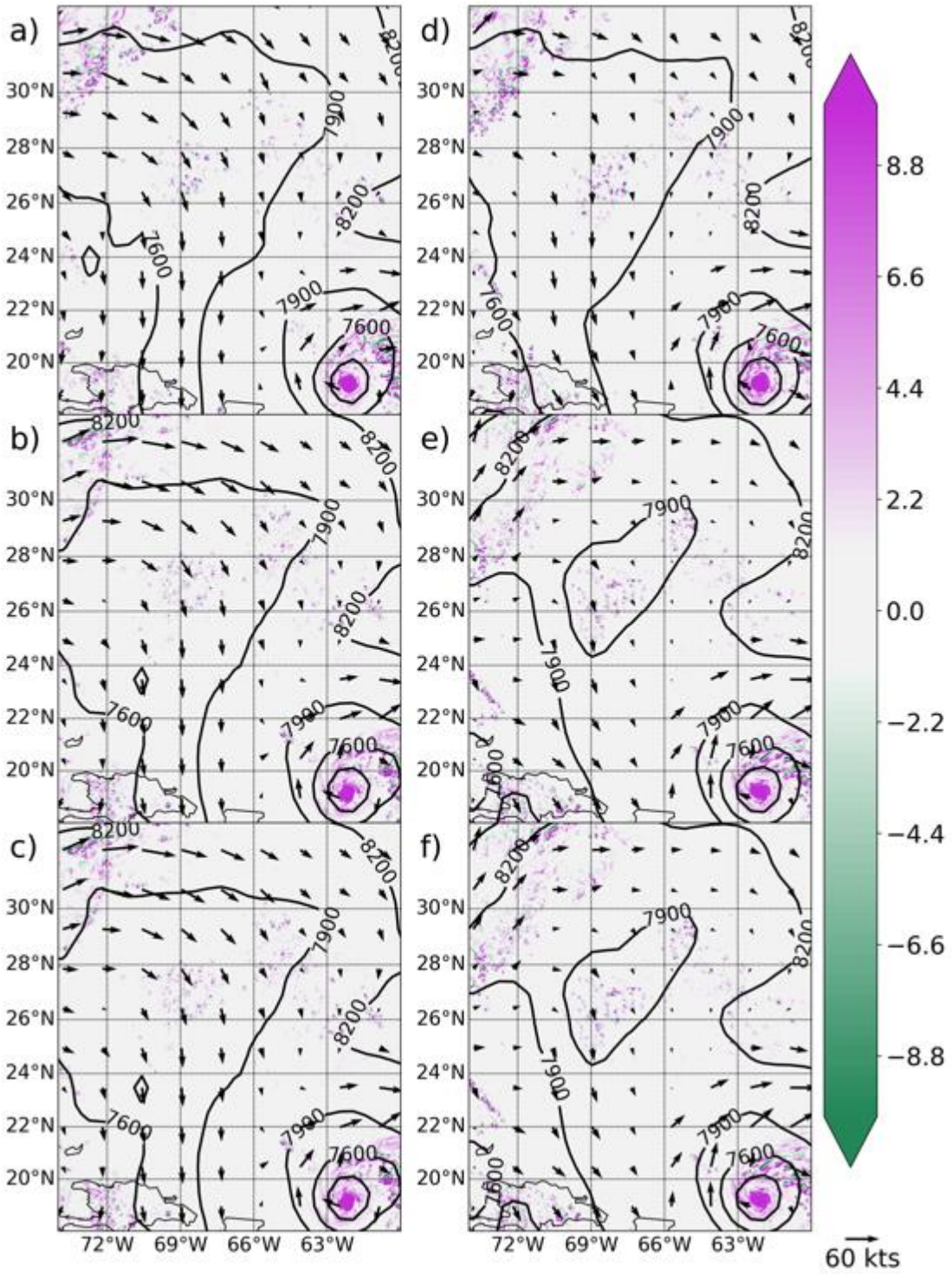

Figure 3.6. 335-K geopotential height (black contours every 300 m), 335-K PV (shaded in PVU per the color bar at the right), and 350-to-320–K vertical wind shear (vectors; kt; reference vector at lower right) for the (a) Control, (b) PRE, (c) PRE18, (d) Irma, (e) PRE&Irma, and (f) PRE&IrmaWS simulations at 0000 UTC 10 September 2017.

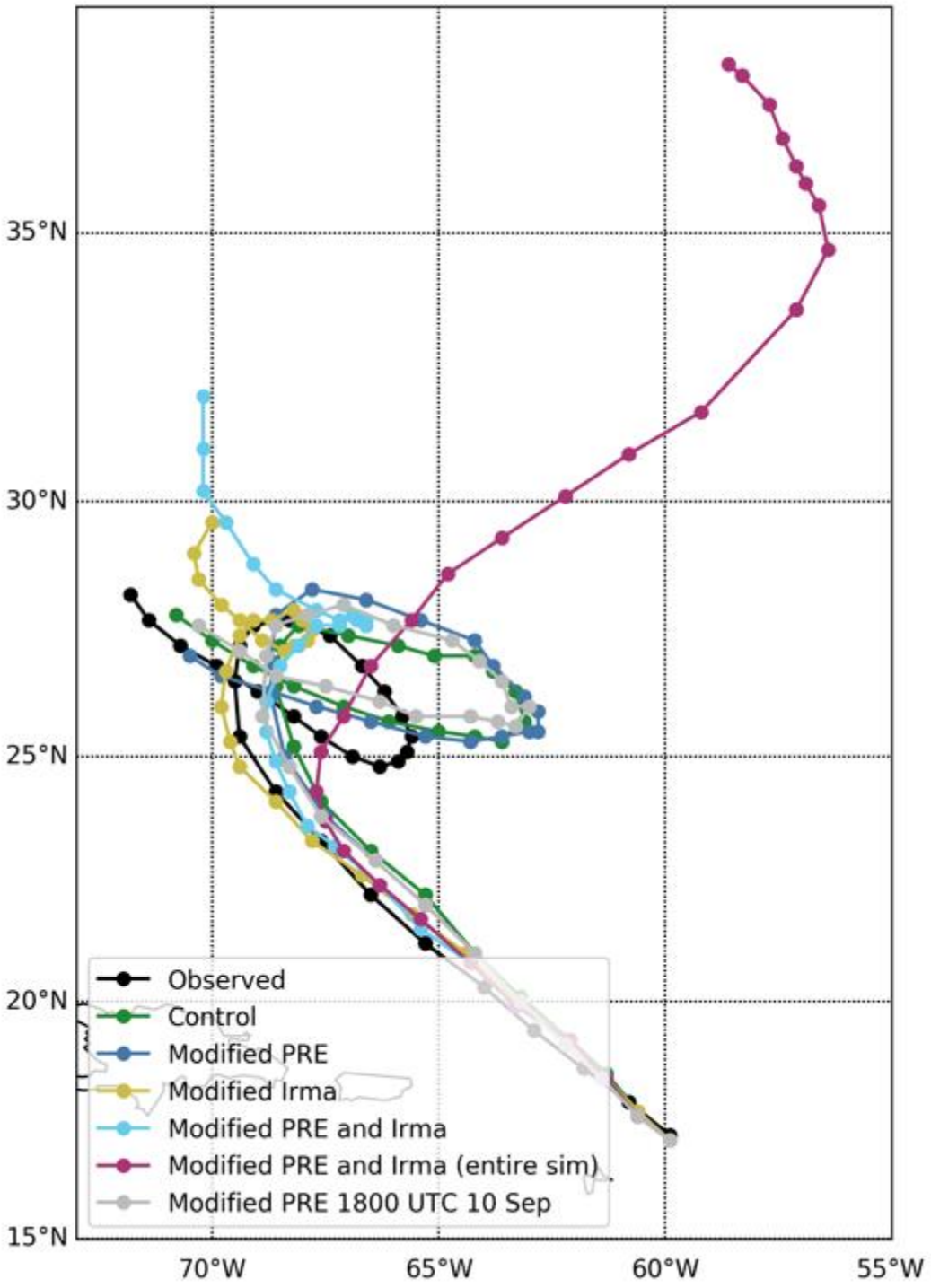

Figure 3.7. TC Jose forecast center location for the control and five sensitivity simulations given in Table 3.1 and the control every six hours from 0600 UTC 9 September to 1200 UTC 16 September 2017.

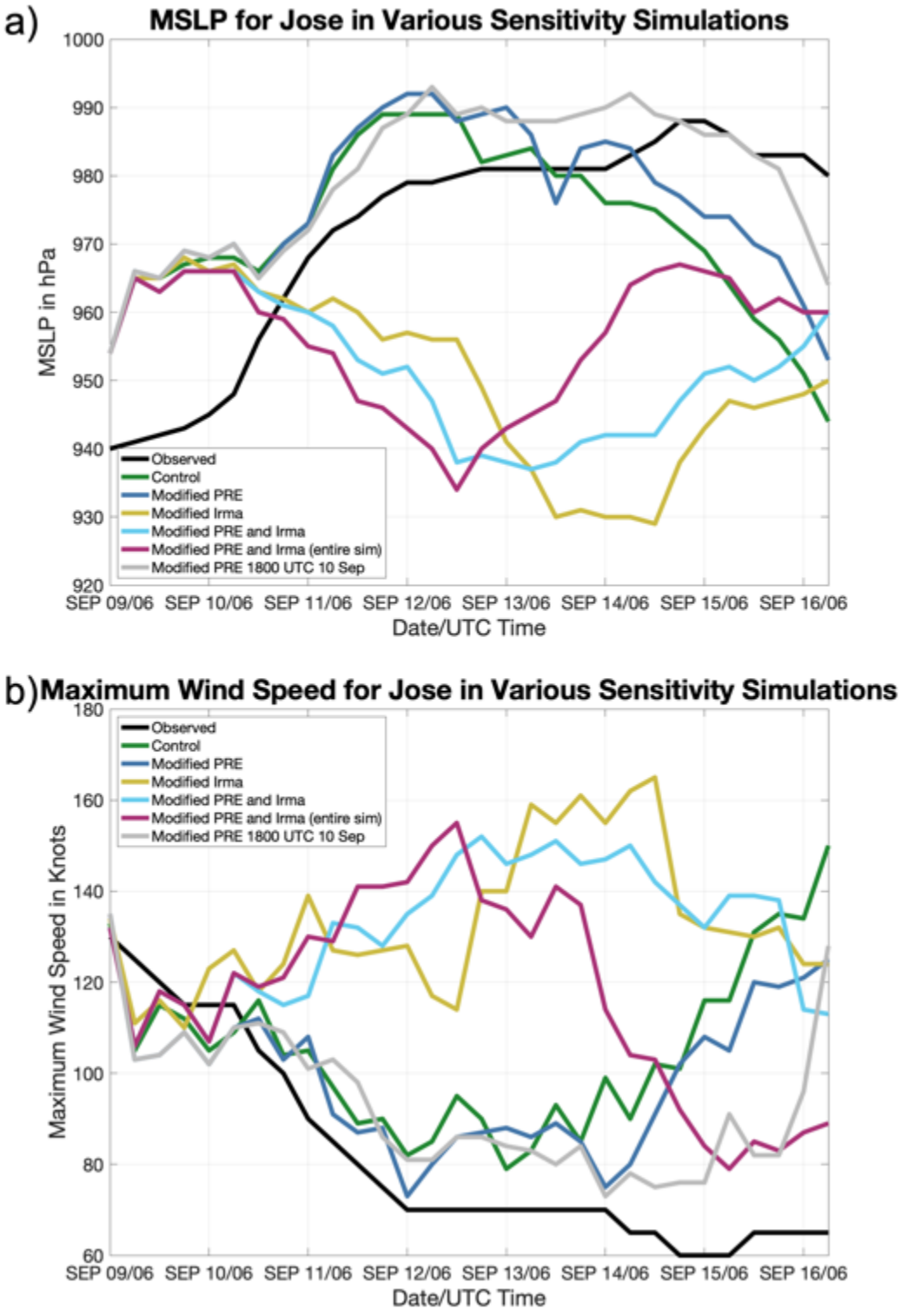

Figure 3.8. TC Jose forecast (a) minimum Mean Sea Level Pressure (MSLP) in hPa, and (b) maximum instantaneous 10 m wind speed in knots every six hours from 0600 UTC 9 September to 1200 UTC 16 September 2017 for all sensitivity simulations in Table 3.1 and the control.

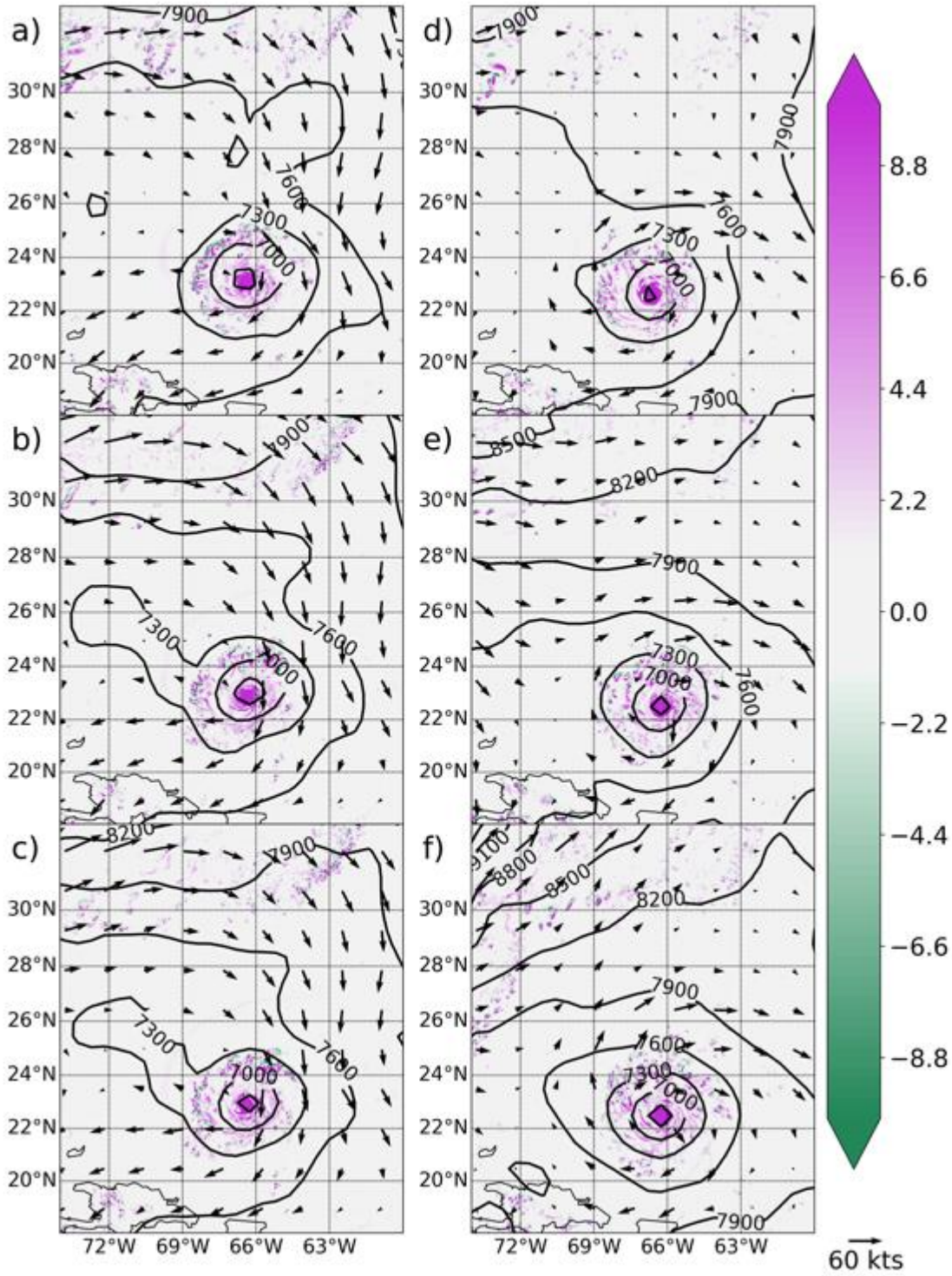

Figure 3.9. As in Figure 3.6 but at 0000 UTC 11 September 2017.

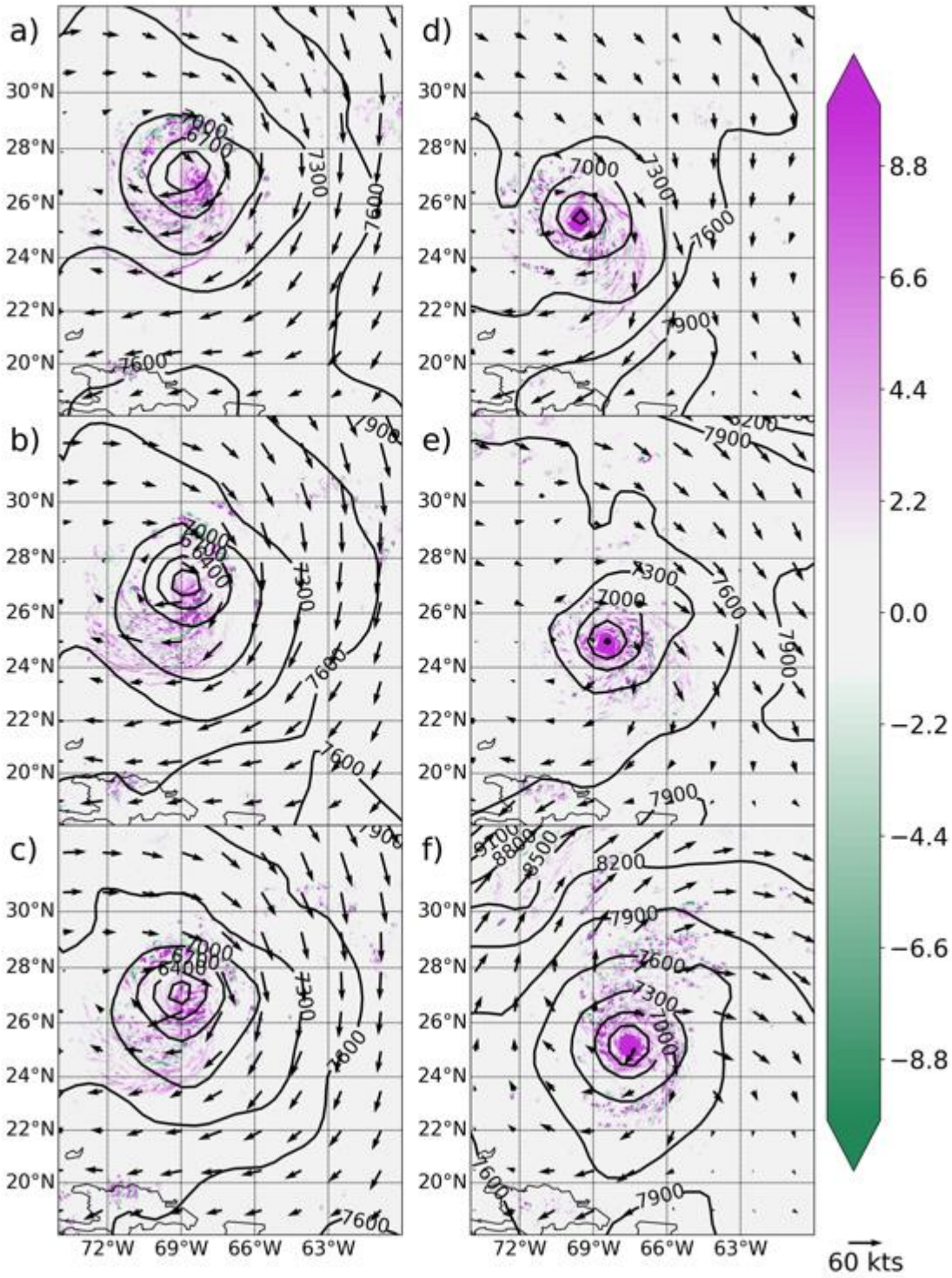

Figure 3.10. As in Figure 3.6 but at 0000 UTC 12 September 2017.

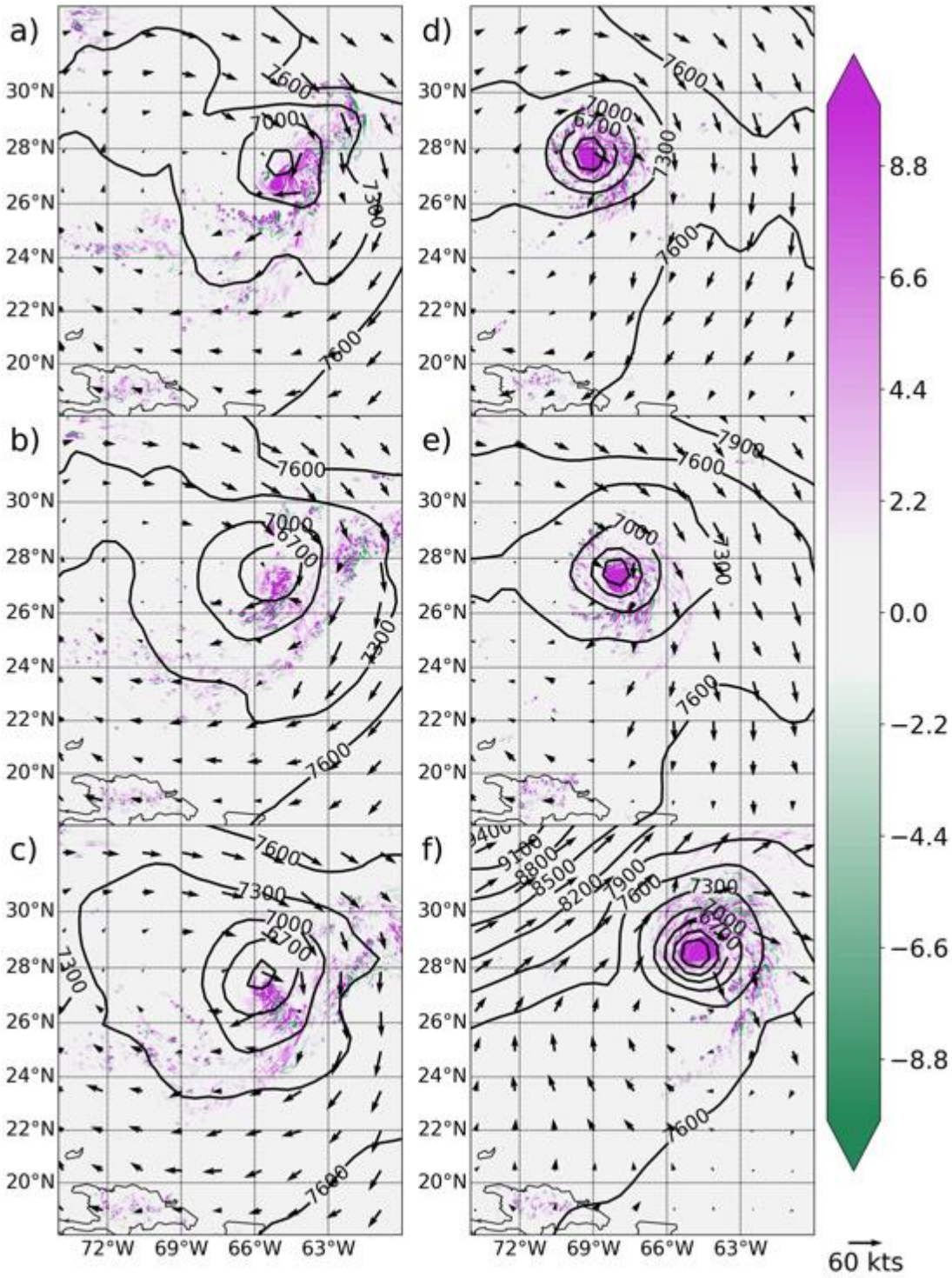

Figure 3.11. As in Figure 3.6 but at 0000 UTC 13 September 2017.

3.4 Conclusions

Ultimately, limiting microphysical heating in the PRE only has minimal impacts on the evolution of the simulation, independent of the amount of time over which the microphysical heating is limited (Figs. 3.6-3.11). Additionally, the minimal impacts that turning off microphysical heating in the PRE have on the simulation were limited locally in both space and time, such that the PRE and PRE18 simulations converge on a similar solution to the control within approximately 36 hours of initialization (Figs. 3.6-3.11). Conversely, turning off microphysical heating in TC Irma has a much more significant impact, both locally and remotely, on the evolution of the simulation. The Irma and PRE&Irma simulations did not differ much from each other yet modified the strength of the ridge immediately downstream of the PRE and TC Irma, causing the track, and subsequent intensity, of TC Jose to evolve very differently. Finally, the PRE&IrmaWS simulation suggests that in the absence of both TC Irma and the PRE entirely, the upstream trough with which they interacted in the control will progress eastward causing TC Jose to recurve rather than undergo an anticyclonic loop.

While temporarily neglecting microphysical heating in the vicinity of the PRE does not appear to exert a significant influence on the outcome of this particular TC-midlatitude waveguide interaction, it does not necessarily mean the PRE does not matter in all TC-midlatitude waveguide interactions. Section 2 of this study finds that convective-scale elements in the PRE, and possibly a TC, can support an inverse cascade of energy from small to large scales, thus having a potential impact on the evolution of the large-scale dynamics.

One issue with the methodology employed in this study, however, is the production of spurious deep, moist convection along the boundaries of the regions over which microphysical heating is neglected. For example, in the PRE&IrmaWS simulation, convective-scale PV not

only persists for over 24-h off the coast of Louisiana, but congeals into a larger-scale feature indicative of tropical cyclonegenesis (Fig. 3.12). This feature is not present in the either the Control simulation or observed data (not shown). Another drawback of the simulations which turn off the microphysical heating in the vicinity of TC Irma is the time it takes for the circulation of TC Irma to wind-down as it is continually starved of microphysical heating. One potential impact of TC Irma's remaining dynamical influence is the warm, moist air advection on the eastern flank of the TC, potentially supplying moisture to the PRE even as Irma weakens. Future techniques, such as PV inversion and spectral filtering to the microphysical heating field, will be employed to address these issues.

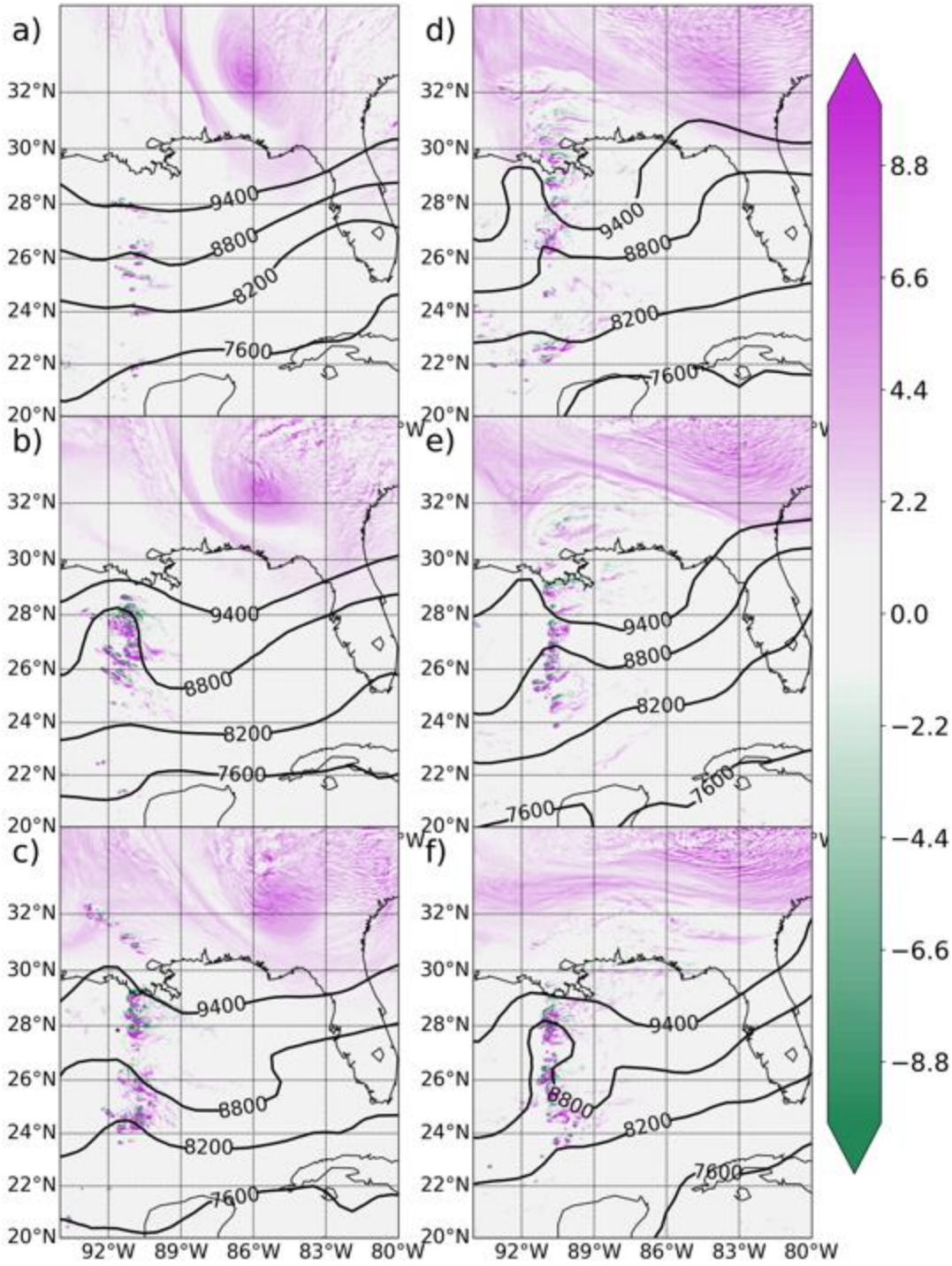

Figure 3.12. 335-K geopotential height (black contours every 600 m), and 335-K PV (shaded in PVU per the color bar at the right) for the PRE&IrmaWS simulation at (a) 0000 UTC, (b) 0600 UTC, (c) 1200 UTC, (d) 1800 UTC 11 September, and (e) 0000 UTC, (f) 0600 UTC 12 September 2017.

Chapter 4

Main Takeaways

Substantial research has been published on the interaction of TCs with the midlatitude flow as they recurve into the midlatitudes and undergo ET, including the associated reduction in downstream midlatitude predictability. This three-part study has contributed two published works to the literature, furthering knowledge on the impacts to a TC downstream of a TC-trough interaction (Prince and Evans 2020) and the sensitivity to a TC-trough interaction to convective-scale processes (Prince and Evans 2022).

Part 1 of this study performs a climatology of indirect interactions, where twenty-six and 56 indirect interactions are identified in the North Atlantic (Table 1.1) and western North Pacific (Table 1.2) basins, respectively. Part 1 of the study also identifies two pathways by which a secondary TC can weaken following an indirect-interaction event. In the North Atlantic, weakening secondary TCs are closer to the midlatitude waveguide on the southeastern edge of the amplified midlatitude ridge (consistent with Fowler and Galarneau 2017), whereas strengthening secondary TCs are further from the waveguide and equatorward of the amplified midlatitude ridge (Table 1.3; Fig. 1.16, bottom left). Conversely, western North Pacific strengthening and weakening secondary TCs are primarily stratified by latitude, with weakening secondary TCs located nearly 6° latitude poleward of their strengthening secondary TC counterparts at the time of maximum interaction, as opposed to their positions relative to the midlatitude pattern (Fig. 1.16, bottom right). Strengthening secondary TCs remain well-equatorward of the midlatitude waveguide and are largely unaffected by changes in the midlatitude flow, whereas weakening secondary TCs rapidly approach the midlatitude

waveguide following the time of maximum interaction (Table 1.4; Fig. 1.16, bottom right). This insight can foster increased forecaster situational awareness during future indirect-interaction events that may allow them to make more-skillful secondary-TC intensity forecasts during and after the time of maximum interaction.

Part 2 of this study identifies the physical processes that allow for thunderstorm-scale PV anomalies to modify the synoptic-scale flow and can be conceptualized as follows (Fig. 2.14). When a thunderstorm initiates within a vertically sheared flow, such as one found on the eastern flank of an upstream midlatitude trough, its associated horizontal gradients of microphysical heating generate PV anomalies aligned perpendicular to the background vertical wind shear vector, with negative PV anomalies to the left of the shear vector and positive PV anomalies to the right of the shear vector (Figs. 2.6 and 2.7ab). On the eastern flank of the upstream trough and to the north of TC Irma, the large-scale strain field can be approximated as having an axis of dilatation oriented from southwest to northeast (Fig. 2.12). This large-scale strain deforms the convectively generated PV anomalies, stretching them along the axis of dilatation (Figs. 2.6ac). The newly deformed PV anomaly covers a larger area than it did before, such that from the circulation theorem its rotation rate must decrease. Due to the alignment of the deformed anomaly with the large-scale strain field, a tensile stress is applied to the large-scale strain, thus reinforcing the large-scale strain, and adding energy to the large-scale flow (Fig. 2.14). The inverse energy cascade is accomplished by the filamentation of the negative PV anomalies (Fig. 2.14).

The final part of this study performs a series of sensitivity simulations on the TC-midlatitude waveguide interaction involving a PRE and TCs Irma and Jose which is studied in part 2. Preliminary results suggest that convection inside of the PRE had a negligible impact on

the downstream evolution, as limiting convection inside of the PRE over varying time periods results in a solution like the Control (Figs. 3.3-3.6a-c, 3.7, 3.8, and 3.9-3.11a-c). The only solutions which show meaningful impacts to the downstream flow evolution and TC Jose are those in which microphysical heating is neglected with TC Irma (Figs. 3.3-3.6d-f, 3.7, 3.8, and 3.9-3.11d-f). While these findings suggest that the inverse cascade of energy identified in Section 2 may not have a meaningful enough impact on the large-scale flow to drastically change the evolution of this particular TC-midlatitude waveguide interaction, it does not necessarily mean it is negligible for all TC-midlatitude waveguide interactions.

Works Cited

Agustí-Panareda, A., C. D. Thorncroft, G. C. Craig, and S. L. Gray, 2004: The extratropical transition of Hurricane Irene (1999): A potential-vorticity perspective. *Quart. J. Roy. Meteor. Soc.*, **130**, 1047–1074, https://doi.org/10.1256/qj.02.140.

Agustí-Panareda, A., S. L. Gray, G. C. Craig, and C. Thorncroft, 2005: The extratropical transition of Tropical Cyclone Lili (1996) and its crucial contribution to a moderate extratropical development. *Mon. Wea. Rev.*, **133**, 1562–1573, https://doi.org/10.1175/MWR2935.1.

Aiyyer, A., 2015: Recurving western North Pacific tropical cyclones and midlatitude predictability. *Geophys. Res. Lett.*, **42**, 7799–7807, https://doi.org/10.1002/2015GL065082.

Anwender, D., P. A. Harr, and S. C. Jones, 2008: Predictability associated with the downstream impacts of the extratropical transition of tropical cyclones: Case studies. *Mon. Wea. Rev.*, **136**, 3226–3247, https://doi.org/10.1175/2008MWR2249.1.

Anwender, D., S. C. Jones, M. Leutbecher, and P. A. Harr, 2010: Sensitivity experiments for ensemble forecasts of the extratropical transition of Typhoon Tokage (2004). *Quart. J. Roy. Meteor. Soc.*, **136**, 183–200, https://doi.org/10.1002/qj.527.

Archambault, H.M., L. F. Bosart, D. Keyser, and J.M. Cordeira, 2013: A Climatological analysis of the extratropical flow response to recurving western North Pacific tropical cyclones. *Mon. Wea. Rev.*, **141**, 2325–2346, https://doi.org/10.1175/MWR-D-12-00257.1.

Archambault, H. M., D. Keyser, L. F. Bosart, C. A. Davis, and J. M. Cordeira, 2015: A composite perspective of the extratropical flow response recurving western North Pacific tropical cyclones. *Mon. Wea. Rev.*, **143**, 1122–1141, https://doi.org/10.1175/MWR-D-14-00270.1.

Banzon, V., T. M. Smith, T. M. Chin, C. Liu, and W. Hankins, 2016: A long-term record of blended satellite and in situ sea-surface temperature for climate monitoring, modeling and environmental studies. *Earth Syst. Sci. Data*, **8**, 165–176, doi:10.5194/essd-8-165-2016.

Berg, R., 2018: National Hurricane Center Tropical Cyclone Report: Hurricane Jose (AL122017). [Available online at https://www.nhc.noaa.gov/data/tcr/AL122017_Jose.pdf.]

Bloomfield, P., 2000: *Fourier Analysis of Time Series: An Introduction*. New York: Wiley-Interscience, 261 pp.

Bosart, L. F., and F. H. Carr, 1978: A case study of excessive rainfall centered around Wellsville, New York, 20–21 June 1972, *Mon. Wea. Rev*, **106**, 348-362, https://doi.org/10.1175/1520-0493(1978)106<0348:ACSOER>2.0.CO;2.

Bosart, L. F., 2003: Tropopause folding: upper-level frontogenesis, and beyond. *Meteor. Monogr.*, Amer. Meteor. Soc., **31**, 13–47. doi:10.1175/0065-9401-31.53.13.

Cangialosi, J. P., 2018: National Hurricane Center forecast verification report: 2017 hurricane season. NOAA, 73 pp., https://www.nhc.noaa.gov/verification/pdfs/Verification_2017.pdf.

Chagnon, J. M. and S. L. Gray, 2009: Horizontal potential vorticity dipoles on the convective storm scale, *Quart. J. Roy. Meteor. Soc*.,**135**, 1392–1408, https://doi.org/10.1002/qj.468.

Chen, S., R. E. Ecke, G. L. Eyink, M. Rivera, M. Wan, and Z. Xiao, 2006: Physical mechanism of the two-dimensional inverse energy cascade, *Phys. Rev. Lett*., **96**, 084502(4), https://link.aps.org/doi/10.1103/PhysRevLett.96.084502.

Colbert, A. J., and B. J. Soden, 2012: Climatological variations in North Atlantic tropical cyclone tracks. *J. Climate*, **25**, 657–673, doi:10.1175/JCLI-D-11-00034.1.

Cote, M. R., 2007: Predecessor rain events in advance of tropical cyclones. M.S. thesis, Department of Atmospheric and Environmental Sciences, University at Albany, State University of New York, 200 pp.

Cunningham, P., and D. Keyser, 2000: Analytical and numerical modelling of jet streaks: Barotropic dynamics. *Quart. J. Roy. Meteor. Soc*., **126**, 3187–3217, doi:10.1002/qj.49712657010.

Davies-Jones, R. P., 1986: Tornado dynamics. *Thunderstorm Morphology and Dynamics*, E. Kessler, Ed., University of Oklahoma Press, 197–236.

Dee, D., and Coauthors, 2011: The ERA-Interim reanalysis: Configuration and performance of the data assimilation system. *Quart. J. Roy. Meteor. Soc.*, **137**, 553–597, https://doi.org/10.1002/qj.828.

Dudhia, J., 1989: Numerical study of convection observed during the Winter Monsoon Experiment using a mesoscale two–dimensional model. *J. Atmos. Sci*., **46**, 3077–3107, https://doi.org/10.1175/1520-0469(1989)046%3C3077:NSOCOD%3E2.0.CO;2.

Efron, B., and R. Tibshirani, 1994: *An Introduction to the Bootstrap*. London: Chapman & Hall, 456pp.

Evans, C., and Coauthors, 2017: The extratropical transition of tropical cyclones. Part I: Cyclone evolution and direct impacts. *Mon. Wea. Rev*., **145**, 4317–4344, https://doi.org/10.1175/MWR-D-17-0027.1.

Eyink, G., 2006a: Multi-scale gradient expansion of the turbulent stress tensor. *J. of Fluid Mech*, **549**, 159-190, https://doi:10.1017/S0022112005007895.

Eyink, G., 2006b: A turbulent constitutive law for the two-dimensional inverse energy cascade. *J. of Fluid Mech.*, **549**, 191-214, https://doi:10.1017/S0022112005007883.

Finocchio, P. M. and J. D. Doyle, 2019: How the speed and latitude of the jet stream affect the downstream response to recurving tropical cyclones. *Mon. Wea. Rev.*, **147**, 3261–3281, https://doi.org/10.1175/MWR-D-19-0049.1.

Fischer, M. S., B. H. Tang, and K. L. Corbosiero, 2017: Assessing the influence of upper-tropospheric troughs on tropical cyclone intensification rates after genesis. *Mon. Wea. Rev.*, **145**, 1295–1313, https://doi.org/10.1175/MWR-D-16-0275.1.

Fowler, J. P., and T. J. Galarneau, 2017: Influence of storm–storm and storm–environment interactions on tropical cyclone formation and evolution. *Mon. Wea. Rev.*, **145**, 4855–4875, https://doi.org/10.1175/MWR-D-17-0131.1.

Franklin, J. L., 2006: Tropical cyclone report: Hurricane Philippe (2005). [Available online at https://www.nhc.noaa.gov/data/tcr/AL172005_Philippe.pdf.]

Fujiwhara, S., 1921: The natural tendency towards symmetry of motion and its application as a principle in meteorology. *Quart. J. Roy. Meteor. Soc*., **47**, 287–292, https://doi.org/10.1002/qj.49704720010.

Galarneau, T. J., Jr., L. F. Bosart, and R. S. Schumacher, 2010: Predecessor rain events ahead of tropical cyclones, *Mon. Wea. Rev.*, **138**, 3272-3297, https://doi.org/10.1175/2010MWR3243.1.

Galarneau, T. J. and C. A. Davis, 2013: Diagnosing forecast errors in tropical cyclone motion. *Mon. Wea. Rev.*, **141**, 405–430, https://doi.org/10.1175/MWR-D-12-00071.1.

Galarneau, T. J., Jr., R. McTaggart-Cowan, L. F. Bosart, and C. A. Davis, 2015: Development of north Atlantic tropical disturbances near upper-level potential vorticity streamers. *J. Atmos. Sci.*, **72**, 572–597, https://doi.org/10.1175/JAS-D-14-0106.1.

Grams, C. M., and Coauthors, 2011: The key role of diabatic processes in modifying the upper-tropospheric wave guide: A North Atlantic case-study. *Quart. J. Roy. Meteor. Soc*., **137**, 2174–2193, https://doi.org/10.1002/qj.891.

Grams, C. M., S. C. Jones, C. A. Davis, P. A. Harr, and M. Weissmann, 2013a: The impact of Typhoon Jangmi (2008) on the midlatitude flow. Part I: Upper-level ridgebuilding and modification of the jet. *Quarterly Journal of the Royal Meteorological Society*, **139**, 2148-2164, doi:10.1002/qj.2091.

Grams, C. M., S. C. Jones, and C. A. Davis, 2013b: The impact of Typhoon Jangmi (2008) on the midlatitude flow. Part II: downstream evolution. *Quart. J. Roy. Meteor. Soc.*, **139**, 2165–2180, https://doi.org/10.1002/qj.2119.

Grams, C. M., S. T. K. Lang, and J. H. Keller, 2015: A quantitative assessment of the sensitivity of the downstream midlatitude flow response to extratropical transition of tropical cyclones. *Geophys. Res. Lett.*, **42**, 9521–9529, https://doi.org/10.1002/2015GL065764.

Grams, C. M., and H. M. Archambault, 2016: The key role of diabatic outflow in amplifying the midlatitude flow: a representative case study of weather systems surrounding western North Pacific extratropical transition. *Mon. Wea. Rev.*, **144**, 3847–3869, https://doi.org/10.1175/MWR-D-15-0419.1.

Gray, W. M., 1968: Global view of the origin of tropical disturbances and storms. *Mon. Wea. Rev.*, **96**, 669–700, https://doi.org/10.1175/1520-0493(1968)096<0669:GVOTOO>2.0.CO;2.

Harr, P. A., and J. M. Dea, 2009: Downstream development associated with the extratropical transition of tropical cyclones over the western North Pacific. *Mon. Wea. Rev.*, **137**, 1295–1319, https://doi.org/10.1175/2008MWR2558.1.

Harr, P. A., and H. M. Archambault, 2016: Dynamics, predictability, and high-impact weather associated with the extratropical transition of tropical cyclones. Dynamics and predictability of large-scale, high-impact weather and climate events, J. Li et al., Eds., Cambridge University Press, 153–167, https://doi.org/10.1017/CBO9781107775541.013.

Hart, R. E., R. N. Maue, and M. C. Watson, 2007: Estimating local memory of tropical cyclones through MPI anomaly evolution. *Mon. Wea. Rev.*, **135**, 3990–4005, https://doi.org/10.1175/2007MWR2038.1.

Hersbach, H., and Coauthors, 2020: The ERA5 global reanalysis. *Quart. J. Roy. Meteor. Soc.*, **146**, 1999– 2049. https://doi.org/10.1002/qj.3803.

Hodges, K., D. Anwender, and S. C. Jones, 2008: Predictability associated with the downstream impacts of the extratropical transition of tropical cyclones: Methodology and a case study of Typhoon Nabi (2005). *Mon. Wea. Rev.*, **136**, 3205–3225, https://doi.org/10.1175/2008MWR2248.1.

Hong, S.–Y., N. Yign, and J. Dudhia, 2006: A new vertical diffusion package with an explicit treatment of entrainment processes. *Mon. Wea. Rev.*, **134**, 2318–2341, https://doi.org/10.1175/MWR3199.1.

Hong, S.–Y., and J.–O. J. Lim, 2006: The WRF single–moment 6–class microphysics scheme (WSM6). *J. Korean Meteor. Soc.*, **42**, 129–151, https://doi.org/10.1155/2016/5094126.

Hoskins, B. J., M. E. McIntyre, and A. W. Robertson, 1985: On the use and significance of isentropic potential vorticity maps. *Quart. J. Roy. Meteor. Soc.*, **111**, 877–946, https://doi.org/10.1002/qj.49711147002.

Huffman, G. J., E. F. Stocker, D. T. Bolvin, E. J. Nelkin, and J. Tan, 2019: GPM IMERG Final Precipitation L3 1 day 0.1 degree x 0.1 degree V06, Edited by Andrey Savtchenko, Greenbelt, MD, Goddard Earth Sciences Data and Information Services Center (GES DISC), Accessed 16 September 2019, https://doi:10.5067/GPM/IMERGDF/DAY/06.

Jiménez, P. A., J. Dudhia, J.F. González-Rouco, J. Navarro, J.P. Montávez, and G.-E. Bustamante, 2012: A revised scheme for the WRF surface layer formulation. *Mon. Wea. Rev*., **140**, 898–918, https://doi.org/10.1175/MWR-D-11-00056.1.

Jones, S. C., and Coauthors, 2003: The extratropical transition of tropical cyclones: Forecast challenges, current understanding, and future directions. *Wea. Forecasting*, **18**, 1052–1092, https://doi.org/10.1175/1520-0434(2003)018<1052:TETOTC>2.0.CO;2.

JTWC, cited 2018: Best Track Data. Joint Typhoon Warning Center, accessed December 2018. [Available online at https://www.metoc.navy.mil/jtwc/jtwc.html?western-pacific.]

Keller, J. H., 2017: Amplification of the downstream wave train during extratropical transition: sensitivity studies. *Mon. Wea. Rev.*, **145**, 1529–1548, https://doi.org/10.1175/MWR-D-16-0193.1.

Keller, J. H., S. C. Jones, J. L. Evans, and P. A. Harr, 2011: Characteristics of the TIGGE multimodel ensemble prediction system in representing forecast variability associated with extratropical transition. *Geophys. Res. Lett.*, **38**, L12802, doi:10.1029/2011GL047275.

Keller, J. H., and coauthors, 2019: The extratropical transition of tropical cyclones II: interaction with the midlatitude flow, downstream impacts, and implications for predictability. *Mon. Wea. Rev.*, **147**, 1077-1106, https://doi.org/10.1175/MWR-D-17-0329.1.

Klotzbach, P. J., 2010: On the Madden–Julian Oscillation–Atlantic hurricane relationship. *J. Climate*, **23**, 282–293, https://doi.org/10.1175/2009JCLI2978.1.

Klotzbach, P. J., 2014: The Madden–Julian Oscillation's impacts on worldwide tropical cyclone activity. *J. Climate*, **27**, 2317–2330, https://doi.org/10.1175/JCLI-D-13-00483.1.

Komaromi, W. A., S. J. Majumdar, and E. D. Rappin, 2011: Diagnosing initial condition sensitivity of typhoon Sinlaku (2008) and hurricane Ike (2008). *Mon. Wea. Rev.*, **139**, 3224–3242, https://doi.org/10.1175/MWR-D-10-05018.1.

Komaromi, W. A., and J. D. Doyle, 2018: On the dynamics of tropical cyclone and trough interactions. *J. Atmos. Sci*., **75**, 2687–2709, https://doi.org/10.1175/JAS-D-17-0272.1.

Kraichnan, R. H., 1967. Inertial ranges in two-dimensional turbulence, *Phys. Fluids*,**16**, 1417–1423, https://doi:10.1063/1.1762301.

Krouse, K. D., A. H. Sobel, and L. M. Polvani, 2008: On the wavelength of the Rossby waves radiated by tropical cyclones. *J. Atmos. Sci*., **65**, 644–654, https://doi.org/10.1175/2007JAS2402.1.

Lackmann, G., 2011: *Midlatitude Synoptic Meteorology: Dynamics, Analysis, and Forecasting*. American Meteorological Society, 345 pp.

Landsea, C. W., 2007: Counting Atlantic tropical cyclones back to 1900. *Eos*, **88**, 197–202, https:// doi.org/10.1029/2007EO180001.

Landsea, C. W. and J. L. Franklin, 2013: Atlantic hurricane database uncertainty and presentation of a new database format. *Mon. Wea. Rev*., **141**, 3576-3592, https://doi.org/10.1175/MWR-D-12-00254.1.

Li, R. C. and W. Zhou, 2013: Modulation of western North Pacific tropical cyclone activity by the ISO. Part II: tracks and landfalls. *J. Climate*, **26**, 2919–2930, https://doi.org/10.1175/JCLI-D-12-00211.1.

McTaggart-Cowan, R, L. F. Bosart, J. R. Gyakum, and E. H. Atallah, 2007: Hurricane Katrina (2005). Part II: Evolution and hemispheric impacts of a diabatically generated warm pool. *Mon. Wea. Rev*., **135**, 3927–3949, https://doi.org/10.1175/2007MWR2096.1.

Menchaca, M. Q., and D. R. Durran, 2019: The influence of gravity waves on the slope of the kinetic energy spectrum in simulations of idealized midlatitude cyclones, *J. Atmos. Sci.*, **76**, 2103-2122, https://doi.org/10.1175/JAS-D-18-0329.1.

Meneveau, C., and J. Katz, 2000: Scale-Invariance and turbulence models for large-eddy simulation. *Annu. Rev. Fluid Mech*., **32**, 1-32, https://doi.org/10.1146/annurev.fluid.32.1.1.

Mlawer, E. J., S. J. Taubman, P. D. Brown, M. J. Iacono, and S. A. Clough,1997: Radiative transfer for inhomogeneous atmospheres: RRTM, a validated correlated–k model for the longwave. *J. Geophys. Res*., **102**, 16663–16682, https://doi.org/10.1029/97JD00237.

National Centers for Environmental Prediction/National Weather Service/NOAA/U.S. Department of Commerce. (2015) NCEP GFS 0.25 Degree Global Forecast Grids Historical Archive. Research Data Archive at the National Center for Atmospheric Research, Computational and Information Systems Laboratory, Boulder, CO.

National Hurricane Center, 2018: Costliest U.S. tropical cyclones. [Available online at https://www.nhc.noaa.gov/news/UpdatedCostliest.pdf.]

Oertel, A., M. Boettcher, H. Joos, M. Sprenger, and H. Wernli, 2020: Potential vorticity structure of embedded convection in a warm conveyor belt and its relevance for large-scale dynamics, *Wea. Clim. Dynam*., **1**, 127–153, https://doi.org/10.5194/wcd-1-127-2020.

Oertel, A., M. Sprenger, H. Joos, M. Boettcher, H. Konow, M. Hagen, and H. Wernli, 2021: Observations and simulation of intense convection embedded in a warm conveyor belt – how ambient vertical wind shear determines the dynamical impact, *Wea. Clim. Dynam.*, **2**, 89–110, https://doi.org/10.5194/wcd-2-89-2021.

Oertel, A. and S. Schemm, 2021: Quantifying the circulation induced by convective clouds in kilometer-scale simulations, *Quart. J. Roy. Meteor. Soc.*, **147**, 1752–1766, https://doi.org/10.1002/qj.3992.

Pantillon, F., J.-P. Chaboureau, C. Lac, and P. Mascart, 2013: On the role of a Rossby wave train during the extratropical transition of Hurricane Helene (2006). *Quart. J. Roy. Meteor. Soc.*, **139**, 370–386, https://doi.org/10.1002/qj.1974.

Papin, P., 2017: Variations in potential vorticity streamer activity: development pathways, environmental impacts, and links to tropical cyclone activity in the North Atlantic basin. Ph.D. dissertation, Univ. at Albany, 225pp. [Available online at https://search.proquest.com/docview/1978476273.]

Peng, J., L. Zhang, Y. Luo, and Y. Zhang, 2014: Mesoscale energy spectra of the mei-yu front system. Part I: kinetic energy spectra, *J. Atmos. Sci.*, **71**, 37-55, https://doi.org/10.1175/JAS-D-13-085.1.

Petterssen, S., and S. J. Smebye, 1971: On the development of extratropical cyclones. *Quart. J. Roy. Meteor. Soc.*, **97**, 457–482, https://doi.org/10.1002/qj.49709741407.

Pohorsky, R., M. Röthlisberger, C. M. Grams, J. Riboldi, and O. Martius, 2019: The climatological impact of recurving North Atlantic tropical cyclones on downstream extreme precipitation events. *Mon. Wea. Rev.*, **147**, 1513–1532, https://doi.org/10.1175/MWR-D-18-0195.1.

Pope, S. B., 2000: *Turbulent Flows*. Cambridge University Press, 802 pp.

Prince, K. C., and C. Evans, 2020: A climatology of indirect tropical cyclone interactions in the North Atlantic and western North Pacific basins, *Mon. Wea. Rev.*, **148**, 4035-4059, https://doi.org/10.1175/MWR-D-19-0377.1.

Quinting, J. F., and S. C. Jones, 2016: On the impact of tropical cyclones on Rossby wave packets: a climatological perspective. *Mon. Wea. Rev.*, **144**, 2021–2048, https://doi.org/10.1175/MWR-D-14-00298.1.

Reynolds, R. W., T. M. Smith, C. Liu, D. B. Chelton, K. S. Casey, and M. G. Schlax, 2007: Daily high-resolution-blended analyses for sea surface temperature. *J. Climate*, **20**, 5473–5496, doi:10.1175/JCLI-D-14-00293.1.

Reynolds, C. A., M. S. Peng, and J. H. Chen, 2009: Recurving tropical cyclones: Singular vector sensitivity and downstream impacts. *Mon. Wea. Rev.*, **137**, 1320–1337, doi:10.1175/2008MWR2652.1.

Riboldi, J., C. M. Grams, M. Riemer, and H. M. Archambault, 2019: A phase locking perspective on Rossby wave amplification and atmospheric blocking downstream of recurving western North Pacific tropical cyclones. *Mon. Wea. Rev.*, **147**, 567–589, https://doi.org/10.1175/MWR-D-18-0271.1.

Riemer, M., and S. C. Jones, and C. A. Davis, 2008: The impact of extratropical transition on the downstream flow: An idealized modeling study with a straight jet. *Quart. J. Roy. Meteor. Soc.*, **134**, 69–91, doi:10.1002/qj.189.

Riemer, M., and S. C. Jones, 2010: The downstream impact of tropical cyclones on a developing baroclinic wave in idealized scenarios of extratropical transition. *Quart. J. Roy. Meteor. Soc.*, **136**, 617–637, https://doi.org/10.1002/qj.605.

Riemer, M., and S. C. Jones, 2014: Interaction of a tropical cyclone with a high-amplitude, midlatitude wave pattern: waviness analysis, trough deformation, and track bifurcation. *Quart. J. Roy. Meteor. Soc.*, **140**, 1362–1376, https://doi.org/10.1002/qj.2221.

Ritchie, E. A., and R. L. Elsberry, 2003: Simulations of the extratropical transition of tropical cyclones: contributions by the midlatitude upper-level trough to reintensification. *Mon. Wea. Rev.*, **131**, 2112–2128, https://doi.org/10.1175/1520-0493(2003)131<2112:SOTETO>2.0.CO;2.

Ritchie, E. A., and R. L. Elsberry, 2007: Simulations of the extratropical transition of tropical cyclones: phasing between the upper-level trough and tropical cyclones. *Mon. Wea. Rev.*, **135**, 862–876, https://doi.org/10.1175/MWR3303.1.

Rios-Berrios, R., R. D. Torn, and C. A. Davis, 2016: An ensemble approach to investigate tropical cyclone intensification in sheared environments. Part I: Katia (2011), *J. Atmos. Sci.*, **73**, 71-93, https://doi.org/10.1175/JAS-D-15-0052.1.

Rios-Berrios, R. and R.D. Torn, 2017: Climatological analysis of tropical cyclone intensity changes under moderate vertical wind shear. *Mon. Wea. Rev.*, **145**, 1717–1738, https://doi.org/10.1175/MWR-D-16-0350.1.

Scheck, L., S. C. Jones, and M. Juckes, 2011: The resonant interaction of a tropical cyclone and a tropopause front in a barotropic model. Part II: Frontal waves. *J. Atmos. Sci.*, **68**, 420–429, https://doi.org/10.1175/2010JAS3482.1.

Schenkel, B. A. and R. E. Hart, 2015: An examination of the thermodynamic impacts of western North Pacific tropical cyclones on their tropical tropospheric environment. *J. Climate*, **28**, 7529–7560, https://doi.org/10.1175/JCLI-D-14-00780.1.

Schenkel, B. A., 2016: A climatology of multiple tropical cyclone events. *J. Climate*, **29**, 4861–4883, https://doi.org/10.1175/JCLI-D-15-0048.1.

Schenkel, B. A., 2017: Are multiple tropical cyclone events similar among basins? *J. Climate*, **30**, 5805–5813, https://doi.org/10.1175/JCLI-D-17-0088.1.

Skamarock, W. C., and Coauthors, 2019: A description of the Advanced Research WRF version 4. NCAR Tech. Note NCAR/TN-556+STR, 162pp, http://dx.doi.org/10.5065/1dfh-6p97.

Tang, B., and K. Emanuel, 2012: A ventilation index for tropical cyclones. *Bull. Amer. Meteor. Soc.*, **93**, 1901–1912, https://doi.org/10.1175/BAMS-D-11-00165.1.

Tewari, M., and Coauthors, 2004: Implementation and verification of the unified NOAH land surface model in the WRF model. *Abstract, 20th Conf. on Weather Analysis and Forecasting/16th Conf. on Numerical Weather Prediction*, Seattle, WA., *Amer. Meteor. Soc.*, **14.2A**.

Thorncroft, C. D., B. J. Hoskins, and M. E. McIntyre, 1993: Two paradigms of baroclinic-wave life-cycle behaviour. *Quart. J. Roy. Meteor. Soc*., **119**, 17–55, https://doi.org/10.1002/qj.49711950903.

Torn, R. D., and C. A. Davis, 2012: The influence of shallow convection on tropical cyclone track forecasts, *Mon. Wea. Rev.*, **140**, 2188-2197, https://doi.org/10.1175/MWR-D-11-00246.1.

Torn, R. D., and G. J. Hakim, 2015: Comparison of wave packets associated with extratropical transition and winter cyclones. *Mon. Wea. Rev.*, **143**, 1782–1803, https://doi.org/10.1175/MWR-D-14-00006.1.

Torn, R. D., 2016: Evaluation of atmosphere and ocean initial condition uncertainty and stochastic exchange coefficients on ensemble tropical cyclone intensity forecasts. *Mon. Wea. Rev*., **144**, 3487–3506, https://doi.org/10.1175/MWR-D-16-0108.1.

Velden, C. S., and L. M. Leslie, 1991: The basic relationship between tropical cyclone intensity and the depth of the environmental steering layer in the Australian region, *Wea. Forecasting*, **6**, 244-253, https://doi.org/10.1175/1520-0434(1991)006%3C0244:TBRBTC%3E2.0.CO;2.

Virtanen, P., and Coauthors, 2020: SciPy 1.0: fundamental algorithms for scientific computing in python. *Nat. Methods*, **17**, 261–272, https://doi.org/10.1038/s41592-019-0686-2.

Wirth, V., M. Riemer, E. K. Chang, and O. Martius, 2018: Rossby wave packets on the midlatitude waveguide—a review. *Mon. Wea. Rev.*, **146**, 1965–2001, https://doi.org/10.1175/MWR-D-16-0483.1.

Xiao, Z., M. Wan, S. Chen, and G. Eyink, 2009: Physical mechanism of the inverse energy cascade of two-dimensional turbulence: A numerical investigation, *J. Fluid Mech.*, **619**, 1-44, https://doi:10.1017/S0022112008004266.

Zhang, G., Z. Wang, T. J. Dunkerton, M. S. Peng, and G. Magnusdottir, 2016: Extratropical impacts on Atlantic tropical cyclone activity. *J. Atmos. Sci*., **73**, 1401–1418, doi:10.1175/JAS-D-15-0154.1.

Zhang, C., and Y. Wang, 2017: Projected future changes of tropical cyclone activity over the western North and South Pacific in a 20-km-mesh regional climate model. *J. Climate*, **30**, 5923-5941, https://doi.org/10.1175/JCLI-D-16-0597.1.

Zhang, G., Z. Wang, M. Peng, and G. Magnusdottir, 2017: Characteristics and impacts of extratropical Rossby wave breaking during the Atlantic hurricane season. *J. Climate*, **30**, 2363–2379, https://doi.org/10.1175/JCLI-D-16-0425.1.

Zhang, G., and Z. Wang, 2018: North Atlantic extratropical Rossby wave breaking during the warm season: wave life cycle and role of diabatic heating. *Mon. Wea. Rev.*, **146**, 695-712, https://doi.org/10.1175/MWR-D-17-0204.1.

Appendix A: Notes on the Calculation of the Ventilation Index with Gridded ERA-Interim Data

As given by equation (1.2), the ventilation index first shown in Tang and Emanuel (2012) is given by:

$$\Lambda = \frac{u_{shear}\chi_m}{u_{PI}} \tag{A1}$$

where $u_{shear} = |\boldsymbol{v_{850}} - \boldsymbol{v_{200}}|$ is the bulk environmental vertical wind shear magnitude between 850 and 200 hPa, u_{PI} is the maximum potential intensity (MPI), and χ_m is the nondimensional entropy deficit. The entropy deficit χ_m is defined as:

$$\chi_m = \frac{s_m^* - s_m}{s_{SST}^* - s_b} \tag{A2}$$

where s_m^* is the saturation entropy at 600 hPa in the TCs inner core, s_m is the environmental entropy at 600 hPa, s_{SST}^* is the saturation entropy at the sea-surface temperature (SST), and s_b is the entropy of the boundary layer. The calculation used for the MPI follows Bister and Emanuel (2002),

$$V_m^2 = c_p(T_s - T_0)\frac{T_s}{T_0}\frac{C_k}{C_d}(ln\theta_e^* - ln\theta_e)|_m \tag{A3}$$

where V_m is the maximum gradient wind speed, c_p is the heat capacity at constant pressure, T_s is the ocean temperature, T_0 is the mean outflow temperature, C_k the exchange coefficient for enthalpy, C_D the drag coefficient, θ_e^* the saturation equivalent potential temperature at the ocean surface, and θ_e the boundary layer equivalent potential temperature. The last factor of (A3) is calculated at the radius of maximum winds.

In Tang and Emanuel (2010), the 600 hPa saturation entropy is calculated as an average within a 100 km annulus of the best-track TC center, and the midlevel entropy is averaged over a

100-300 km annulus of the best-track TC center. These averages output a single number, while we are interested in viewing the ventilation index in a spatial sense. To match the methodology of Tang and Emanuel (2010) as closely as possible, for each grid point, a running spatial mean is performed, with a radius of one grid point for the saturation entropy, and a radius of one to four grid points for the midlevel entropy. A major drawback of working with a coarse-resolution reanalysis dataset such as the ERA-Interim, is the poor representation of TCs, particularly those which are small and intense, thus, even with the averaging performed above, it is important to note the likely misrepresentation of the saturation entropy. Additionally, given that the focus in these calculations is on the average downstream impact in the vicinity of the secondary TC far away from the primary TC, impacts from the TCs primary and secondary circulations to these quantities are retained for simplicity.

Finally, in Tang and Emanuel (2010) the MPI is calculated at the future location of the TC of interest. But given that we are again interested in a gridded calculation of the ventilation index, the MPI is simply calculated at every grid point, independent of where the TC is at a particular time. This leads to an MPI signal which is likely largely driven by sea-surface temperature anomalies in the vicinity of the TC caused by upwelling (Figs. A1 and A2). Therefore, much of the signal immediately surrounding the initial TC in the ventilation index in section 2 is largely driven by this upwelling signal, yet further away from the initial TC, this signal fades and the environmental characteristics become more apparent (Figs. A1 and A2).

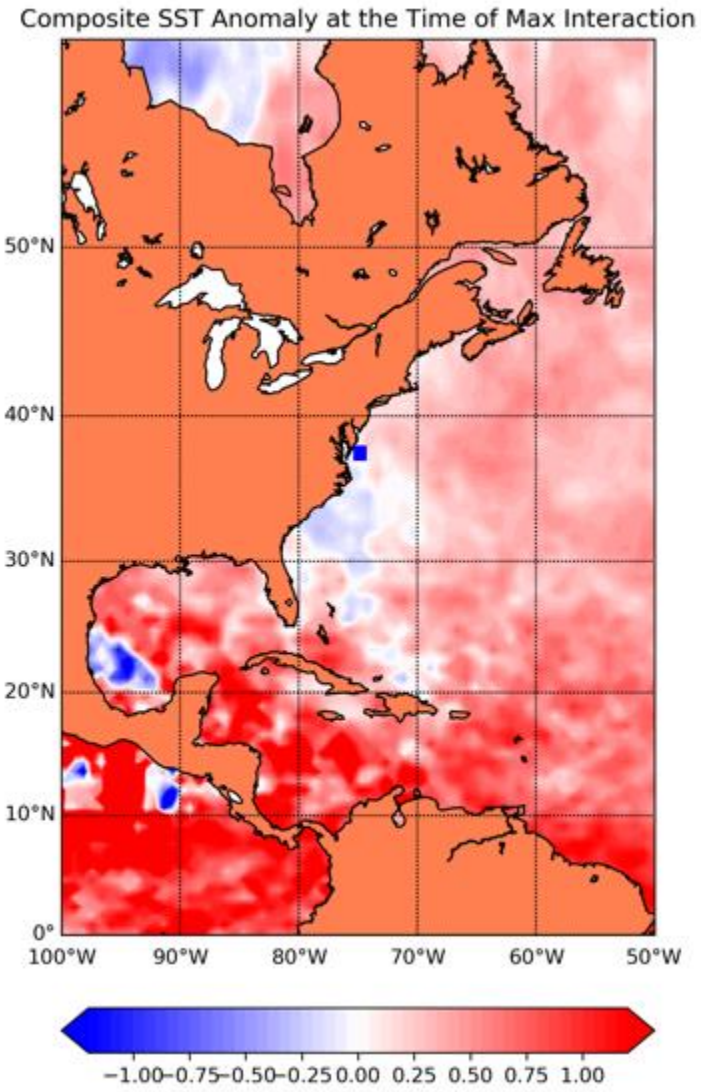

Figure A1. Composite SST anomaly (in K; per the color bar on the bottom) over the 26 identified indirect interactions in the North Atlantic basin. The blue square denotes the average location of the primary storms at the time of maximum interaction between the primary TCs and the midlatitude waveguide.

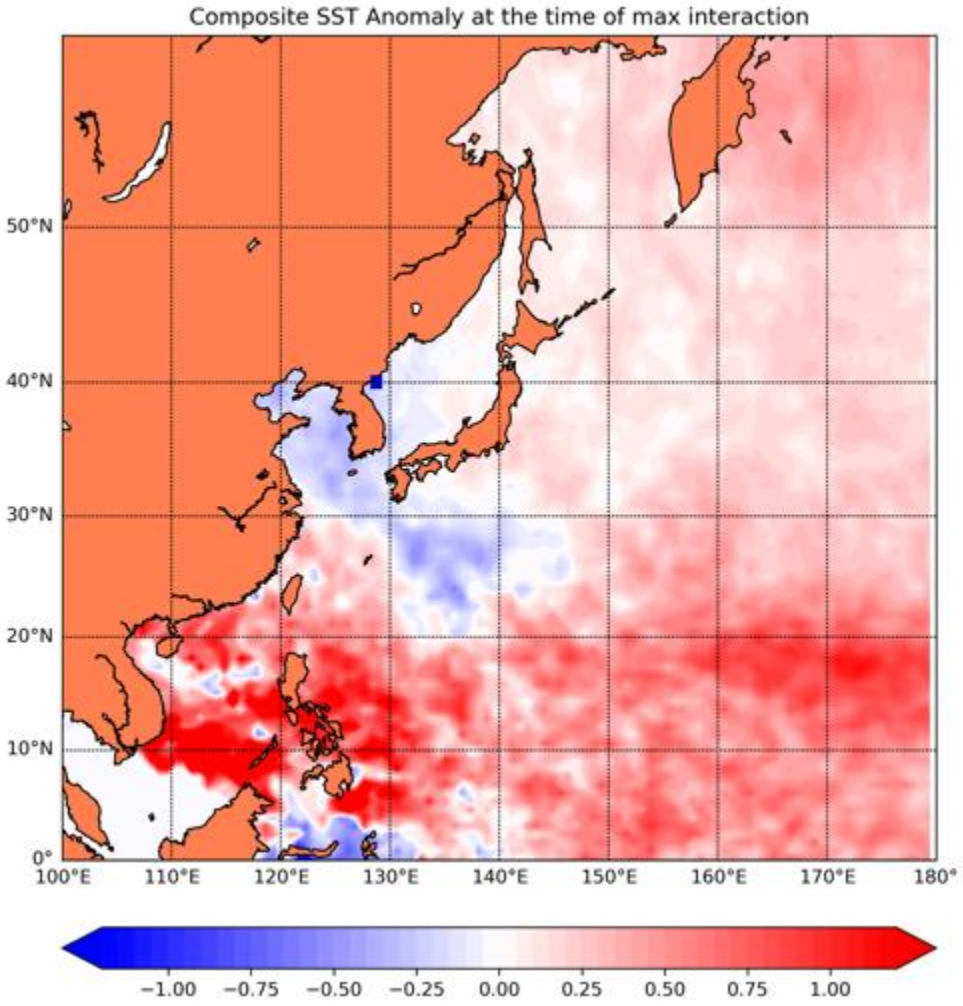

Figure A2. Same as in Figure A1, except averaged over the 56 identified indirect TC interaction events in the western North Pacific basin.

Appendix B: Derivation of the Fully Three-Dimensional PV Tendency Equation in Isentropic Coordinates

To obtain the fully three-dimensional PV tendency equation in isentropic coordinates, following Lackmann (2011), we first start with the isentropic horizontal momentum equations,

$$\left(\frac{\partial}{\partial t} + u\frac{\partial}{\partial x} + v\frac{\partial}{\partial y} + \dot{\theta}\frac{\partial}{\partial \theta}\right)u - fv + \frac{\partial M}{\partial x} - F_x = 0 \text{ and,} \tag{B1}$$

$$\left(\frac{\partial}{\partial t} + u\frac{\partial}{\partial x} + v\frac{\partial}{\partial y} + \dot{\theta}\frac{\partial}{\partial \theta}\right)v + fu + \frac{\partial M}{\partial y} - F_y = 0 \tag{B2}$$

where u and v are the zonal and meridional wind components, respectively, F_x and F_y denote the frictional force components in the zonal and meridional directions, respectively, $\dot{\theta} = \frac{\partial \theta}{\partial t}$, f is the Coriolis parameter, and M is the Montgomery streamfunction, given as,

$$M = gZ + C_pT \tag{B3}$$

where g is gravity, Z is the geopotential height of the isentropic surface, C_p is the specific heat at constant pressure for dry air, and T is the temperature on the isentropic surface.

We then subtract the y-derivative of (B1) from the x-derivative of (B2) to obtain the isentropic vorticity equation,

$$\frac{\partial \zeta_{a\theta}}{\partial t} + \frac{\partial}{\partial x}\left[u\zeta_{a\theta} + \dot{\theta}\frac{\partial v}{\partial \theta} - F_y\right] + \frac{\partial}{\partial y}\left[v\zeta_{a\theta} + \dot{\theta}\frac{\partial u}{\partial \theta} - F_x\right] = 0 \tag{B4}$$

where $\zeta_{a\theta}$ is the absolute vorticity on an isentropic surface. The vector form of (B4) is given by:

$$\frac{\partial \zeta_{a\theta}}{\partial t} + \nabla \cdot \left(\vec{V}\zeta_{a\theta}\right) + \hat{k} \cdot \nabla_\theta \times \left(\vec{F} - \dot{\theta}\frac{\partial \vec{V}}{\partial \theta}\right) = 0 \tag{B5}$$

Where $\vec{V} = (u, v, 0)$ represents the horizontal wind on an isentropic surface, $\nabla = (\partial_x, \partial_y, 0)$ represents the horizontal gradient operator on an isentropic surface, $k = (0,0,1)$ represents the unit vector perpendicular to an isentropic surface.

(B5) can be rewritten, such that

$$\vec{J} = (u\zeta_{a\theta}, v\zeta_{a\theta}, 0) + \left(\dot{\theta}\frac{\partial v}{\partial \theta}, -\dot{\theta}\frac{\partial u}{\partial \theta}, 0\right) + (-F_y, F_x, 0) \tag{B6}$$

where,

$$\frac{\partial \zeta_{a\theta}}{\partial t} + \nabla \cdot \vec{J} = 0 \tag{B7}$$

with (B7) stating that the only way to locally change absolute vorticity on an isentropic surface are through divergence of the vector $\vec{J}$.

We then write a general relation for the mixing ratio of an arbitrary quantity q such that,

$$\frac{\partial(\sigma q)}{\partial t} + \nabla \cdot \vec{J} = \sigma S \tag{B8}$$

where S represents all sources and sinks of q, and σ is the isentropic density defined as,

$$\sigma = -\frac{1}{g}\frac{\partial p}{\partial \theta} \tag{B9}$$

and,

$$\vec{J}_{new} = \left(u\sigma q, v\sigma q, \dot{\theta}\sigma q\right) + (-F_y, F_x, 0) \tag{B10}$$

If we let q represent the dry-air mixing ratio (equal to 1) and neglect friction and sources or sinks, then (B8) becomes the isentropic continuity equation,

$$\frac{\partial \sigma}{\partial t} + \nabla \cdot \left(\sigma \vec{V}\right) + \frac{\partial}{\partial \theta}\left(\sigma \dot{\theta}\right) = 0 \tag{B11}$$

When drawing comparisons between (B8) and (B10) with (B6) and (B7), we get,

$$q = \frac{\zeta_{a\theta}}{\sigma} \tag{B12}$$

which we can rewrite as,

$$q = -g\frac{\partial \theta}{\partial p}\zeta_{a\theta} = PV \tag{B13}$$

where PV is the Rossby-Ertel potential vorticity.

To obtain a tendency equation for PV we will utilize (B8), with $q = PV$. This gives,

$$\frac{\partial \sigma PV}{\partial t} + \frac{\partial}{\partial x}\left[u\sigma PV + \dot{\theta}\frac{\partial v}{\partial \theta} - F_y\right] + \frac{\partial}{\partial y}\left[v\sigma PV - \dot{\theta}\frac{\partial u}{\partial \theta} + F_x\right] = 0 \qquad \text{(B14)}$$

which can be rewritten to,

$$\frac{dPV}{dt} = -g\frac{\partial \theta}{\partial p}\zeta_{a\theta}\frac{\partial \dot{\theta}}{\partial \theta} + g\frac{\partial \theta}{\partial p}\left[\frac{\partial \dot{\theta}}{\partial x}\frac{\partial v}{\partial \theta} - \frac{\partial F_y}{\partial x} - \frac{\partial \dot{\theta}}{\partial y}\frac{\partial u}{\partial \theta} + \frac{\partial F_x}{\partial x}\right] \qquad \text{(B15)}$$

excluding friction simplifies to,

$$\frac{dPV}{dt} = -g\frac{\partial \theta}{\partial p}\zeta_{a\theta}\frac{\partial \dot{\theta}}{\partial \theta} + g\frac{\partial \theta}{\partial p}\left[\frac{\partial \dot{\theta}}{\partial x}\frac{\partial v}{\partial \theta} - \frac{\partial \dot{\theta}}{\partial y}\frac{\partial u}{\partial \theta}\right] \qquad \text{(B16)}$$

which, when expanded into the local and advective components, and written in vector form, results in equation (2.3).

As noted in Section 2.2.3, $\dot{\theta}$ in WRF is made up of several terms,

$$\dot{\theta} = \dot{\theta}_{rad} + \dot{\theta}_{shallow\ cu.} + \dot{\theta}_{cu.} + \dot{\theta}_{pbl} + \dot{\theta}_{mp} \qquad \text{(B17)}$$

where $\dot{\theta}_{rad}$ is the total contribution to the potential temperature tendency from the radiation parameterization $\dot{\theta}_{shallow\ cu.}$ is the contribution to the potential temperature tendency from the shallow cumulus parameterization, $\dot{\theta}_{cu.}$ is the contribution to the potential temperature tendency from the cumulus parameterization, $\dot{\theta}_{pbl}$ is the contribution to the potential temperature tendency from the planetary boundary layer parameterization, and $\dot{\theta}_{mp}$ is the contribution to the potential temperature tendency from the microphysical parameterization. Given that the numerical simulations are performed at convection-permitting grid spacings with no cumulus parameterization, contributions from the two cumulus terms are zero. Additionally, when calculating the PV tendency in (B16), the focus is primarily on the middle- to upper-troposphere, where turbulent vertical mixing is quite small, making contributions from the turbulent vertical mixing scheme orders of magnitude less than other terms on the right-hand side of (B17), thus it can be neglected. Finally, contributions from the radiation parameterizations are several orders of magnitude weaker than the microphysical heating (not shown), resulting in the approximation:

$$\dot{\theta} \cong \dot{\theta}_{mp}. \tag{B18}$$

Appendix C: Notes on the Calculation of the Horizontal Spectral Kinetic Energy Budget

Following Peng et al. (2014) and Menchaca and Durran (2019), the horizontal kinetic energy of the flow can be represented as,

$$KE_h = \frac{1}{2}\rho \boldsymbol{u}^2 \tag{C1}$$

where $\boldsymbol{u} = (u, v)$ is the horizontal wind vector and ρ is the density. If we perform a Fourier transform to transform from physical to wavenumber space, (C1) becomes,

$$KE_h(\boldsymbol{k}) = \frac{1}{2}\bar{\rho}\hat{\boldsymbol{u}}^*(\boldsymbol{k}) \cdot \hat{\boldsymbol{u}}(\boldsymbol{k}) \tag{C2}$$

where $\boldsymbol{k} = k_x i$, with a hat denoting a Fourier-transformed variable, an asterisk denoting the complex conjugate, and $\bar{\rho}$ representing a horizontally uniform background density profile. The time rate of change of (C2) is given by:

$$\partial_t KE_h(\boldsymbol{k}) = \frac{\bar{\rho}}{2}[(\boldsymbol{u}, \partial_t \boldsymbol{u})_{\boldsymbol{k}} + c.c.] \tag{C3}$$

where $(\boldsymbol{a}, \boldsymbol{b})_{\boldsymbol{k}} = \hat{\boldsymbol{a}}^*(\boldsymbol{k}) \cdot \hat{\boldsymbol{b}}(\boldsymbol{k})$, and the $c.c.$ denotes the complex conjugate of whatever term comes before the "$c.c.$", which, in the case of (C3) would be the complex conjugate of $(\boldsymbol{u}, \partial_t \boldsymbol{u})_{\boldsymbol{k}}$. If we let $\nabla = (\frac{\partial}{\partial x}, \frac{\partial}{\partial y}, 0)$, the horizontal momentum equation in physical space can be written as,

$$\partial_t \boldsymbol{u} = -\boldsymbol{u} \cdot \nabla \boldsymbol{u} - w\partial_z \boldsymbol{u} - c_p \bar{\theta} \nabla \pi' + \boldsymbol{F}_h \tag{C4}$$

where $\boldsymbol{F}_h$ is the turbulent subgrid-scale diffusivity, w is the vertical velocity, c_p is the specific heat capacity for dry air at constant pressure, $\bar{\theta}(z)$ is a vertically varying approximation to the full $\theta(x, y, z, t)$, and π is the Exner function, which is comprised of a horizontally uniform

component $\bar{\pi}(z)$, where the overbar denotes a spatial average of the domain of interest, that is in hydrostatic balance with $\bar{\theta}(z)$ and the remainder $\pi'(x, y, z, t)$, where $\pi' = \pi - \bar{\pi}$.

Substituting (C4) into (C3), we obtain:

$$\partial_t KE_h(\boldsymbol{k}) = \frac{\bar{\rho}}{2}\left[\left(\boldsymbol{u}, -\boldsymbol{u}\cdot\nabla\boldsymbol{u} - w\partial_z\boldsymbol{u} - c_p\bar{\theta}\nabla\pi' + \boldsymbol{F}_h\right)_{\boldsymbol{k}} + c.c.\right] \tag{C5}$$

which can split into three separate terms. It should be noted that the $c.c.$ is distributed to the terms inside of the preceding parentheses in (C5), and the leading $\frac{\bar{\rho}}{2}$ is distributed to the terms inside of the bracket. Additionally, the negative leading sign in some terms is due to the reverse distribution of a negative sign. The first term of the distributed form of (C5) is the tendency arising from advection,

$$A(\boldsymbol{k}) = -\frac{\bar{\rho}}{2}[(\boldsymbol{u}, \boldsymbol{u}\cdot\nabla\boldsymbol{u} + w\partial_z\boldsymbol{u})_{\boldsymbol{k}} + c.c.] \tag{C6}$$

the second term is the tendency arising from the pressure gradient force,

$$P(\boldsymbol{k}) = -\frac{\bar{\rho}}{2}c_p\bar{\theta}[(\boldsymbol{u}, \nabla\pi')_{\boldsymbol{k}} + c.c.] \tag{C7}$$

and the final term is the tendency due to dissipation,

$$D(\boldsymbol{k}) = \frac{\bar{\rho}}{2}(\boldsymbol{u}, \boldsymbol{F}_h)_{\boldsymbol{k}} + c.c. \tag{C8}$$

The advective tendency in (C6) can be further decomposed into,

$$A(\boldsymbol{k}) = T(\boldsymbol{k}) + V_a(\boldsymbol{k}) + \varepsilon_1(\boldsymbol{k}) \tag{C9}$$

where,

$$T(k) = -\bar{\rho}\left\{\left[\boldsymbol{u}, \boldsymbol{u}\cdot\nabla\mathbf{u} + \frac{1}{2}\boldsymbol{u}(\nabla\cdot\boldsymbol{u})\right]_k - \frac{1}{2}(\partial_z\boldsymbol{u}, w\boldsymbol{u})_k + \frac{1}{2}(\boldsymbol{u}, w\partial_z\boldsymbol{u})_k\right\} + \text{c.c.} \tag{C10}$$

is the conservative transfer of energy between wavenumbers,

$$V_a(\boldsymbol{k}) = -\frac{1}{2}\partial_z[\bar{\rho}(\boldsymbol{u}, w\boldsymbol{u})_{\boldsymbol{k}}] + c.c. \tag{C11}$$

is the divergence of the vertical advective energy flux, and

$$\varepsilon_1(\boldsymbol{k}) = \frac{\bar{\rho}}{2}\{[\boldsymbol{u}, \boldsymbol{u}(\nabla \cdot \boldsymbol{u} + \partial_z w]_{\boldsymbol{k}} + \partial_z \ln(\bar{\rho})(\boldsymbol{u}, w\boldsymbol{u})_{\boldsymbol{k}}\} + c.c. \quad \text{(C12)}$$

with (C12) representing the component of the advective tendency which is nonzero when the anelastic continuity equation is not satisfied. Although our model is not anelastic (similar to Menchaca and Durran (2019)), they note that (C12) is quite small, so we neglect (C12) as they did in their study.

To attain the buoyancy and full vertical advective flux terms in (2.10), we first write out the vertical component of the pressure gradient force using the pseudo-incompressible approximation,

$$P_v(\boldsymbol{k}) = c_p \bar{\rho}\bar{\theta}(w, \partial_z \pi')_{\boldsymbol{k}} - c_p \partial_z[\bar{\rho}\bar{\theta}(w, \pi')_{\boldsymbol{k}}] + c.c. \quad \text{(C13)}$$

Under the hydrostatic approximation, $\partial_z \pi'$ is proportional to θ'.

The first term in (C13) represents buoyancy forcing, which can be written as:

$$B(\boldsymbol{k}) = c_p \bar{\rho}\bar{\theta}(w, \partial_z \pi')_{\boldsymbol{k}} + c.c. \quad \text{(C14)}$$

whereas the second term in (C13) represents the divergence of the vertical flux of energy due to pressure work(or pressure-volume work), which can be physically represented by the expansion of an air parcel as it rises, and can be combined with (C11) to obtain the total vertical energy flux divergence,

$$V(\boldsymbol{k}) = -\frac{1}{2}\partial_z[\bar{\rho}(\boldsymbol{u}, w\boldsymbol{u})_{\boldsymbol{k}}] - c_p \partial_z[\bar{\rho}\bar{\theta}(w, \pi')_{\boldsymbol{k}}] + c.c. \quad \text{(C15)}$$

The expression for $\boldsymbol{F_h}$ in (C8) is,

$$K_h \nabla^2 \boldsymbol{u} + K_v \frac{\partial^2 \boldsymbol{u}}{\partial z^2} \quad \text{(C16)}$$

where K_h is the horizontal eddy viscosity computed in WRF-ARW as a function of the horizontal deformation and K_v is the vertical eddy viscosity computed from the planetary boundary layer parameterization.

Appendix D: Modifications to the WRF Code

In the WRF-ARW model, after the microphysics parameterization has been called to calculate updated microphysical species and their concentrations, the microphysical potential-temperature tendency is calculated and then applied to the perturbation potential temperature field. This is accomplished by first calculating the dry perturbation potential temperature,

$$\Delta\theta_{dry} = \theta_{dry,new} - \theta_{dry,old} \tag{D1}$$

where θ_{dry}^{new} is the new perturbation potential temperature field after the microphysical parameterization is called and θ_{dry}^{old} is the perturbation potential temperature field before the microphysical parameterization is called. The full perturbation moist potential temperature field is then,

$$\theta'_{moist,new} = \theta_{dry,old} * \left[1 + \left(\frac{R_v}{R_d}\right) * q_{v,old}\right] + \Delta\theta_{dry} * \left[1 + \left(\frac{R_v}{R_d}\right) * q_{v,new}\right] + \left[\left(\frac{R_v}{R_d}\right) * \Delta q_v * \theta_{dry,new}\right] - T_0 \tag{D2}$$

where $R_v = 461\, JK^{-1}kg^{-1}$ and $R_d = 287\, JK^{-1}kg^{-1}$ are the gas constants for moist and dry air respectively; $q_{v,old}$ and $q_{v,new}$ are the vapor mixing ratio before and after applying the updated microphysical tendencies, respectively; $\Delta q_v = q_{v,new} - q_{v,old}$; and $T_0 = 300\ K$ is the base-state temperature which is subtracted to get the perturbation. In all sensitivity simulations performed, term two on the right-hand side of (D2) is made to be zero over all vertical levels, effectively negating any contributions from the microphysical parameterization to the simulated potential-temperature field while still allowing the hydrometeors to evolve naturally.

Curriculum Vita
Kevin Prince

Personal Information

Current Address
600 Victory Garden Dr Apt C22
Tallahassee, FL 32301

Contact Information
E-Mail: kprince@uwm.edu
Phone: (517) 862-3709

Last Updated: 28 June 2022

DOB: 20 January 1994

Education

2018-2022	**University of Wisconsin-Milwaukee, Ph.D., Meteorology** Advisor: Prof. Clark Evans
2016-2018	**University of Wisconsin-Milwaukee, M.S., Meteorology** Advisor: Prof. Clark Evans
2012-2016	**Central Michigan University, B.S., Meteorology, Cum Laude** Minors: Mathematics

Professional Positions

2022-Present	**National Research Council Postdoctoral Research Fellow**, Naval Postgraduate School, Monterey, CA Lab Host: Dr. Will Komaromi
2021	**Summer Research Intern,** Naval Research Laboratory, Monterey, CA
2021-2022	**Distinguished Dissertation Fellow,** Univ. Wisconsin-Milwaukee, Milwaukee, WI
2018-2019	**Research Assistant,** Univ. Wisconsin-Milwaukee, Milwaukee, WI
2017-2021	**Weather Observer,** FAA General Mitchell International Airport, Milwaukee, WI
2016-2018	**Teaching Assistant,** Univ. Wisconsin-Milwaukee, Milwaukee, WI
2015-2016	**Undergraduate Research Assistant,** Central Michigan University, Mount Pleasant, MI

Awards and Honors

2020	**Recipient,** Naval Research Enterprise Intern Program Summer Intern
2020	**Recipient,** Distinguished Dissertation Fellowship, University of Wisconsin-Milwaukee
2019	**Recipient,** World Meteorological Organization Travel Funding Grant
2018	**Recipient,** Outstanding Student Conference Poster Award, American Meteorological Society 17th Annual Student Conference
2015	**Recipient,** Central Michigan University Summer Scholars Scholarship $3,500

Peer-Reviewed Publications

Prince, K. C., and C. Evans, 2022: A case-study analysis of convective-scale contributions to midlatitude waveguide preconditioning preceding a tropical cyclone-midlatitude waveguide interaction, *J. Atmos. Sci.*, provisionally accepted.

Prince, K. C., and C. Evans, 2020: A climatology of indirect tropical cyclone interactions in the north Atlantic and western north Pacific basins, *Monthly Weather Review*, **148**, 4035-4059.

Prince, K. C., and C. Evans, 2018: A climatology of extreme South American cold surges. *J. Appl. Meteor. Climatol.*, **57**, 2297–2315.

Selected Presentations

Prince, K. C., C. Evans, and S. Kravtsov, 2022: A case-study analysis of convective-scale contributions to tropical cyclones' interactions with the midlatitude waveguide. *Abstract, 35th Conf. on Hurricanes and Tropical Meteorology*, New Orleans, LA, Amer. Meteor. Soc., 13C.3.

Prince, K., and C. Evans, 2020: A climatology of indirect tropical cyclone interactions. *Abstract, 30th Conf. on Weather Analysis and Forecasting/26th Conf. on Numerical Weather Prediction*, Boston, MA, Amer. Meteor. Soc., 12D.4.

Prince, K., 2018: A climatology of Andean South American Cold Surges and their Continental Effect. *Abstract, 17th Annual Student Conference,* Austin, TX, Amer. Meteor. Soc., 172.

Prince, K., 2016: Accuracy of Frost and Freeze Forecasts for Northwestern Michigan Wine Growers. *Abstract, 15th Annual Student Conference,* New Orleans, LA, Amer. Meteor. Soc., 169.